Design, manufacture and commissioning of a low pressure quasistatic bulge tester for skin and membrane tissue

Andrew Michael Curry

Supervisor: Dr Reuben Govender
Co-supervisor: Prof. Gerald Nurick

MEC5000W - MSc in Mechanical Engineering
in the Department of Mechanical Engineering
Faculty of Engineering and the Built Environment
University of Cape Town

November 2019

Declaration

I, Andrew Michael Curry, hereby:

I know the meaning of plagiarism and declare that all the work in the document, save for that which is properly acknowledged, is my own. This thesis/dissertation has been submitted to the Turnitin module (or equivalent similarity and originality checking software) and I confirm that my supervisor has seen my report and any concerns revealed by such have been resolved with my supervisor.

I am now presenting the report for examination for the degree of M.Sc Eng (Mechanical).

A.M. Curry

November 10, 2020

Abstract

The material properties of skin are of great importance to a variety of fields such as dermatology and reconstructive surgery. Relatively little infrastructure and expertise exists locally in South Africa for testing biological tissue. The difficulties of testing the material properties of skin are the non-uniformity and anisotropy across specimen location and subjects. This anisotropy is most commonly measured by tensile testing of samples cut in different orientations. However, the individual samples at different orientations would be extracted from slightly different locations on the same subject, which will naturally vary in response. Bulge testing is a method of determining response to tension in different directions at the same location, by applying biaxial tension. It uses a positive pressure applied to a peripherally clamped specimen to deform the specimen in a balloon type manner.

In this project, bulge testing apparatus was designed and built for the purpose of testing skin and membrane tissue, under biaxial tension. The testing apparatus consists of a syringe pump to control inflation of a specimen, which is clamped in an inflation chamber. Digital Image Correlation (DIC) was used to capture the 3D deformation fields of the specimen, and hence infer the strain fields.

To simplify commissioning testing, a commercial silicone elastomer suited for skin prosthetics, was used to manufacture specimens for uniaxial and bulge experimental testing. Two types of bulge specimens were manufactured, standard round specimens and elliptical specimens. The round specimens were used to compare their material response to uniaxial tests and the elliptical bulge specimens were used to simulate the anisotropic response of skin.

The method of analysis used in this project is based on using DIC and curvature calculations at multiple points to calculate membrane stresses in principal directions. The method of calculating principal curvatures from DIC is adapted from the work by Machado *et al.* [1] that calculated Gaussian curvature using the first and second fundamental forms of a surface.

In total 18 round, 6 elliptical and 10 uniaxial specimens were tested and the material properties were found to vary slightly between each specimen. The spread in data between the uniaxial and bulge tests was found to be very similar with the bulge data showing 10 % spread at 1.2 stretch and constant 8 % spread above 1.2 stretch and the uniaxial data

showing increasing spread from 7 % to 15 %. The curvature results showed very clear principal directions of curvature for the elliptical specimens. This demonstrated that the method used in this project is capable of clearly extracting the orientations of stiffer fibre directions of skin and other collagenous tissue.

Acknowledgements

My sincere gratitude goes to:

The NRF for funding this research.

My supervisors, Dr Reuben Govender and Prof. Gerald Nurick, for without you this would not have been possible. Thank you for all the support and mentorship throughout the duration of this project.

Richard Whittemore for your expertise with all things electronics. Dr. Richard Curry for your expertise and assistance with Digital Image Correlation. Pierre Smith and his workshop staff for all of their work in machining parts for my project.

My fellow postgrads at BISRU, thank you for always being willing to assist with any advice and always providing endless humour in the office.

To my family and friends for providing endless support and motivation throughout.

Contents

Nomenclature **xv**

1 Introduction **1**

1.1 Background and Motivation 1

1.2 Objectives 2

1.3 Scope 2

1.4 Outline 3

2 Literature Review **4**

2.1 Properties and Structure of Skin 4

2.1.1 Layers 4

2.1.2 Typical Mechanical Response 5

2.1.3 Langer Lines 6

2.1.4 Age and Location 7

2.2 Mechanical Properties of Skin and Testing Methodologies 7

2.2.1 Uniaxial Tension 9

2.2.2 Biaxial Tension 10

2.2.3 Other Testing Methods 12

2.2.4 Preconditioning 13

2.3 Digital Image Correlation 13

2.4 Curvature Calculations 14

2.5 Constitutive Models 15

3 Design of Experimental Apparatus 17

3.1 Requirements 17

3.1.1 Specimen Diameter 18

3.1.2 Strain Rate and Inflation Rate 19

3.1.3 Pressure and Accuracy 21

3.1.4 Portable 22

3.1.5 Sampling Rate 22

3.1.6 Syringe Stroke Length 22

3.1.7 Maximum Piston Force 22

3.1.8 Inflation Chamber Easily Disassemblable 22

3.2 Mechanical Design 23

3.2.1 Inflation Chamber 24

3.2.2 Syringe Pump 25

3.3 Instrumentation and Control System 26

3.3.1 Stepper Motor and Driver 26

3.3.2 Rotary Encoder 28

3.3.3 Pressure Transducer and ADC 28

3.3.4 Limits and Switches 28

3.3.5 Data Output 29

3.3.6 Coding Environment 30

4 Experimental Methodology 32

4.1 Digital Image Correlation 32

4.1.1 Cameras, lenses and lighting 33

4.1.2 Calibration 34

4.1.3 Correlation settings 35

4.2 Curvature calculations . . . 35
4.3 Stress calculations . . . 36
4.4 Graphing . . . 37
4.5 Specimen preparation . . . 39
4.6 Testing plan . . . 40

5 Results **42**

5.1 Stretch-stress graphs . . . 42
5.1.1 Uniaxial tension . . . 42
5.1.2 Round bulge . . . 43
5.1.3 Elliptical bulge . . . 45
5.2 Directions of curvature . . . 48
5.3 Bulge profiles . . . 50
5.4 Strain Rate . . . 51
5.4.1 Round specimen strain rate response . . . 51
5.4.2 Elliptical specimen strain rate response . . . 52

6 Discussion **54**

6.1 Material behaviour . . . 54
6.2 Specimens and Speckle Patterns . . . 56
6.3 Directions of curvature . . . 58
6.3.1 Elliptical specimens . . . 58
6.3.2 Round specimens . . . 58
6.4 Testing Apparatus . . . 59
6.4.1 Mechanical apparatus . . . 59
6.4.2 Imaging and DIC . . . 59
6.5 Strain Rate . . . 59
6.6 Ogden material models . . . 61

7 Conclusions and Recommendations **64**

7.1 Experimental Apparatus 64

7.2 Experimental Testing and Results 65

7.3 Imaging and DIC 65

7.4 Recommendations 66

Appendices **72**

A Engineering Drawings and Device Images **72**

B Electronics wiring diagram **85**

C Arduino code **87**

C.1 Motor Arduino Code 87

C.2 Sensor Arduino Code 95

D Matlab code **102**

D.1 Curvature Code 102

D.2 Variable Processing 105

D.3 Stress Calculation 108

E Additional Resources **109**

E.1 Motor Calibration 109

E.2 Pressure Transducer Calibration 111

List of Figures

2.1 Diagram showing the layers that make up skin [3]. 5

2.2 Schematic adapted from Delalleau *et al.* [8] showing the typical phases seen in the mechanical response of skin tissue. 5

2.3 Schematic showing the Langer lines over the front and back of the human body [9]. 6

2.4 Graph showing the difference in stretch-stress response between human skin specimens cut parallel and perpendicularly to Langer lines [10]. 7

2.5 Schematic showing where Ní Annaidh *et al.* [12] cut uniaxial tensile specimens from the backs of human cadavers. 9

2.6 Graph from Seibert *et al.* [23] showing the plane of invariants, containing pure uniaxial tension, equibiaxial tension and loading states between. . . . 10

2.7 Schematic showing the 12 axis planer biaxial tension machine by Reihsner *et al.* [5]. 11

2.8 Planer biaxial test by Perez *et al.* [25] pulling a sclera specimen in two directions. 11

2.9 Simple schematic of a bulge test [27]. 12

2.10 Results from Hendricks *et al.* [29] comparing tests with different aperture sizes. 13

2.11 Graphics from Istra4D DIC software showing a height map and visualisation of deformation. 14

3.1 Schematic showing a bulge test with assumed spherical bulge. 19

3.2 Diagram of spherical cap geometry. 20

3.3 Estimated stretch vs strain rate for a constant volumetric rate of 0.05 ml/s. 21

3.4 Schematics explaining the basic workings of the mechanical apparatus. . . 24

3.5 Labelled diagram of the different parts of the inflation chamber design. . . 25

3.6 Labelled diagram showing the different parts of the syringe pump design. . 26

3.7 Flow diagram showing how the electronic components interface with each other. 27

3.8 Flow diagram of the basic structure of the control system. 31

4.1 Camera positioning for experimental testing. 33

4.2 Image showing the the markers that have been found as part of a 3D calibration process in Istra4D. 34

4.3 Example of a stress vs stretch graph for one point at the apex of a specimen. 38

4.4 Example of a stress vs stretch graph for nine points around the apex of a specimen. 38

4.5 Example of a stress vs stretch graph showing the averaged response at the centre of a specimen. 39

5.1 Stretch-stress graph for uniaxial tensile tests where specimens T1 to T5 and T6 to T10 were tested at strain rates 1.6×10^{-2} /s and 5×10^{-2} /s respectively. 43

5.2 Stretch-stress curves in principal directions for all round specimens R1 to R18 inflated at rates between 0.1 ml/s and 5.9 ml/s. 44

5.3 Stretch-stress curves in principal directions for specimens R1 to R3 inflated at 0.1 ml/s. 44

5.4 Stretch-stress curves in principal directions for specimens R4 to R6 inflated at 5. 9ml/s. 45

5.5 Stretch-stress curves in principal directions for all elliptical specimens E1 to E6 which were all tested at 1.18 ml/s. 46

5.6 Stretch-stress curves in principal directions for 40x50 elliptical specimens E1 to E3. 46

5.7 Stretch-stress curves in principal directions for 30x50 elliptical specimens E4 to E6. 47

5.8 Stretch-stress curves in principal directions for round and elliptical specimens R1 and E1. 47

5.9 Quiver plots showing principal directions of curvature at each point of the round and elliptical specimens R7, E2 and E5 at apex strains of 10 %, 30 % and 57 %. 49

5.10 Bulge profile of specimen R5 (round specimen). 50

5.11 Bulge profile of specimen E1 (40x50 elliptical specimen). 50

5.12 Bulge profile of specimen E4 (30x50 elliptical specimen). 51

5.13 Graph showing the strain rate responses for a round specimen (R7) in both principal directions, inflated at 1.2 ml/s (50 RPM). 52

5.14 Graph showing the strain rate response for an elliptical specimen (E2) in both principal directions, inflated at 1.2 ml/s (50 RPM). 53

5.15 Graph showing the strain rate response for an elliptical specimen (E5) in both principal directions, inflated at 1.2 ml/s (50 RPM). 53

6.1 Plot showing the spread in stress curves at various stretch values comparing both uniaxial and bulge data. 55

6.2 Plot showing the normalised spread of the stress curves relative to the mean stresses at various stretch values comparing both uniaxial and bulge data where the error bars indicate upper and lower bounds for variation. 55

6.3 Images showing the speckle patterns of specimens R1 to R18 and E1 to E6. 57

6.4 Results from Tonge *et al.* [4] where 2-D ellipses are fitted to bulge profiles of human skin specimens in the fibre and perpendicular directions. 58

6.5 Comparing strain rates for specimens R7, E2 and E5 in both principal directions, all inflated at 1.2 ml/s (50 RPM). 60

6.6 Estimate of inflation rate profile for near constant strain rate. 61

6.7 Third order Ogden material models for uniaxial and bulge experimental data. 62

6.8 Using the uniaxial Ogden parameters to model the biaxial response and vice versa. 63

A.1 Image of the syringe pump and inflation chamber. 82

A.2 Image of syringe pump with a 60 ml syringe installed. 82

A.3 Image of camera and lighting set up. 83

A.4 Image of camera and lighting set up running during a test. 84

E.1 Calibration curve for the stepper motor output speed using 1/8 micro-stepping. 111

E.2 Calibration curve for the 100kPa pressure transducer. 112

List of Tables

2.1 Summary of literature including *in vitro* and *in vivo* studies on human skin [7][12]. 8

3.1 Summary of design requirements for the experimental apparatus. 18

3.2 Table showing an example of the data output from the Sensor-Arduino. . . 29

4.1 Table showing the full testing plan for all specimens. 41

6.1 Table showing the grid and facet DIC settings for the different specimen types. 56

6.2 Material constants for the three term Ogden material models of bulge and tensile experiments. 62

E.1 Table showing the motor speeds for different micro-stepping settings. . . . 110

Nomenclature

Greek Lower Case Symbols

α	Ogden hardening exponent
η	Efficiency
$\kappa_{i,ii}$	Principal curvature
λ_a	Principal stretch
μ	Shear moduli
σ_a	Principal stress

Greek Upper Case Symbols

Ψ	Strain energy

Roman Lower Case Symbols

a	Aperture radius
b	Surface curvature tensor
g	Surface metric tensor
h	Bulge height
l	Lead of ball screw
p	Hydrostatic stress
s	Arc length
t	Thickness
t_0	Undeformed thickness
$v_{i,ii}$	Principal curvature directions

Roman Upper Case Symbols

F_a	Axial force
I_B	First invariant
II_B	Second invariant
P	Pressure
R	Radius
T	Torque
V	Volume

Abbreviations

ADC	**A**nalogue to **D**igital **C**onverter
BISRU	**B**last **I**mpact & **S**urvivability **R**esearch **U**nit
DIC	**D**igital **I**mage **C**orrelation
FPS	**F**rames **P**er **S**econd
LED	**L**ight **E**mitting **D**iode
RPM	**R**evolutions **P**er **M**inute
TTL	**T**ransistor-**T**ransistor **L**ogic
UG	**U**nder **G**raduate

Chapter 1

Introduction

1.1 Background and Motivation

The material properties of skin are of great importance to a variety of fields such as dermatology and reconstructive surgery. Skin provides critical roles in protecting the body from the environment and biological pathogens and houses many sense organs such as pressure, pain and temperature receptors. Better understanding into the mechanical properties of skin leads to advancements in novel therapies for skin diseases and wounds. In addition the understanding of the properties of skin is also an advantage to the development of computational models used to simulate injuries and various diseases. Relatively little infrastructure and expertise exists in South Africa for testing skin or membrane tissues, forcing clinical researchers to rely of data from international studies. Locally relevant treatments, such as growing artificial skin for treating burn victims from informal settlement fires, would benefit from access to testing facilities for their treatments. This project seeks to expand on expertise and infrastructure on this topic of research.

The difficulty of testing the material properties of skin is the non-uniformity and anisotropy across specimen location and subjects. The anisotropy is largely due to the natural tension lines and collagen content of each skin specimen. Collagen fibres are mostly responsible for the anisotropic mechanical response of skin under larger strains. At low strains there are a number of factors that contribute to the response. The anisotropy of skin can be measured by tensile testing of samples cut in different orientations, while the individual samples at different orientations would be extracted from slightly different locations on the same subject. This introduces uncertainty when comparing the properties, since the properties of skin are known to vary from location and direction, even within the same subject. This uncertainty may be avoided by applying biaxial tension to a specimen. Planar biaxial tension can be achieved by controlled loading of either axis of a cruciform specimen. Bulge testing, sometimes referred to as a "bubble test" is

a popular method of applying biaxial tension to a circular specimen. It uses a positive pressure applied to a peripherally clamped specimen to deform the specimen in a balloon type manner. This method of testing has been previously used by other researches in the literature for testing human and animal skin. The mechanical response of skin is non-linear and develops three distinctly different phases: loading phase, transitional phase and linear phase. The typical loading phase exhibits large amounts of elastic deformation under very small loads followed by the transitional phase into the linear phase which shows a stiffer response.

1.2 Objectives

This project aims to enable local testing of skin at low strains and strain rates, by designing and building a bulge tester to load specimens in biaxial tension. The study is focused on lower strain rates and pressures as an initial step in a broader program at BISRU. Specimen deformation should be fully mapped out to achieve a full field strain map in 3-dimensions and the testing methodology should closely match the normal loading conditions of human skin. Clear directions and magnitudes of anisotropic behaviour should be extracted from the data analysis so that fibre directions and non-uniform responses are easily analysed.

1.3 Scope

This project is focused on designing and building a bulge testing device with a syringe pump for pressurisation. This project fits into a broader program of biological tissue testing devices at BISRU[1].

The materials used for testing in this project are limited to silicone elastomer. Silicone elastomer is a good substitute for biological skin and will be used for validation tests of the apparatus built in this project before any biological tissue is tested. (Note, the testing of biological tissue raises issues of medical ethics and is not a subject of this project.)

This project is limited to low pressure testing. Since there are other projects at BISRU focussed on high and intermediate pressure testing resulting in a need for a device capable of testing at lower pressures, the pressures dealt with in this project should not be greater than $500kPa$.

The strain rates tested in this project are limited to the quasistatic testing regime, in the range of $1 \times 10^{-3}/s$ to $1 \times 10^{-1}/s$.

[1]Other students that have worked and are working on this topic at BISRU include Aaron Graham [2], Dustin Fisher (in progress) and Jonathan Caine(in progress).

This project will focus on building experimental infrastructure and deriving material parameters directly from experimental data. Numerical simulations, and material models that require coupled simulation and experiments, are outside the scope of this project.

1.4 Outline

The chapters of this document proceed as follows:

Chapter 2 reviews the literature on skin and the methods that have been previously used to experimentally test human and animal skin.

Chapter 3 describes the various requirements and specifications required for the design of the experimental apparatus. This chapter also contains the mechanical, electrical and control system design process of this project and describes the preliminary testing of the experimental apparatus.

Chapter 4 describes the experimental methodology used in this project, including specimen preparation, calculations, analysis and graphing methods used.

Chapter 5 presents the primary results obtained during commissioning, including stress-stretch graphs, strain rate graphs, curvature plots, bulge profiles and material models.

Chapter 6 discusses the experimental results and makes comparisons of the methods used to testing biological tissue.

Chapter 7 describes the conclusions that are drawn from this project and the recommendations for future work.

Chapter 2

Literature Review

2.1 Properties and Structure of Skin

Skin is a critically important organ with regards to protection from the environment we live in. From ultraviolet sunlight to foreign bacteria and pathogens, our skin is the first and most important barrier of protection. This complex organ houses almost all our sense receptors such as pain, temperature and pressure receptors which all feed critical information to our brains about the environment around us.

2.1.1 Layers

All biological skin consists of three main layers: the epidermis, dermis and hypodermis. Each layer contains different micro-structures resulting in significantly different macro responses. The epidermis layer is a thin top layer which can be broken up further into two layers, the stratum corneum and viable epidermis [3]. The stratum corneum consists of mostly non-viable cells that form a physical barrier of protection from pathogens and other external agents. The Dermis layer, underneath the epidermis, is considered to be the most significant structural layer. The dermis is composed mostly of collagen, elastic and reticulin fibres, which are the major contributors to the mechanical response of skin. The lowest layer, the hypodermis, consists of mostly fat and energy storage as well as containing the majority of receptors found in skin. All layers of skin contain blood vessels and nerve endings as well as hair follicles and glands which protrude though all layers to the surface [3].

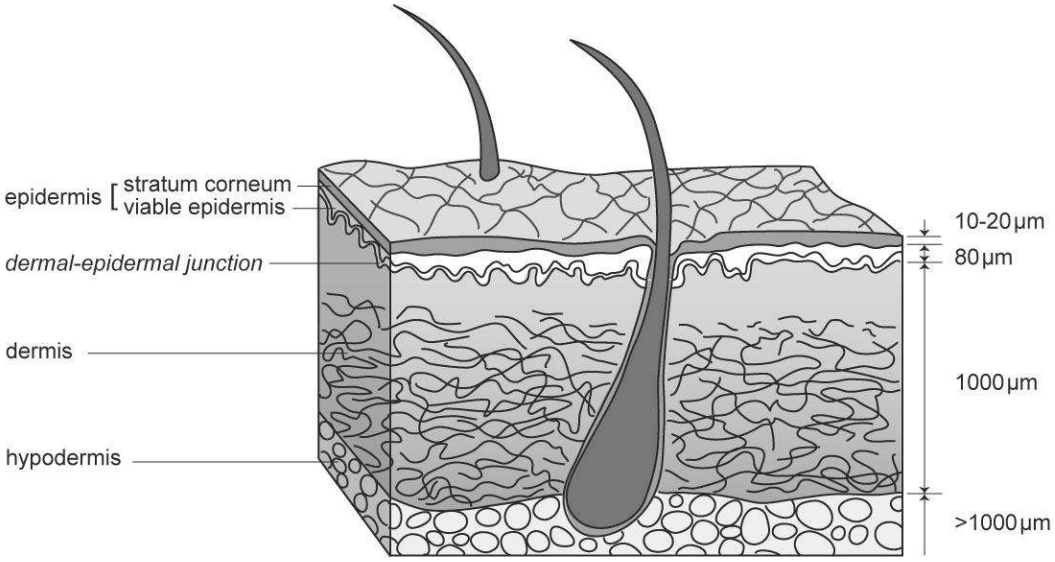

Figure 2.1 Diagram showing the layers that make up skin [3].

2.1.2 Typical Mechanical Response

The stress strain response of skin is shown to take on a J-shaped curve by many studies [4][5][6][7]. This J-shaped curve develops three identifiable phases: loading phase, transitional phase and linear phase. The loading phase presents a less stiff phase where relatively small loads result in large deformations. This response is mostly due to the properties of elastin as the collagen fibres are still coiled and unaligned and hence do not contribute much to the stiffness. As the collagen fibres begin to straighten and align the response begins to stiffen as seen in the transitional phase. Once the collagen fibres are mostly aligned the response of skin now becomes reliant on the properties of the collagen fibres. This tertiary response is almost linear, hence is called the linear phase.

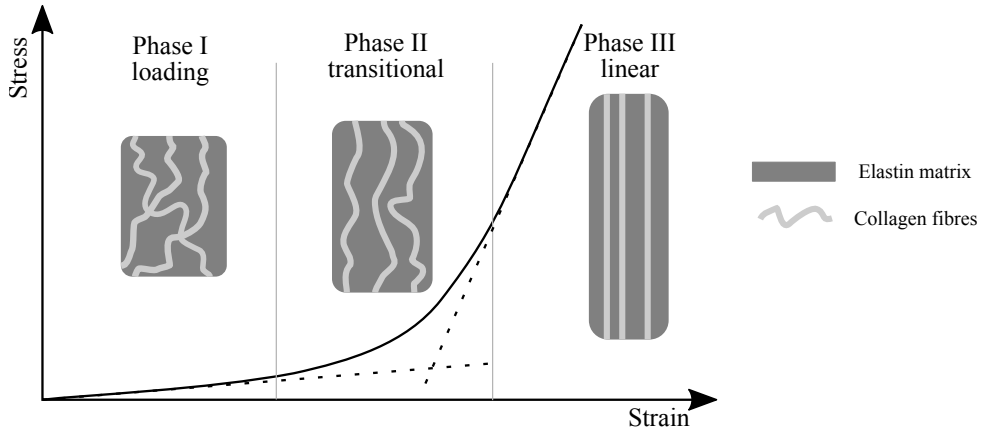

Figure 2.2 Schematic adapted from Delalleau *et al.* [8] showing the typical phases seen in the mechanical response of skin tissue.

2.1.3 Langer Lines

The Langer lines or natural tension lines, were first documented by Austrian anatomist Karl Langer, who mapped these lines using puncture wounds and chemical treatment to the skin of cadavers [9]. These lines have since been found to correspond to the maximum principal stress direction and the direction of minimum strain of specimens stretched in biaxial tension [4][5][7]. These natural tension lines can also be determined when specimens are extracted from a body. A circular specimen that has been extracted will deform into an ellipsoid with the minor axis corresponding with the orientation of the Langer lines [5]. Tonge *et al.* [4] compared three specimens from known locations and found their stiffest direction to correlate with Langer lines. Reihsner *et al.* [5] found that the deviation between the maximum principal stress and the Langer line direction was between -10 ° and 10 °. Langer lines are similar across all humans and can be approximated according to body maps such as Figure 2.3. The study by Ní Annaidh *et al.* [10] tested uniaxial specimens cut from the back of human subjects. The results seen in Figure 2.4 show that specimens cut parallel to the Langer lines show a stiffer response than the specimens cut perpendicularly to the Langer lines.

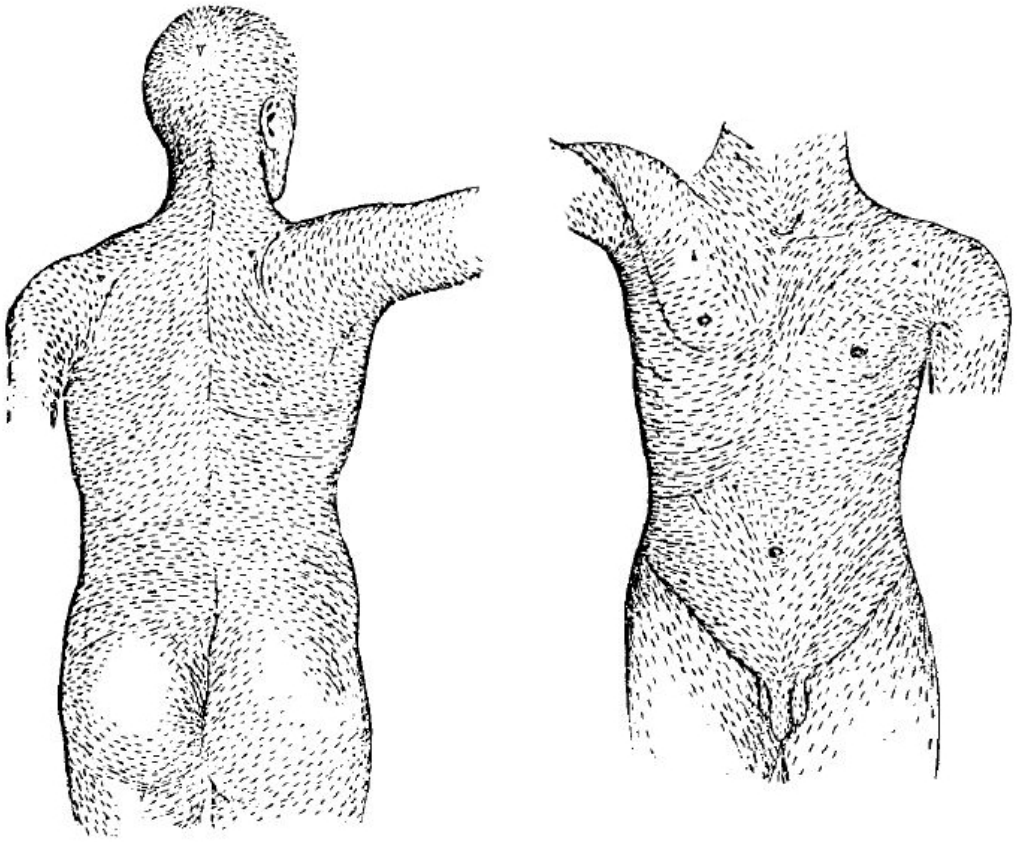

Figure 2.3 Schematic showing the Langer lines over the front and back of the human body [9].

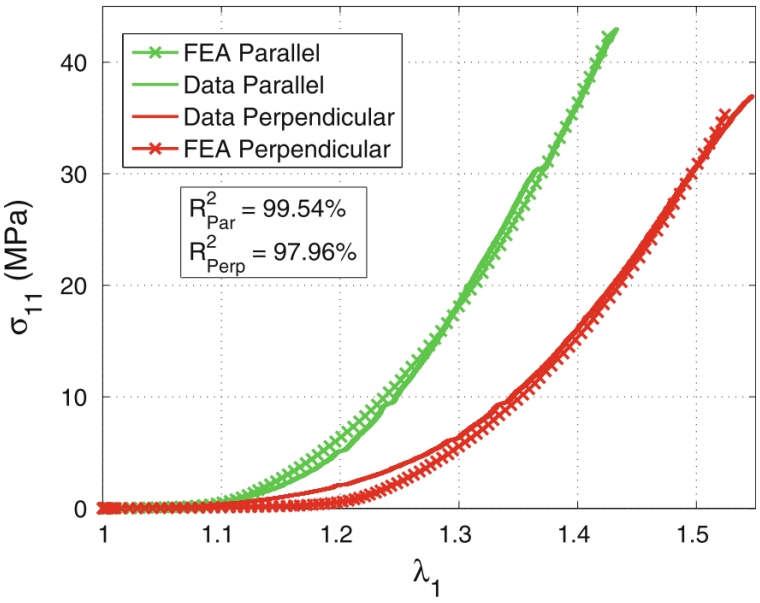

Figure 2.4 Graph showing the difference in stretch-stress response between human skin specimens cut parallel and perpendicularly to Langer lines [10].

2.1.4 Age and Location

Age and location of skin on the body have both been shown to affect the properties of skin. Sugihara *et al.* [11] compared extensibility of different locations across male subjects between the ages of 3 months to 73 years old and found certain locations to have no significant correlation to age while the majority of locations did. Tonge *et al.* [4] found that the age of the donor played a large role, observing that specimens from older donors were found to be stiffer and more anisotropic than younger donors. Reihsner *et al.* [5] compared sixteen different body locations of five individuals ages 30 to 80 years old. The study found the patella, abdomen and shoulder locations to have the highest degree of anisotropy. Opposite anatomical sites of the upper arm, thigh and calf were found to have the most significant difference in maximum and minimum principle stretches.

2.2 Mechanical Properties of Skin and Testing Methodologies

The different methods for testing the mechanical properties of skin may be split into *in vivo* and *in vitro* methods. *In vivo* refers to testing tissue in its natural biological environment, on a living body. The boundary conditions for *in vivo* tests are hard to define since the skin is still attached to the layers and flesh below.

In vitro testing involves extraction of tissue from the body and testing it independently. *In vitro* methods are less complicated for determining the material properties of skin because boundary conditions are more accurately defined and specimens can be tested to failure unlike *in vivo* testing where pain and discomfort are issues. The downside to *in vitro* testing is that since the skin samples must be removed from the body, skin samples are largely limited to those extracted from deceased subjects.

Gallagher *et al.* [7] and Ní Annaidh *et al.* [12] both reviewed previous studies of *in vivo* and *in vitro* tests on human skin, which have been summarised in Table 2.1. It is assumed that Gallagher and Ní Annaidh extracted some of this data from graphs published in the original sources, where those studies were not found to present the explicit numerical data in tables or text. The summary of results shows how much spread and variation there is in the mechanical properties of human skin. *In vivo* studies can not test the skin to failure so are limited to low strain to avoid patient discomfort. Hence the *in vivo* studies only reported moduli which ranged from 0.002 MPa to 0.85 MPa. In contrast, the *in vitro* tests spanned a much larger range of stresses. The *in vitro* stress results at failure spanned at least one order of magnitude, reporting ultimate tensile strength raging from 1 MPa to 30 MPa, and failure strains from 17 % to 207 %.

Table 2.1 *Summary of literature including in vitro and in vivo studies on human skin [7][12].*

Reference	**Failure strain (%)**	**Modulus (MPa)**	**UTS (MPa)**	**Test type**
Jansen and Rottier [13]	17-207	2.9-54	1-24	*In vitro* tension
Dunn *et al.* [14]		18.8	2-15	*In vitro* tension
Vogel [15]	30 -115	15-150	5-32	*In vitro* tension
Ní Annaidh *et al.* [12]	37 - 71	48.4-118.2	13.2-30	*In vitro* tension
Jacquemoud *et al.* [16]	27 - 59	19.5-87.1	5.7-12.6	*In vitro* tension
Agache *et al.* [17]		0.42-0.85		*In vivo* torsion
Diridollou *et al.* [18]		0.12-0.25		*In vivo* suction
Khatyr *et al.* [19]		0.13-0.66		*In vivo* tension
Pailler-Mattei *et al.* [20]		0.0045-0.008		*In vivo* indentation
Zahouani *et al.* [21]		0.0062-0.0021		*In vivo* indentation

2.2.1 Uniaxial Tension

Many studies into the properties of skin have been done using uniaxial tension [7][12][22]. Equipment for uniaxial tensile testing is commonly available in engineering laboratories conducting material testing. Well defined boundary conditions and simple calculations make results relatively easy to obtain. DIC can be used to better analyse stain data by showing local non-uniformities in strain, whereas extensometer based measurements only yield an average displacement over the length of the specimen. Extracting dog-bone shaped skin specimens for uniaxial tensile tests is simple. However, cutting dog-bone shaped specimens limits the ability to cut specimens in multiple directions at the same location. This is seen in Figure 2.5 by Ní Annaidh *et al.* [12], showing an example of where tensile specimens were cut from the back of each subject. In order to compare specimens cut at different orientations to the Langer lines, it was necessary to cut specimens from different locations on the body. As the skin properties vary with location in the body, this limits the ability to make precise comparison about the anisotropy. Furthermore, the skin properties at the same location on different subjects also show vast differences, hence the large spread in data in Table 2.1.

Figure 2.5 Schematic showing where Ní Annaidh *et al.* [12] cut uniaxial tensile specimens from the backs of human cadavers.

2.2.2 Biaxial Tension

Biaxial tension involves pulling a specimen in more than one direction. This is most commonly done using two methods: a planar biaxial test, or a diaphragm test. A diaphragm test is also known as an inflation test or bulge test. This multi-axis type of loading is critical for testing and characterising anisotropic materials such as biological soft tissues and composite materials where loading directions impact material response. Seibert *et al.* [23] discusses how a material's mechanical response is determined by its loading condition. The different responses are bound between a lower bound (loading state of pure uniaxial tension) and an upper bound (loading state of equibiaxial tension). These responses and bounds are analysed by Seibert *et al.* [23] and seen in Figure 2.6 which shows the plane of invariants according to Treloar [24]. The figure axes I_B and II_B are the first and second invariants of the left Cauchy-Green deformation tensor. The equibiaxial (upper bound) and any deformation states between, can not be modelled with only experimental data from uniaxial tensile tests. They showed in part that uniaxial stress states could modelled using equibiaxial experimental data.

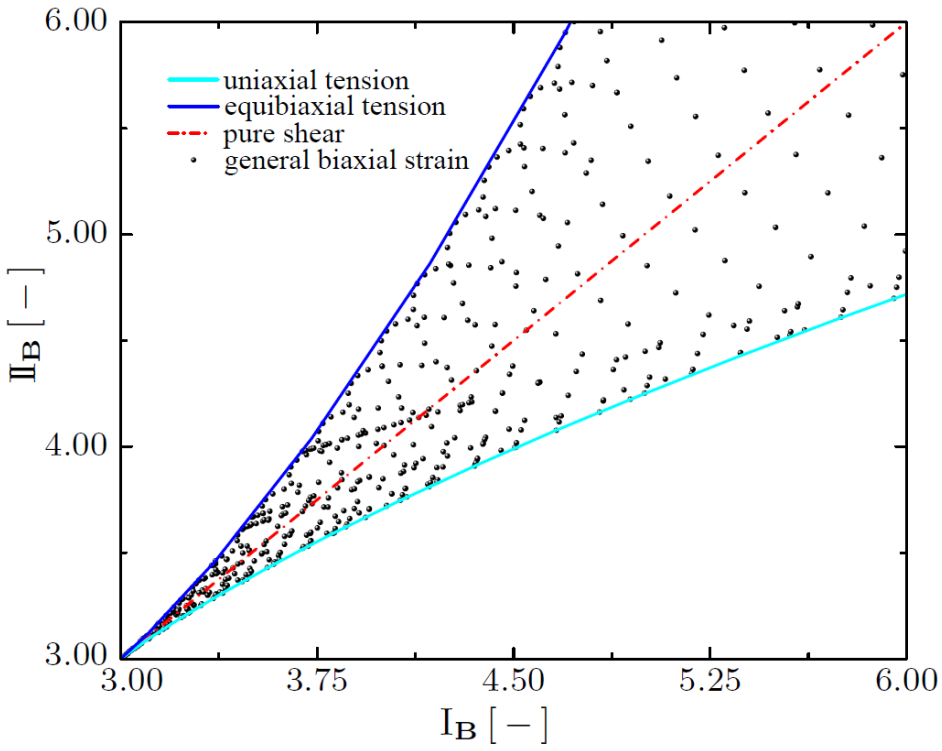

Figure 2.6 Graph from Seibert *et al.* [23] showing the plane of invariants, containing pure uniaxial tension, equibiaxial tension and loading states between.

2.2.2.1 Planar Tension

A planar biaxial test is conducted by pulling two or more axes in tension in the same plane. Examples of this are seen in Figures 2.7 and 2.8, where Reihsner *et al.* [5] loads a specimen by pulling it in twelve directions and Perez *et al.* [25] loads a sclera specimen in two perpendicular axis. The main advantage of loading specimens in planar biaxial tension is the ability to vary the loading state of each axis resulting in different combinations of stress states. This is particularly useful in testing anisotropic or directional materials such as composites and biological tissue for developing constitutive models [26].

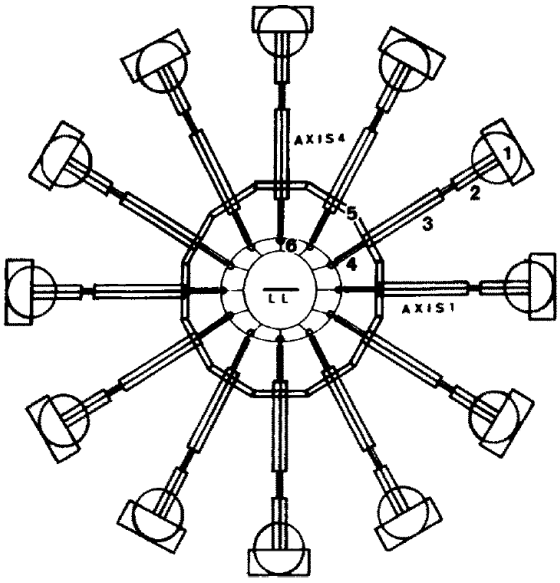

Figure 2.7 Schematic showing the 12 axis planer biaxial tension machine by Reihsner *et al.* [5].

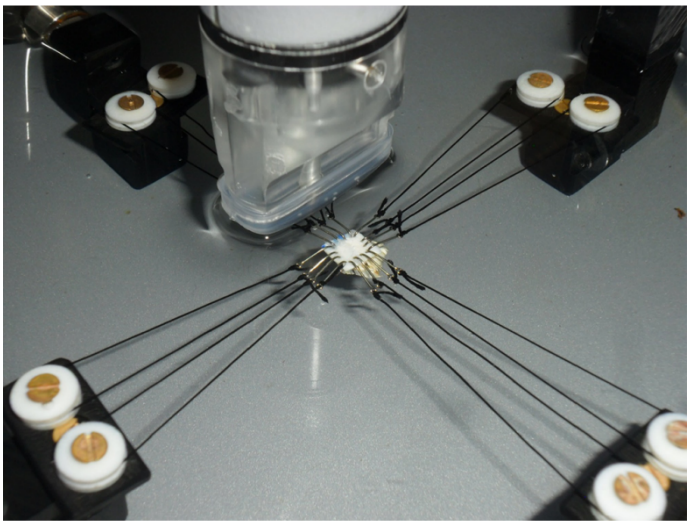

Figure 2.8 Planer biaxial test by Perez *et al.* [25] pulling a sclera specimen in two directions.

The specimens used for planar biaxial tension are commonly cut into cruciform shapes for clamping or suturing. Avanzini and Battini [26] compared different cruciform geometries and mounting methods. These specimens are large in comparison to the region of interest. An advantage of planar testing is that the specimens are loaded in pure tension without any bending effects. Sun *et al.* [6] investigated the influence of boundary conditions for soft biological tissue tested in planar biaxial tension and found clamping methods to have strong boundary effects and suture based methods to be better suited for this method of testing.

2.2.2.2 Bulge Testing

The study by Tonge *et al.* [4] investigated the properties of human skin using a bulge tester. Specimens were inflated and deformation was recorded and analysed using DIC. A commercial syringe pump was adapted to pressurise and control the pressurisation rate of specimens. The study tested six specimens and investigated preconditioning and humidity effects, concluding that neither had significant effects on results. Stress was calculated using an ellipsoidal shell model with applied pressures and curvatures measured from DIC. Stresses were calculated in the fibre and perpendicular directions to account for non-negligible stress gradients. Ellipsoids were fitted to cross sections in the fibre and perpendicular directions of the specimens to compare the differences in each of the aforementioned directions and to determine the degree of anisotropy of each specimen. A similar study by Kumaraswamy [27] conducted bulge tests on rubber and porcine skin. Porcine specimens were tested up to 13 kPa and found to have a maximum apex displacement of 10.8 mm and principal strains of 12.56 % and 9.84 %.

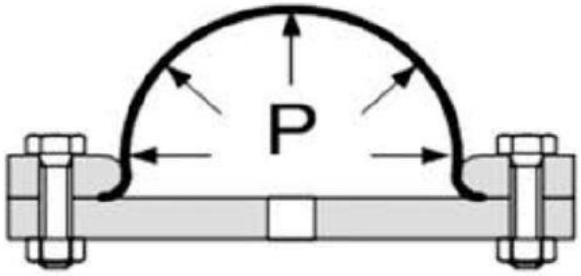

Figure 2.9 Simple schematic of a bulge test [27].

2.2.3 Other Testing Methods

Gerhardt *et al.* [28] investigated the contributions of each layer of skin to the macro response using shear testing and found that the epidermis has a 2 to 4 times higher stiffness than the dermis layer. A study by Hendricks *et al.* [29] used suction tests with apertures between ø1 mm to ø6 mm and found that the epidermis layer presented a linear response. The study also found that for larger apertures the response was dominated by

the dermis layer and in tests with smaller apertures of ø1 mm, the response was dominated by the epidermis layer.

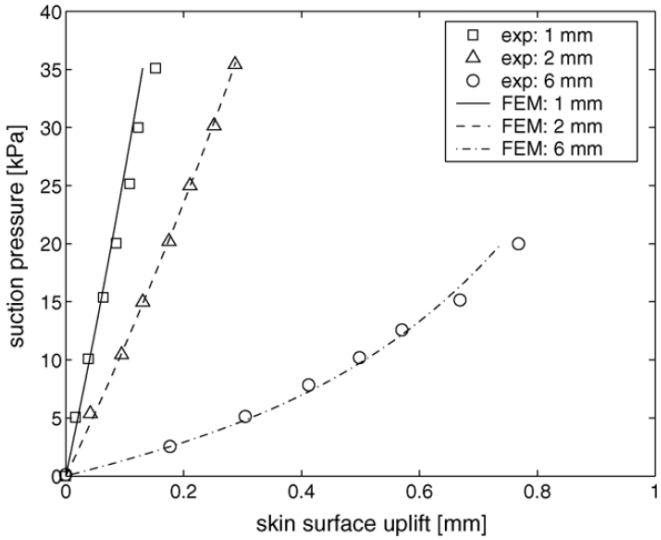

Figure 2.10 Results from Hendricks *et al.* [29] comparing tests with different aperture sizes.

2.2.4 Preconditioning

Preconditioning is a method of repeated loading and unloading of a material before testing to obtain more repeatable test results. Liu and Yeung [22] investigated the effects of preconditioning and stress relaxation of porcine skin by uniaxial tensile tests. The study found that the orientation of the fibre direction had an effect on the number of preconditioning cycles required to reach a steady state response. Specimens loaded parallel to the fibre direction were found to require fewer cycles to reach steady state than specimens loaded perpendicular to the fibre direction. Gallagher *et al.* [7] used a nine step protocol for each test that included preconditioning. However, the preconditioning was not analysed or discussed. Tonge *et al.* [4] found that preconditioning had negligible effect on bulge tests for skin. Tonge *et al.* [4] suspected that the reason for this was because the boundary conditions from clamping limits rearrangement of collagen fibres that is seen in uniaxial tensile tests.

2.3 Digital Image Correlation

Digital image correlation has become an increasingly popular non-contact method of deformation tracking in experimental testing. Calibration using a target with markers of known dimensions and relative orientation is used to determine a coordinate system and spatial positioning of each camera. For standard set-ups, one camera is required for 2D deformation analysis and a minimum of two cameras are required for 3D deformation

analysis. It is possible to use one camera for a 3D analysis by using mirrors, as described by Yu and Pan [30]. Each image is broken up into facets of $n \times n$ pixels located with centres at grid spacing of $m \times m$ pixels. Each facet should contain a random speckle pattern, which allows tracking of the entire surface rather than a set of distinct points or line markers in a grid.

The accuracy and error are improved by using cameras with better resolution and frame rates appropriate to the strain rate of the deforming specimen. The speckle pattern (stochastic pattern) is another aspect which can greatly influence the resolution and error of a DIC evaluation. It is generally not possible to track individual pixels between two cameras since a pixels grey value is likely shared with many other pixels on the same image, hence why facets (groupings of pixels) are analysed [31]. Sutton [31] states that the key to a good speckle pattern is high information content. Finer speckle patterns will mean higher surface information. This permits a smaller facet size and grid spacing and thus better resolution. The limit is that the speckle size is at least two to three times larger than the size of a single pixel.

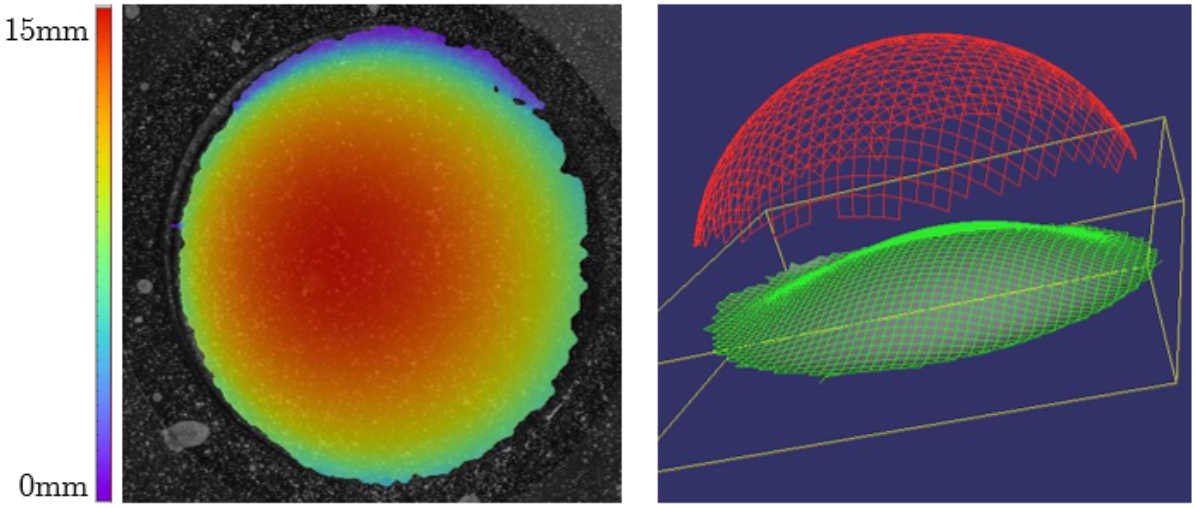

Figure 2.11 Graphics from Istra4D DIC software showing a height map and visualisation of deformation.

2.4 Curvature Calculations

In testing that involves bulging a specimen and capturing surface displacement, the curvatures of the surface becomes an important variable in calculating stresses. As in the study by Tonge *et al.* [4] and other similar studies, curvature values at a point or in a direction are used to in calculating membrane stresses as in Equation 2.1 where P is pressure, t is thickness and κ is curvature. DIC is a useful tool for calculating surface dis-

placement fields but does not output curvature values so methods of calculating curvature are needed.

$$\sigma_m = \frac{P}{2t\kappa} \tag{2.1}$$

A study by Machado *et al.* [1] tested a silicone material and used an approach of evaluating the Gaussian curvature of each point of a DIC evaluation by evaluating the first and second fundamental forms of a surface ($\mathbf{g}$ and $\mathbf{b}$ in Equation 2.2). This approach resulted in attaining principal curvature magnitudes in the maximum and minimum principal curvature directions. These principal directions were assumed to be in the circumferential and meridional directions, under the assumption of antisymmetric bulge behaviour. By furthering this approach by Machado *et al.* [1], the principal directions of curvature and magnitudes can be solved directly by solving the eigenvalue problem in Equation 2.2, where κ_i and κ_{ii} are the maximum and minimum curvatures and v_i and v_{ii} are their respective directions.

$$[\mathbf{g} - \kappa_{i,ii}\mathbf{b}]\,\mathbf{v}_{i,ii} = \mathbf{0} \tag{2.2}$$

This method can then be used on non-uniform and anisotropic deformation fields rather than only for symmetrical bulges where directions can be assumed. This is useful for testing collagenous tissue which commonly shows bisymmetrical deformation thus capable of determining the axes corresponding to fibre and perpendicular directions that are commonly described for skin.

2.5 Constitutive Models

The simplest constitutive models for skin use bi-linear elastic models [4][12][14], where two elastic moduli are used to represent the first and third phases of the mechanical response, as discussed in Section 2.1.2. Non-linear, hyperelastic models such as Mooney-Rivlin, neo-Hookean and Ogden models are also commonly used to model skin [32]. These models are also used to model rubbers but Ogden is generally better suited for most rubbers. The Ogden material model derives stress-strain relationships by means of a strain energy density function as in Equation 2.3.

$$\Psi = \Psi(\lambda_1, \lambda_2, \lambda_3) = \sum_{p=1}^{N} \frac{\mu_p}{\alpha_p}(\lambda_1^{\alpha p} + \lambda_2^{\alpha p} + \lambda_3^{\alpha p} - 3) \tag{2.3}$$

The three principal stresses σ_a (a=1,2,3) of the Cauchy stresses are calculated by Equation 2.4 where p (hydrostatic stress) can be calculated by setting $\sigma_3 = 0$ for uniaxial or biaxial stress cases. The incompressible strain condition for biaxial stress is $\lambda_3 = (\lambda_1\lambda_2)^{-1}$ and the incompressible strain condition for uniaxial stress is $\lambda_2 = \lambda_3$ therefore $\lambda_3 = \lambda_1^{-\frac{1}{2}}$.

$$\sigma_a = -p + \sum_{p=1}^{N} \mu_p \lambda_3^{\alpha_p} \tag{2.4}$$

The biaxial stresses in the first and second principal directions at the apex of a bulge can be calculated with Equations 2.5 and 2.6 as derived in Holzapfel [33] where N determines the number of terms, μ_p are shear moduli and α_p are dimensionless constants. The uniaxial stress can be calculated with Equation 2.7.

$$\sigma_1 = \sum_{p=1}^{N} \mu_p \left[\lambda_1^{\alpha p} - (\lambda_1\lambda_2)^{-\alpha p}\right] \tag{2.5}$$

$$\sigma_2 = \sum_{p=1}^{N} \mu_p \left[\lambda_2^{\alpha p} - (\lambda_1\lambda_2)^{-\alpha p}\right] \tag{2.6}$$

$$\sigma_1 = \sum_{p=1}^{N} \mu_p \left(\lambda_1^{-\frac{\alpha_p}{2}} + \lambda_1^{\alpha_p}\right) \tag{2.7}$$

There are other more advanced constitutive models such as Gasser-Ogden-Holzapfel that require coupled experiments and simulations, which is beyond the scope of this project.

Chapter 3

Design of Experimental Apparatus

The experimental apparatus designed in this project consists of an inflation chamber that clamps the specimen, a syringe pump to pressurise the inflation chamber and an electronic control system to control the motor on the syringe pump and record data from the sensors. The syringe pump, inflation chamber and electronics were designed and manufactured as part of this project. It is worth noting that the syringe pump and inflation chamber were designed as an initial prototype and not the final design, however the initial prototype met all design criteria. This chapter describes the whole design process from requirements to initial testing.

3.1 Requirements

This study forms part of a broader research plan for testing membrane tissue at BISRU. Where this project involves low strain rates, there are other projects focused on developing devices for testing skin and membrane tissue at intermediate and high strain rates. Since the aim of this project is to build a device that is capable of testing human skin it must be taken into consideration how and where the testing will take place. The high priority requirements include the specimen diameter, inflation rate, pressure and resolution as these design metrics will be used as the foundation of the device specifications and capability. A summary of the design requirements and metrics is seen in Table 3.1.

Table 3.1 *Summary of design requirements for the experimental apparatus.*

Number	Requirement	Value
RQ 1	Specimen diameter	ø10 mm to ø50 mm
RQ 2	Inflation rate	5×10^{-2} ml/s to 5 ml/s
RQ 3	Maximum pressure	500 kPa
RQ 4	Min pressure resolution	1 % of maximum pressure for sensor fitted
RQ 5	Maximum dimensions	$400 \times 400 \times 400$ mm
RQ 6	Maximum mass	15 kg
RQ 7	Min sample rate	60 Hz
RQ 8	Min stroke length	70 mm
RQ 9	Maximum piston force	400 N
RQ 10	Cleanability	All wetted parts can be disassembled using basic hand tools (spanner, screwdriver, hex key)

3.1.1 Specimen Diameter

The specimen size is important since it affects many testing parameters such as syringe volume, camera lens selection, inflation rate and volumetric resolution. Foremost the size of a skin specimen is limited by the size of the donor body and the location it is extracted from. Since the properties vary so much at each location on the body it is important to be able to test specific parts of the body independently to attain reliable data about each location. Anatomically opposite areas of the body have been found to have greatly different properties. For example, the flexor and extensor sides of the arm show vastly different responses [5] and yet they are of the order of 50 mm to 100 mm apart. Tonge *et al.* tested specimens of 100 mm×100 mm and Kumaraswamy [27] tested specimens between ø45 mm and ø80 mm. Both of these studies used commercial syringe pumps which are only capable of low pressures of the order of 30 kPa. The custom built syringe pump built for this project will be capable of much higher pressures and hence can test smaller diameter specimens, that will have a stiffer global response. The diameter range for this project is to be between ø10 mm and ø50 mm. This range of specimen sizes will mean that more specimens can be tested from a limited amount of tissue and further studies can be conducted on the affect of specimen size. Modification for testing larger specimens could be easily incorporated into the inflation chamber, with the more significant restriction to specimen size being the syringe volume. To simplify sanitary requrements disposable syringes are used and the most commonly available syringes available have volumes between

1 ml and 60 ml. A ø50 mm specimen bulged to hemisphere (57 % strain) corresponds to 32 ml of volumetric displacement. Hence a 60 ml syringe is capable of bulging a ø50 mm specimen past 60 % strain which is sufficient for this project.

3.1.2 Strain Rate and Inflation Rate

This project is focused on testing at low strain rates, of the order of 1×10^{-3} /s to 1×10^{-1} /s. Since a bulging surface typically does not strain uniformly, it should be noted than in the design phase the strain rates are estimates of averages across the specimen. A specimen being inflated at a constant volumetric rate will not maintain a constant strain rate due to the ratio of change in volume and change in surface area of a spherical shape. The strain and strain rates are estimated by analysing the change in arc length across a mid section of a bulging specimen for a given change in volume. It is assumed that a specimen clamped in a circular aperture will bulge into a spherical cap assuming an incompressible working fluid (water) in the system . The arc length can be calculated at a given inflation volume. A sphere of diameter between infinity and the aperture diameter is able to protrude through the aperture and the volume of the spherical cap that protrudes increases with a decrease in sphere diameter. An example of this is seen in Figure 3.1.

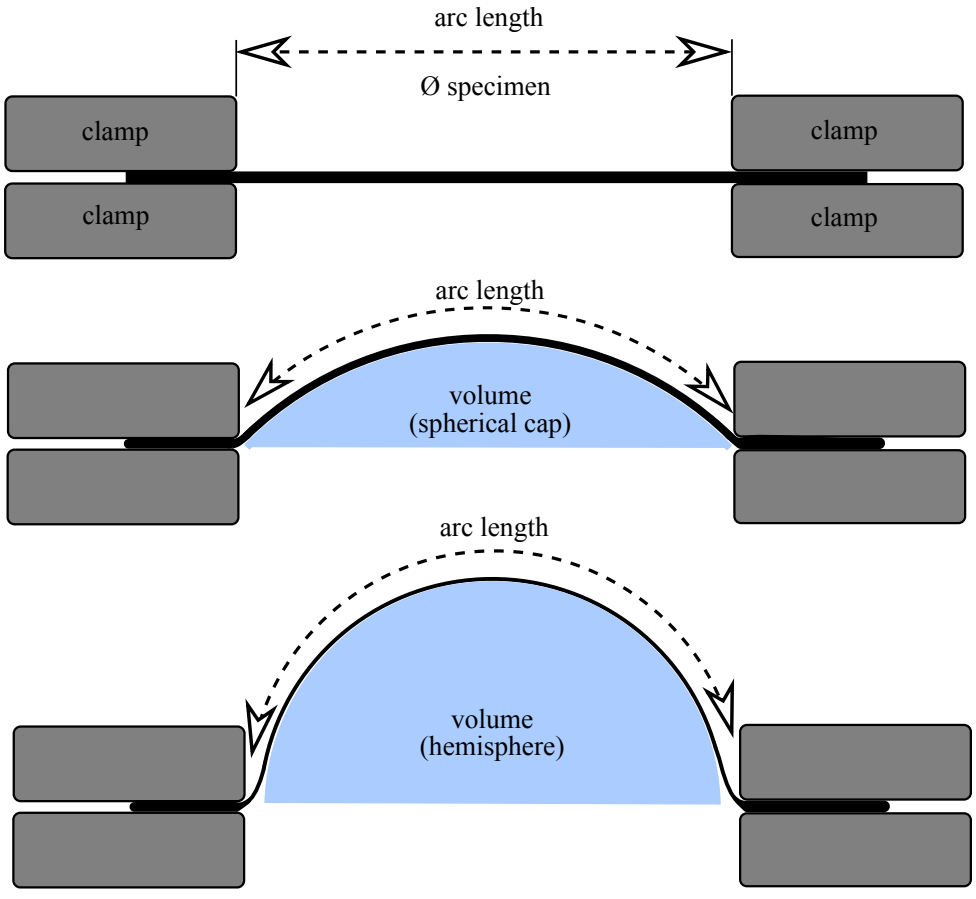

Figure 3.1 Schematic showing a bulge test with assumed spherical bulge.

The volume of a spherical cap is calculated with Equation 3.1 where a is the aperture radius and h is the height of the spherical cap. The cubed-root equation is used to solve h for a given volume with Equation 3.2. The radius of a sphere is calculated from h and a in Equation 3.3 and the arc length can then be calculated with Equation 3.4. From these, the arc length for a given inflation volume is calculated and hence strain and strain rate can be calculated given a volumetric inflation rate. This approximation is valid while the deformation remains within a hemisphere ($h <= a$).

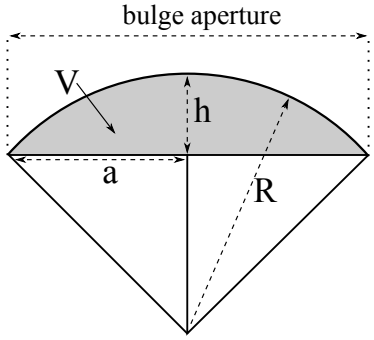

Figure 3.2 Diagram of spherical cap geometry.

$$V = \frac{\pi h}{6}(3a^2 + h^3) \tag{3.1}$$

$$h = \sqrt[3]{\left(-\frac{3V}{\pi}\right) + \sqrt{\left(-\frac{3V}{\pi}\right)^2 + a^6}} + \sqrt[3]{\left(-\frac{3V}{\pi}\right) - \sqrt{\left(-\frac{3V}{\pi}\right)^2 + a^6}} \tag{3.2}$$

$$R = \frac{a^2 + h^2}{2h} \tag{3.3}$$

$$s = 2R \arcsin\left(\frac{a}{R}\right) \tag{3.4}$$

By plotting strain vs strain rate graphs for constant inflation rates, as estimate of required inflation rates can be obtained to achieve strain rates in the rage $1 \times 10^{-3}/s$ to $1 \times 10^{-1}/s$. The strain rate curve for a inflation rate of 0.0 5ml/s is plotted in Figure 3.3. The curve shows the strain rate increasing at a high rate until a strain of 0.15, after which the rate appears to remain fairly constant at a rate of $1 \times 10^{-3}/s$. The graph for an inflation rate of 5 ml/s was found to achieve a strain rate of $1 \times 10^{-1}/s$ in the near constant region.

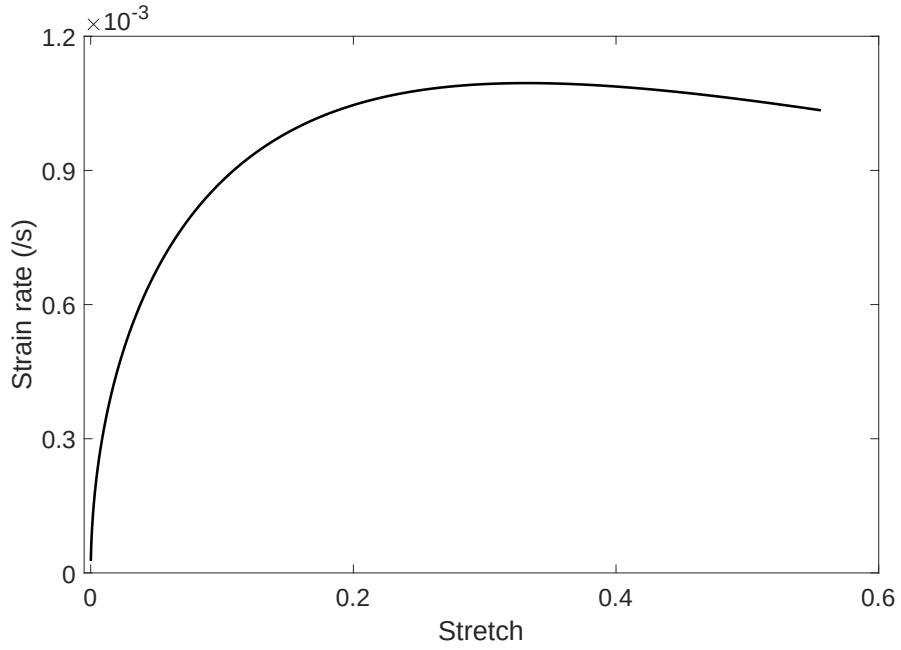

Figure 3.3 Estimated stretch vs strain rate for a constant volumetric rate of 0.05 ml/s.

3.1.3 Pressure and Accuracy

The literature does not clearly show what stresses and pressures to expect when testing skin. The summary in Table 2.1 shows that studies have found the elastic modulus of skin to range from 0.0045 MPa to 150 MPa. Two relevant studies that both did bulge testing on skin; Tonge *et al.* [4] and Kumaraswamy [27], tested up to 5 kPa and 14 kPa respectively. These pressures are lower than the pressures that would be expected for the material parameters from the literature summaries in Table 2.1.

Since a plastic syringe would likely be the limiting component for the syringe pump, a standard 60 ml syringe was manually pressure tested and found to be capable of reaching at least 800 kPa before the plunger arm began deforming. Considering that the syringes are capable of significantly higher pressures than the maximum pressures Tonge *et al.* [4] or Kumaraswamy [27] tested to, a maximum driving pressure of 500 kPa is suitable for this project. The pressures ranges expected for testing silicon in this project are in the range of 10 kPa to 100 kPa. The accuracy of the sensor used to measure the pressure should be high since the expected pressures vary to a large degree. Ideally, more than one pressure transducer should be available for testing so that a transducer with a more suitable pressure range is used in each case. An accuracy of at least 1 % of the maximum test pressure is required for the pressure transducer used.

3.1.4 Portable

To avoid the logistics of transporting and storing skin specimens, it would be preferable to transport the testing apparatus to clinical sites where the skin specimens would be harvested. This would enable testing as soon as possible after harvesting, reducing complications such as tissue degradation or likelihood of tissue contamination. UCT Medical School is one clinical site that is likely to be used for harvesting and testing skin specimens, since it already has surgical facilities. The bulge testing apparatus should be small enough to be carried and set up by one person, hence as a rough guide the maximum weight for the whole device should no exceed 15 kg [34] and should fit into a container of dimensions $400 \times 400 \times 400$ mm for easy transport in a standard vehicle.

3.1.5 Sampling Rate

The Basler cameras that are available in the department for DIC are capable of a maximum of 60 FPS. The minimum sampling rate should be at least 60 Hz to ensure that there is at least one pressure data point for each image captured. The limiting factor for sampling is that the Basler cameras available have a limiting factors of 60 FPS. In order to assure at least one data point captured per frame, the pressure and any other parameters should be sampled at at least 60 Hz.

3.1.6 Syringe Stroke Length

As standard plastic syringes will be used to pressurise the inflation chamber, the stoke length for the syringe pump should be capable of at least the stroke length of the largest syringe available for testing. The largest syringe commonly available and likely to be used for this project is a 60 ml syringe that has a stroke length of 70 mm.

3.1.7 Maximum Piston Force

The maximum pressure required for this device is 500 kPa, hence the syringe pump should be capable of exerting sufficient force to achieve 500 kPa. Larger syringes have larger diameters which will result in higher piston forces required to reach 500 kPa. The largest syringe available is a 60 ml syringe with a diameter of 30 mm. This syringe will require a 353 N piston force to exert a pressure of 500 kPa. A maximum piston force of at least 400 N is required.

3.1.8 Inflation Chamber Easily Disassemblable

When working with biological tissue it is important to keep everything clean and not leave biological matter on any equipment. Rotting tissue is a health concern and can

lead to contamination of specimens and should be avoided. Thus all the equipment that is exposed to the skin specimens should be easily cleaned and sterilised after use. The inflation chamber, syringe and tubing are the only parts what would be in contact with tissue or fluid that might be contaminated and need to be cleaned. The syringe is a stock item that can be easily cleaned or disposed and replaced. The tubing can be easily cleaned by running a sterilising agent through the tubing. The inflation chamber and clamps are not disposable and should be designed so that they can be easily cleaned. These parts should also be constructed from a suitable material such as stainless steel which is commonly used in sterile applications because it is non-porous and does not corrode or react to most cleaning products.

3.2 Mechanical Design

The mechanical design of the bulge tester built for this study includes design of an inflation chamber and a syringe pump that are connected together with a high pressure hose. The inflation chamber is designed for clamping specimens between ø50 mm and ø10 mm although it would be easy to manufacture an adaptation to clamp large specimens if needed. The syringe pump is designed with the syringe being the weakest and limiting component in the design. A ball screw and stepper motor are used for high accuracy and efficiency with zero backlash. The basic workings of the mechanical design are shown in Figure 3.4.

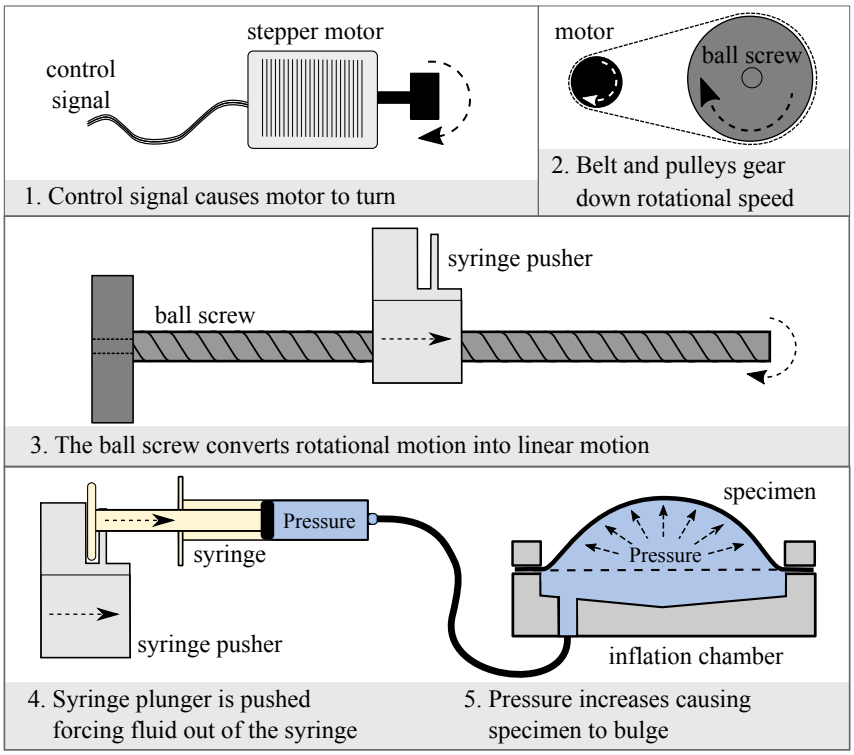

Figure 3.4 Schematics explaining the basic workings of the mechanical apparatus.

3.2.1 Inflation Chamber

The main purpose of the inflation chamber is to clamp and seal a specimen in place for pressurised testing. The inflation chamber consists of a main body, clamp plates and inlet/outlet ports. The main body has an inner diameter of 76 mm and depth of 5 mm with a tapered floor to allow for drainage and purging of air when inverted. A T-piece connector is connected to the centre port of the main body for connecting a pressure transducer and ball valve which is used for draining or purging air. The pressure transducer is located 35 mm below the bottom surface of the specimen in the same horizontal plane. All threaded connections use G1/4 inch tapered thread, which it is a common thread for many different pressure connectors. The second port on the bottom of the main body located off centre, is used as the fluid input port from the syringe pump. A specimen is sandwiched between two clamp plates, both with the same inner diameter which is called the aperture diameter. The main body has a 85mm O-ring grove for sealing with the bottom surface of the lower clamp plate. The silicone specimen seals itself against the top of the lower clamp plate and the upper clamp plate is clamped down to the main body with six M5 bolts. The upper inner edge of the upper clamp plate has a large chamfered for better viewing angles and lighting for Digital Image Correlation. The inflation chamber assembly is attached to a 3D printed stand for support and to enable easy inversion for filling and purging of air. When inverted the specimen surface will be facing downwards and the ball valve is

then the highest point where any air will escape when the chamber is filled from the input port.

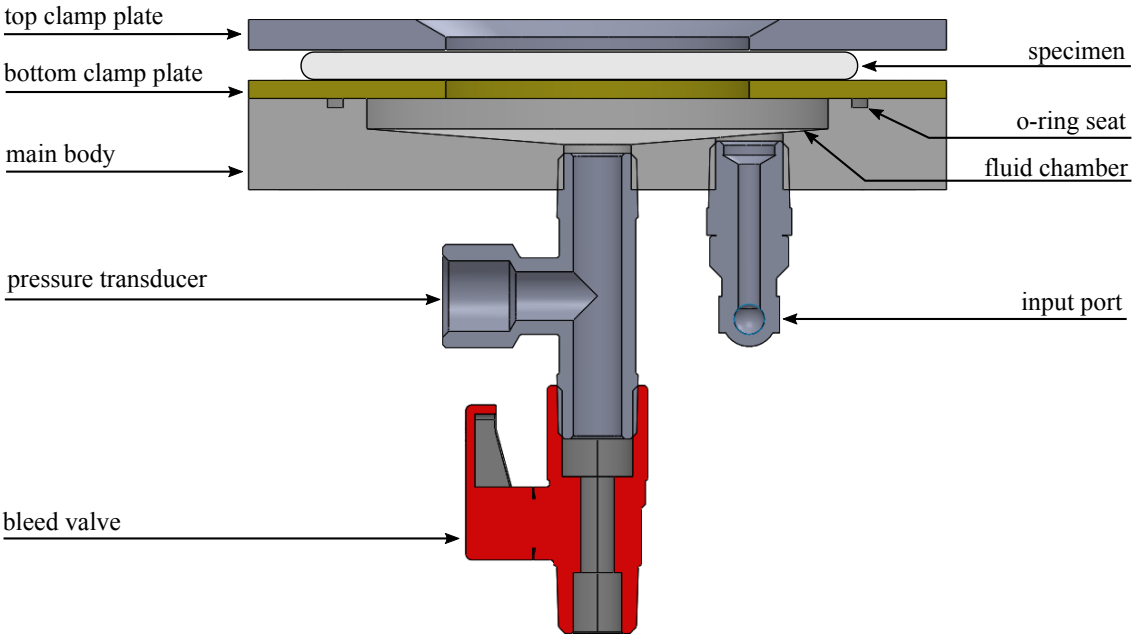

Figure 3.5 Labelled diagram of the different parts of the inflation chamber design.

3.2.2 Syringe Pump

The syringe pump was custom built as part of this project because commercially available syringe pumps do not meet the volumetric speeds, pressures and resolution requirements for this project. A SFU1204 (ø12 mm, 4 mm pitch) ball screw is used to convert the torque from the motor into a linear driving force for the syringe. The syringe pusher is attached to a platform that is guided by three linear bearings that run on two linear rails. This platform is also bolted to the ball nut which is pushed lengthways down the ball screw when the ball screw is rotated. The linear bearings are positioned in a triangular formation to counter any moments from induced by syringe plunger that would otherwise be transmitted through the ball nut and ball screw reducing efficiency. The ball screw is driven with a bipolar Sanyo Denki stepper motor that has a holding torque of 1.27 Nm and resolution of 200 step/rev. A gear reduction of 2:1 is used to half the speed of the ball screw resulting in higher position control and increased torque. This is achieved with standard GT2 pulleys and belt arrangement with a belt tensioner to mitigate backlash. This arrangement allows for the motor to ball screw speed ratio to be changed from 2:1 to 1:2 by switching pulleys, should higher speeds be required. The syringe pump has a linear travel length of 200 mm, with a linear travel resolution of 10 μm per step. This allows volumetric resolution of 7×10^{-3} ml when using a 60 ml syringe, which can be improved

by using a smaller syringe if required. The syringe pump is currently fitted with a 60 ml syringe but can be swapped out for any size syringe or a custom machined syringe.

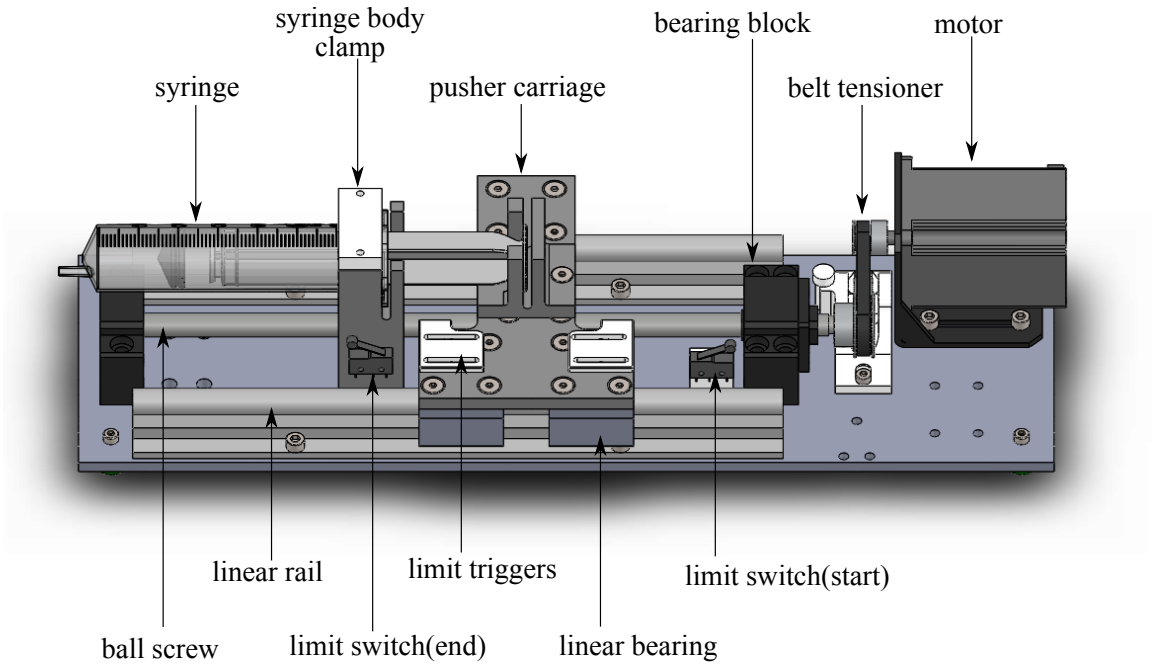

Figure 3.6 Labelled diagram showing the different parts of the syringe pump design.

3.3 Instrumentation and Control System

In order to simplify the design and implementation of the instrumentation and control system, Arduinos are used due to their abundant open-source resources for applications of this project. The instrumentation and control system consists of two Arduino Mega 2560 micro controllers. One Arduino is used for motor control, limit switches and buttons and the second Arduino is used to receive signals from the sensors, output data from the sensors to the computer and output the TTL signal used for triggering the cameras for DIC. These Arduinos are hence called the Motor-Arduino and Sensor-Arduino from this point on. Both Arduinos are linked via a serial connection and function as one control system. The electrical wiring diagram for the electronics can be found in Appendix B and the basic control system flow diagram is seen in Figure 3.7.

3.3.1 Stepper Motor and Driver

The Sanyo Denki bipolar stepper motor was chosen for its high torque and small step angle. This motor was also chosen because a rotary encoder came pre-installed on the back of the motor. This simplified the design by not having to account for and install an

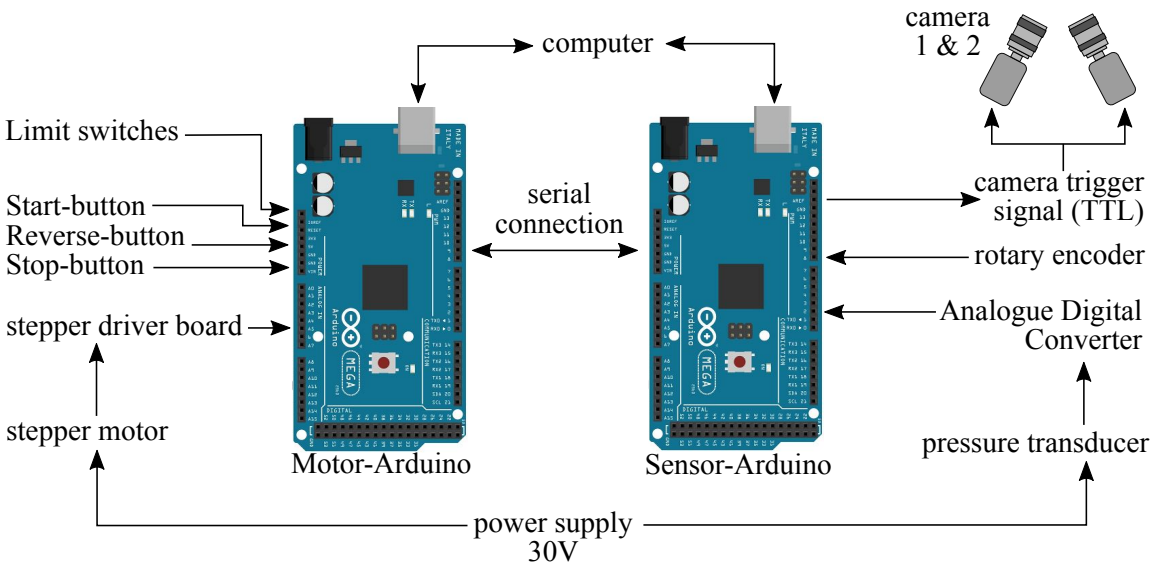

Figure 3.7 Flow diagram showing how the electronic components interface with each other.

encoder which presents its own challenges. The motor has a holding torque of 1.27 Nm, 1.8 ° step angle or 200 steps per revolution and an input voltage of 24 V to 36 V DC. The inflation rate requirements for the syringe pump of 0.05 ml/s to 5 ml/s correlate to speed requirements of 2 RPM to 215 RPM for the motor. The holding torque on the stepper motor results in a piston force of 3.1 kN when using Equation 3.5 where $l = 4 \times 10^{-3}$ m, $T = 2 \times 1.27$ Nm (double due to the gearing ratio) and $\eta = 80\%$. The maximum running torque of a stepper motor is less than the holding torque and dependant on multiple factors. The data sheet for this motor shows that it is capable of a driving torque between 1.1 Nm to 1.2 Nm for the running speeds required to meet the inflation rate requirements. This results in a minimum piston force of 1.4 kN which meets the required minimum of 400 N.

$$F_a = \frac{2\pi\eta T}{l} \tag{3.5}$$

A stepper motor driver board is used to control the stepper motor and implement micro-stepping. An Arduino CNC shield V3 is used to attach the motor driver board to the Arduino. The CNC shield is designed for plugging the motor driver boards straight into them with other circuitry and redundancies to prevent over currents and other issues. The DRV8825 stepper motor controller was chosen for enhanced motor control. The availability of excising software libraries and tutorials for the DRV8825 simplified implementation. Using a motor controller board results in easy implementation of micro-stepping which smooths the motion between steps on the stepper motor creating smoother rotation of the motor at lower speeds. After testing the various micro-stepping settings it was found that $1/8^{th}$ micro-stepping provided the best range of speeds and smoothed

rotation. The minimum and maximum speeds achievable were found to be 0.8 RPM to 350 RPM. It was found that the input and output speeds were not consistent so the motor output speeds were graphed and the input speed was calibrated for more accurate output speeds. The gear reduction results in speeds between 0.4 RPM and 175 RPM on the ball screw. Motor speeds below 0.8 RPM are possible but the steps become distinct due to the longer time between pules, resulting in jerky steps rather than smooth rotation.

3.3.2 Rotary Encoder

A rotary encoder is used to measure the speed of the stepper motor. The S-type S340 encoder came pre-installed on the Sanyo Denki bipolar stepper motor. The S340 has a resolution of 400 counts per revolution with three channel output. Two channels are used to generate quadrature signal for reading the rotational speed and the third channel is an index channel that is pulsed once per revolution. There are two methods for calculating rotational speeds of a quadrature signal, pulse counting or pulse timing. Pulse counting uses a sampling period and counts the number of pulses that are recorded for that time period and pulse timing records the time period between pulses. The pulse timing method is more accurate and better suited to lower rotational speeds because at low speeds the time difference between pulses is larger.

3.3.3 Pressure Transducer and ADC

RS Pro 100 kPa and 600 kPa pressure transducers were chosen for measuring the pressure inside the inflation chamber. These sensors were chosen because they operated within the expected pressure pressures and are easily implemented into the Arduino ecosystem. The supply voltage is 9 V to 32 V which is the same upper range of supply voltage as the stepper motor, this simplifies the power supply requirements for the control system. The output signal is an analogue signal between 0 V to 5 V which corresponds to 0 kPa to the maximum pressure rating. The pressure transducer output can be wired straight into the Arduino board but since the Arduino's on-board Analogue to Digital Converter(ADC) has a resolution of 10 bit, it was decided to use an external ADC with higher resolution. The ADS1115 ADC with 16 bit resolution was chosen to increase the resolution of the analogue signal from the pressure transducer. This ADC is commonly used with Arduinos and libraries are easily available.

3.3.4 Limits and Switches

The switch inputs for the control system include a start-button, reverse-button, stop-button and two limit switches. The two limit switches are located on each side of the linear rails to stop the syringe pump before the motor drives the pusher carriage into the

bearing blocks on each side of the ball screw which would cause damage to the ball screw, bearing blocks or carriage. These limit switches are connected to interrupt pins on the Motor-Arduino in order to stop the motor immediately. A test can be run until a limit switch is triggered without any issues and hence can be used as a stop reference for a test. The limit switch at the starting end of the rail is used to reset the syringe pump by moving a pre-set distance forward after it is triggered when the syringe pump is reversing. If the limit switch at the end of the rail is triggered, the motor and data collection will stop and the syringe pump will be held in position with full holding torque. A maximum pressure limit is programmed into the Sensor-Arduino so that if the maximum rated pressure of the pressure transducer is reached the test will stop. This is to avoid overpressure of the transducer. A stop-button is also programmed into an interrupt pin for manual stopping of a test which will also provide holding torque and stop data collection.

3.3.5 Data Output

Time, pressure and speed reading are outputted to a computer from the Sensor-Arduino via a USB connection. The data output commences when the start-button is pressed. The data is outputted for two seconds before the stepper motor is started, this is to provide a reference pressure reading. Once a test stops, the data output is also stopped and all the test data can be saved to a text file. An example of the data that is saved from a test is seen in Table 3.2.

Table 3.2 *Table showing an example of the data output from the Sensor-Arduino.*

Time	**Pressure**	**Speed**
(s)	(kPa)	(RPM)
0.01	0	0
0.02	0	0
0.03	0	0
...	...	...
2.01	0.346	5
2.02	0.9934	5
2.03	1.2537	5
2.04	1.4469	5
...	...	...

3.3.6 Coding Environment

The scripts for the two Arduinos are written in C++ which is the native language for the platform. The basic flow for the control system developed is see in Figure 3.8. There are four main functions which either start or stop a test:

1. Start-button is pressed
2. End-limit triggered OR Stop-button is pressed
3. Maximum pressure is exceeded
4. Reverse-button is pressed

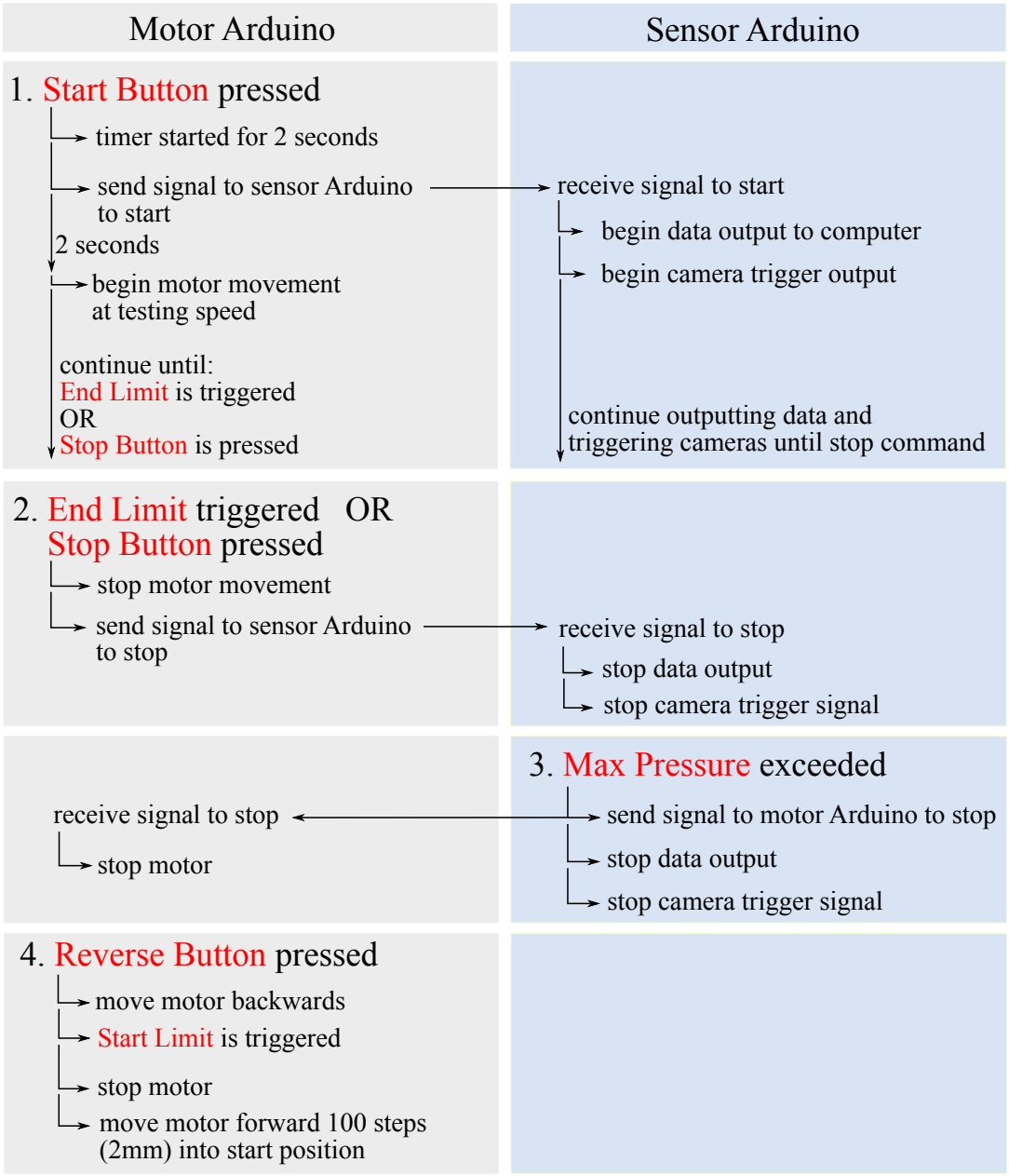

Figure 3.8 Flow diagram of the basic structure of the control system.

The following libraries are required to run the Arduino based control system. All libraries are available for download and their respective licences can be found on https://www.arduinolibraries.info/

- TimerOne (V1.1.0) - used for initiating and using the Arduino timer clock
- WireData (V1.0.0) - used for communication between the Sensor and Motor Arduinos
- StepperDriver (V1.1.3) - used to control the stepper motor
- Adafruit_ADS1X15 (V1.0.1) - used to read digital signal from the ADC

Chapter 4

Experimental Methodology

This chapter focuses on the methodology of the data processing used in this project. The analysis steps used in this project are specimen preparation and manufacture, testing protocol, set up for and the use of DIC and the data processing done in Matlab that generates the final results such as stress-stretch and curvature detection methods.

There are four main steps to attaining the final results. These steps in order are: DIC analysis, curvature calculations, stress calculations and data selection for graphing. This chapter will show how the data for a specimen is processed starting with the DIC set up and setting used. The proceeding sections of the chapter will cover the remaining steps in the processing which are done using Matlab.

4.1 Digital Image Correlation

All tests were recorded and analysed using 3D DIC for the bulge tests and 2D DIC for the uniaxial tensile tests. Istra4D DIC software by Dantec Dynamics was used to run the DIC analysis on each test. DIC determines displacement data at a user determined grid spacing. The DIC software then calculates various strain measures (e.g. engineering strains, true strains) in different orientations (global coordinates, principal directions). The process for each test is as follows: First calibration images are captured with Basler Pylon software after which a projection calibration is done in Istra4D. If the residuum [1] for the projection calibration is acceptable, then the experimental images are captured and imported into Istra4D. A correlation series is started using the calibration file and experimental images. Once suitable settings are selected the correlation analysis is run and the resulting data can be exported for further analysis. These processes are explained in more detail below.

[1] Residuum is the uncertainty (in 3D space) of the location of any given feature detected by the pair of cameras.

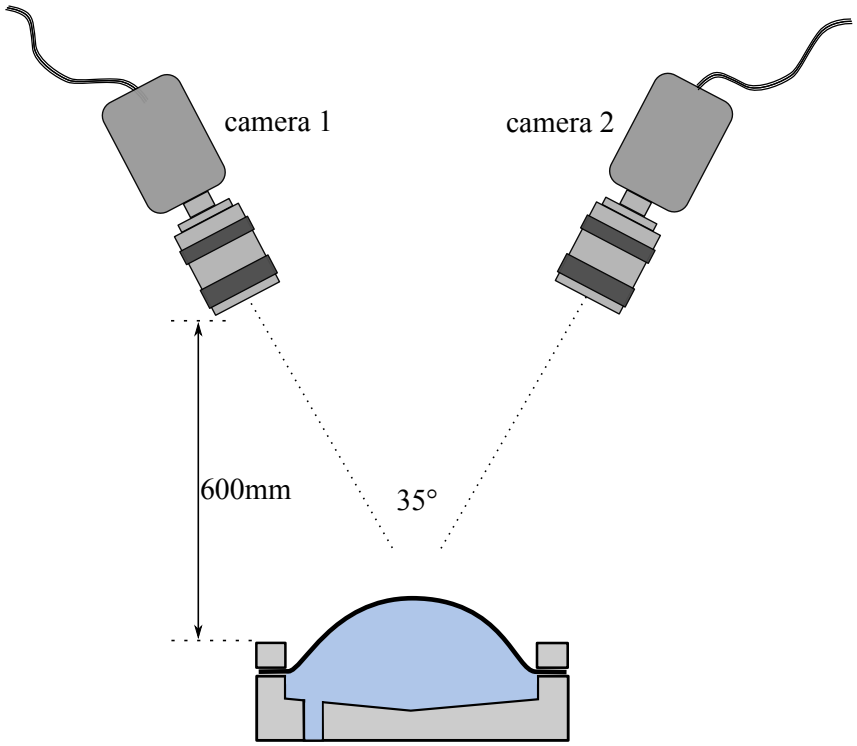

Figure 4.1 Camera positioning for experimental testing.

4.1.1 Cameras, lenses and lighting

The correct cameras, lenses and lighting set up are all important for extracting reliable data from a DIC analysis. The key parameters are the resolution, frame rate and depth of field. Two Basler acA2500-60um cameras are used for testing with Tokina 100 mm macro lenses. The cameras have a resolution of 2590×2048 pixels at a maximum frame rate of 60 FPS.

The focal length is manually adjusted on the lenses with the focus rings. The aperture is set to the smallest f-stop setting (f-32) as this would provide the largest depth of field which is important since the specimens will be bulging towards the cameras and need to stay in focus. The focal point of the lenses are set between the specimen and lens and then adjusted until the edge of the depth of field reaches the calibration target that is positioned on top of the flat specimen. Once the calibration target is in focus at the zero deformation position of the specimen, the target plate is then raised by 30 mm which slightly exceeds the expected apex height of a fully bulged ø50 mm specimen. The calibration plate should also be in focus at this position meaning that the specimen will remain in focus for as much of the test as possible. If the lenses were set for perfect focus at the flat specimen condition, it is likely that the images would be sufficiently out of focus at the hemisphere state that the DIC correlation would fail. It was found that the

lenses did not have identical aperture sizes, to mitigate this the apertures were set to f-22 as explained in Section 4.1.2.

A LED light was used to provide additional lighting because more lighting is needed at higher frame rates and smaller aperture sizes. The lighting and exposure time should be adjusted until the images are not over exposed as DIC can not distinguish between pixels that are over exposed. It was found that the silicone specimens reflected a lot of light resulting in over exposure even with low lighting levels. White marble dust was used to dust the surface of each specimen and brushed off with a soft brush. The marble dust left a matt finish on the surface of the specimen reducing the reflectivity and mitigating the overexposure caused by the reflected light. The lighting could then be adjusted to the correct level resulting in better grey value distributions across the specimen. A large piece of reflective material was wrapped around the tripods for the cameras and light to create a light-box around the specimen resulting in more ambient type light which also reduced overexposure.

4.1.2 Calibration

Calibration is a critical step in DIC, as it establishes the relative positions of the cameras in 3D space. Calibration plates are manufactured in varying sizes to suit the lenses and cameras that are used for capturing images. A calibration plate should fill up roughly one quarter of the frame. A minimum of six calibration images are needed for calibration but more images will result in a more accurate calibration. The calibration plate should be moved to different locations in the frame for each image while still being in the same plane and depth of field so that the images are all in focus. Past work at BISRU [35] showed that a residuum of greater than 0.1 is undesirable and below 0.05 is preferable.

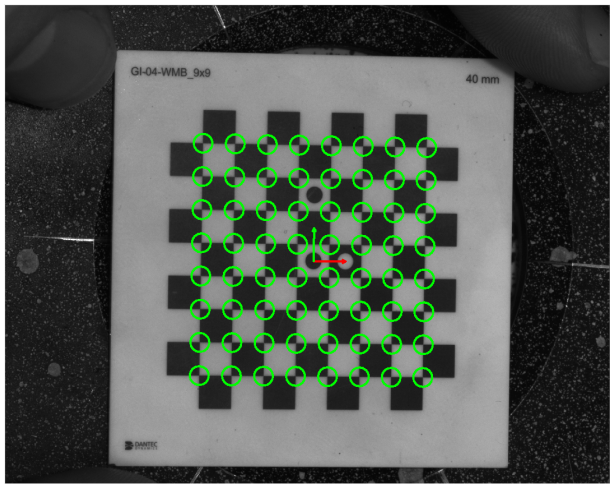

Figure 4.2 Image showing the the markers that have been found as part of a 3D calibration process in Istra4D.

Calibration was completed for each testing speed, which included three bulge tests each. The cameras were not touched or moved in between tests. However, it is good practice to calibrate for each test. Problems were encountered with the lenses that were used because the apertures size of each lens were found to not be identical to each other at the same aperture setting. This caused the calibration residuum to be higher than 0.1. The issue was fixed by increasing the f-stop to f-22. The lens with the larger aperture was set to f-32 and then to f-22 and the lens with the smaller aperture was set to f-16 and then to f-22. This used the backlash in the aperture mechanism of the lenses to reduce the difference in the aperture size. By using f-22 instead of f-32, the depth of field would be slightly reduced but the difference in apertures was reduced, resulting in greatly improved residuums. It was found that with the current set-up the depth of field was still sufficient for testing.

4.1.3 Correlation settings

Correlation is the process where the DIC software processes all the images from a test and outputs surface deformation according to the settings selected. There are many settings that need to be adjusted for a successful DIC analysis. The two most fundamental settings are the grid size and facet size (measured as squares of $n \times n$ pixels). These will determine how many grid points surface displacement will be calculated at and whether it will be able to sufficiently resolve displacements and calculate strains. The Istra4D manual states that facets should not overlap by more than one third. However, R. Curry [35] advised that the facets can overlap more than a third and an overlap of about 50 % will likely result in better correlations. This results in slightly larger facets which mean that the correlation algorithm has greater certainty in identifying the displacement of any given facet. The correlation algorithm assumes deformation is uniform over the area of a facet. If the facet is so large that the deformation varies significantly from one edge to the other, the algorithm will struggle to identify the correct displacement for the facet's centre. The settings chosen for correlation are dictated mainly by the speckle pattern, camera resolution and amount of deformation between frames.

4.2 Curvature calculations

All curvature calculations are processed using Matlab with input data from DIC. The method by Machado *et al.* [1] was followed and adapted to calculate principal curvatures and directions at each point assessed by DIC. In the study by Machado *et al.* [1], axisymmetric bulge behaviour is assumed and hence principal curvature directions are assumed to be in the circumferential and meridional directions. This project is required to evaluate the curvatures of anisotropic materials that will likely not bulge in an axisymmetric manner. In order to calculate the directions of principal curvature, the Matlab script pub-

lished Machado *et al.* [1] is adapted to solve the eigenvalue problem as seen in Section 2.4 and repeated below in Equation 4.3. The surface metric tensor $\mathbf{g}$ and surface curvature tensor $\mathbf{b}$ are calculated with Equations 4.1 and 4.2 respectively as outlined by Machado *et al.*. These tensors are used to solve Equation 4.3 where $k_{i,ii}$ and $\mathbf{v}_{i,ii}$ are the principal curvatures and principal directions respectively. The elements of $\mathbf{g}$ and $\mathbf{b}$ are calculated inside the script published by Machado *et al.* [1]. The two dimensional direction vectors $\mathbf{v}_{i,ii}$ from the eigenvalue problem are located in the $X-Y$ plane.

$$\mathbf{g} = g_{\alpha\beta}\mathbf{g}^{\alpha} \otimes \mathbf{g}^{\beta} = \begin{bmatrix} g11 & g21 \\ g12 & g22 \end{bmatrix} \tag{4.1}$$

$$\mathbf{b} = b_{\alpha\beta}\mathbf{g}^{\alpha} \otimes \mathbf{g}^{\beta} = \begin{bmatrix} b11 & b21 \\ b12 & b22 \end{bmatrix} \tag{4.2}$$

$$\left[\begin{bmatrix} g11 & g21 \\ g12 & g22 \end{bmatrix} - K_{i,ii} \begin{bmatrix} b11 & b21 \\ b12 & b22 \end{bmatrix} \right] \mathbf{v}_{i,ii} = \mathbf{0} \tag{4.3}$$

Each frame evaluated by DIC is represented as a single step in the correlation process and exported individually as a text file. This results in there being a text file for every step, each containing the evaluated data for every point on the surface of the specimen. The $x-y-z$ coordinates are indexed with respect to their grid location assigned from the DIC analysis and these grid indexes are used import the spacial coordinates from the text files into matrices named X, Y and Z in Matlab. Other values evaluated by DIC that are utilised include engineering principal strains and displacements in the x, y and z directions. The Matlab script published by Machado *et al.* [1] calculates the principal curvatures at every non-boundary point that is evaluated for a specific step. Each step file is imported and evaluated in Matlab in order to track surface deformation for the entire test duration. This results in a maximum and minimum curvature values calculated for every point and step with their respective directions, all indexed by grid position and step number. The Matlab script by Machado *et al.* [1] does not calculate principal directions or solve the eigenvalues directly and hence needed to be adapted.

4.3 Stress calculations

With principal curvatures and strains known at every point, it is possible to calculate the true stresses at each point in the directions of principal curvatures using membrane

theory. This project will focus on the apex of a bulging specimen where boundary and clamping effects will have the least effect. The apex the bulge profile is expected to be spherical for isotropic materials and ellipsoidal for anisotropic materials such as skin which tend to display a bi-symmetrical response. Under this assumption of ellipsoidal bulging, the directions of principal curvature and principal strain correlate indirectly. Spherical bulging will result in curvature at the apex that is equal in every direction likely resulting in directions that do not correlate or show a trend. The current thickness t is calculated with Equation 4.4, assuming an incompressible material response, the two principal strains at each point are used to find the resulting strain in the normal direction which is used to calculate the thickness from its original thickness pre-bulge.

$$t = \frac{t_0}{\epsilon_1 \epsilon_2} \tag{4.4}$$

The pressure history is imported and indexed with regard to the step number and time stamp on each pressure reading. The pressure is adjusted to account for the extra head of water caused from the bulge profile of the specimen. The z displacement of the apex of the bulge is used to represent the extra head of water for adjusting the pressure readings. Having compensated the pressure for the water head, and using the instantaneous thickness and instantaneous curvature in the principal directions one can then calculate the two principal true stresses using Equation 4.5.

$$\sigma_{1,2} = \frac{P}{2t\kappa_{i,ii}} \tag{4.5}$$

4.4 Graphing

Since stress and strain have been evaluated at every point, there is too much data to present for each specimen. An average can not be taken across all the points because the points closer to the clamps will be affected by the boundary effects. Figure 4.3 shows an example of the stress-stretch response of a single point at the apex of the specimen. The apex of the bulge is found by searching for the point with the greatest z displacement. Graphing nine points around the apex of the bulge shows some spread in the data as seen in Figure 4.4. By averaging the nine points at the apex of the bulge, Figure 4.5 is generated that better represents the response of a single specimen. The facet grid in the DIC software does not grantee that the true apex lies on a grid point. Having determined the grip point that appears to lie closest to the apex, taking grid points 1 facet adjacent to the point insures that data at the true apex is encapsulated. Physically this assumes that the true apex lies inside a square 3mm by 3mm for the given the camera and lens parameters.

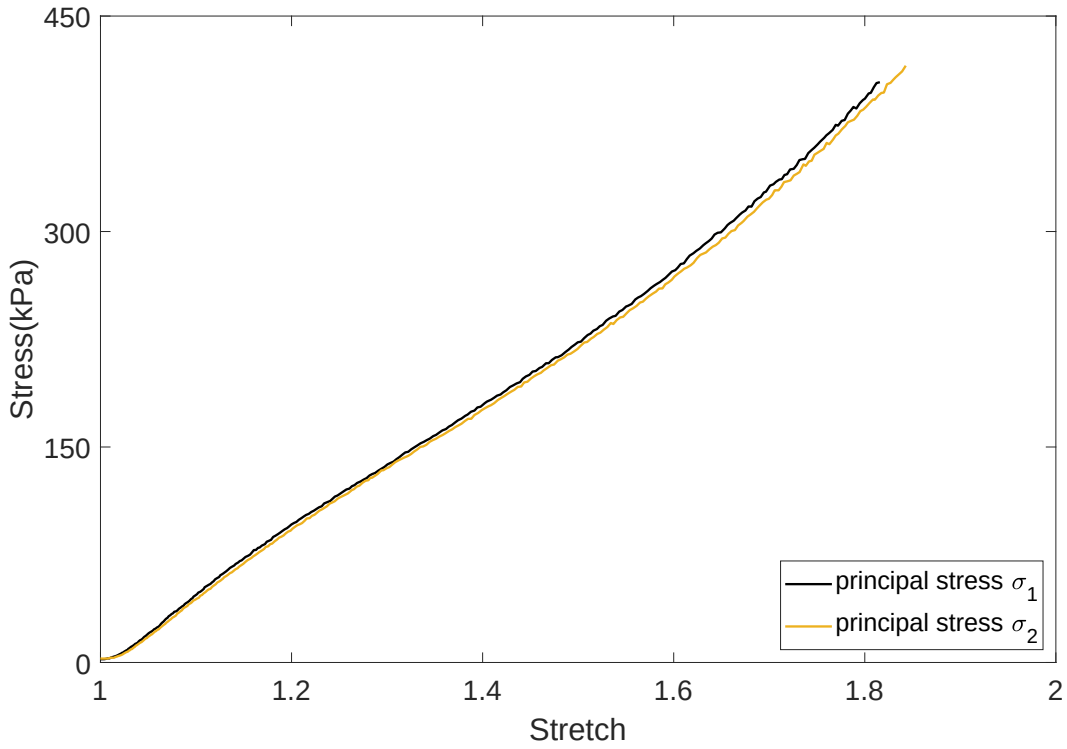

Figure 4.3 Example of a stress vs stretch graph for one point at the apex of a specimen.

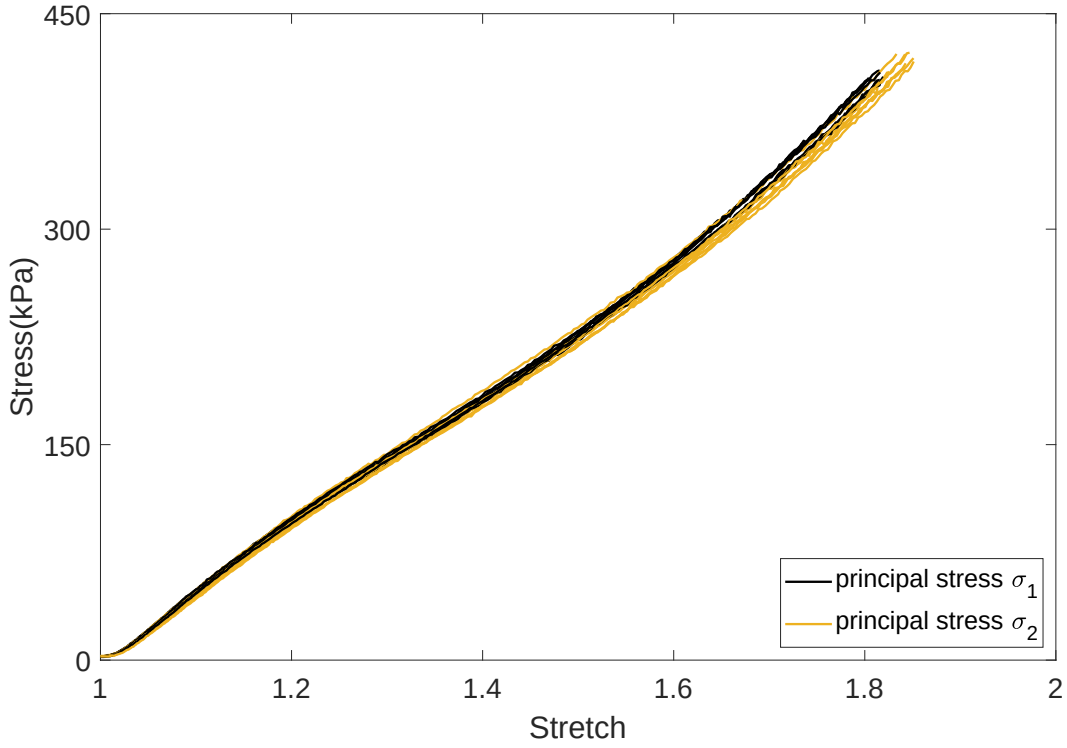

Figure 4.4 Example of a stress vs stretch graph for nine points around the apex of a specimen.

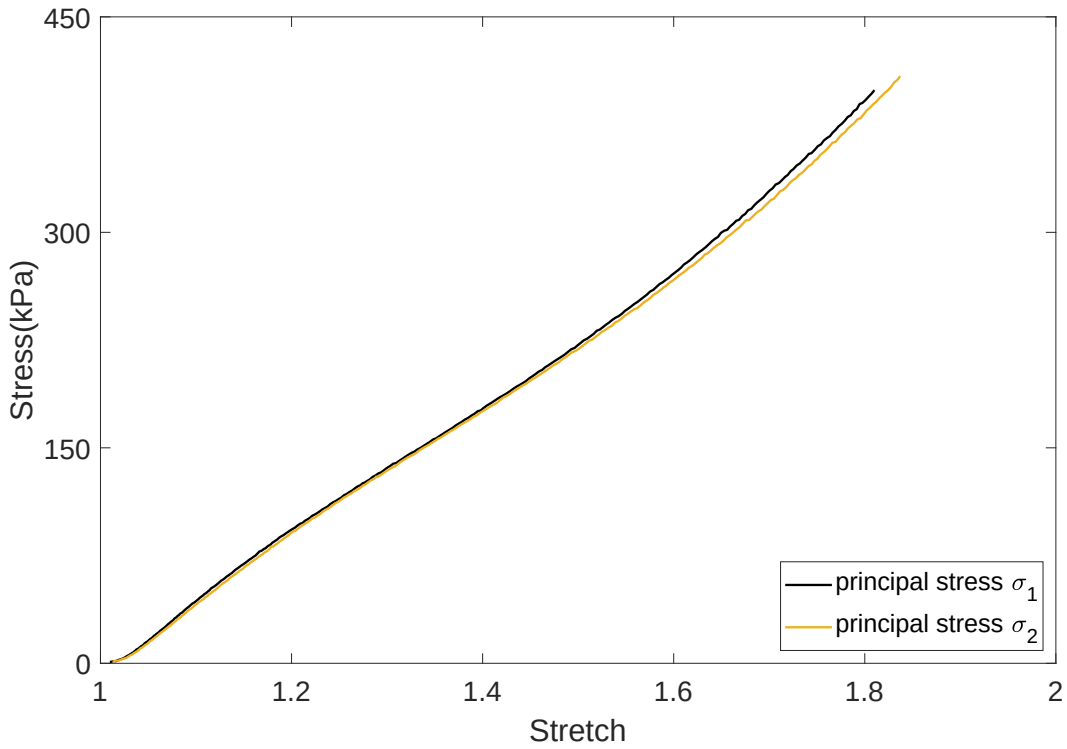

Figure 4.5 Example of a stress vs stretch graph showing the averaged response at the centre of a specimen.

4.5 Specimen preparation

The silicone used in this project consists of two parts that are mixed together in equal amounts and set to cure. Each part, A and B, are measured out by mass with a electronic scale of accuracy 0.01 g. Each part is weighed out in equal mass to within 0.02 g. More accuracy was difficult to achieve because of the nature of measuring out a highly viscous medium. The maximum recommended amount of pigment was added to each batch to achieve the best colour consistency when specimens are stretched. It was found that low amounts of pigment resulted in blotchy colouring at high strains which would negatively affect DIC. Initially small batches of specimens were cast for practising speckling methods. These specimens were mixed with silicone thinner for easier mixing and casting which meant that the specimens contained different amounts of thinner depending on how much was added in each batch. When tested, these specimens were found to vary a large amount in their mechanical response due to the silicone thinner than was used. Due to this, thinner was not used in the casting of the specimens for final testing. The material properties were clearly affected by multiple aspects of the casting process including mixing and additives, so it was decided to cast all specimens from the same batch to achieve similar properties for all specimens. The elliptical specimens in the cast were however, all rejected because the silicone did not properly fill the cavities and large air bubbles formed around the edges of the specimens. These large deformities in the elliptical specimens affected their ability

to seal and hold pressure. This meant that a new batch of elliptical specimens were cast. Since the round and uniaxial specimens were cast from the same batch and were of good quality, there was no need to recast them. Casting the elliptical specimens in a different batch is acceptable because their purpose is to demonstrate non-uniform deformation and not to compare material properties to the other specimen types.

The same silicone was also used to speckle the specimens. Other methods of speckling that were attempted include using graphite powders and spray paint. These methods were found to be undesirable because the powder shifted on the surface of the specimen and the spray paint de-laminated from the surface since its stiffness was significantly higher than the silicone. Since a better method of speckling was not found, the method used previously by Graham [2] was used. This method involved splattering a freshly mixed batch of silicone mixed with black pigment and silicone thinner on a specimen. It was found that the process was time sensitive, the specimens had to be speckled between 1 hour and 1.5 hours after casting or the black speckles would not hold their shape and spread thinly across the surface of the specimen. This method of speckling is a lengthy process but worked well for speckling few specimens. Since the DragonSkin10 silicone was observed to vary in mechanical response between different batches mixed and cast, the specimens were cast in two batches: one batch with the round bulge and uniaxial specimens and the second batch consisted of the elliptical specimens. This was to keep material properties for both tensile and bulge specimens as similar as possible. Speckling a much larger number of specimens took much longer resulting in the speckling process being rushed as well as applying the speckle outside of the ideal 30 min window. This resulted in much courser speckle patterns than what was achieved with previous smaller sample batches. The speckle patterns for the batch of elliptical specimens came out courser than the first batch of specimens which is discussed further in Chapter 6.

4.6 Testing plan

The experimental testing plan consists of two testing methods, uniaxial tension tests and bulge inflation tests. Three different types of specimens were bulge tested, a ø50 mm round specimen, 40 mm×50 mm elliptical specimen and a 30 mm×50 mm elliptical specimen. The full testing plan with testing parameters is seen in Figure 4.1. In total there are 18 round, 6 elliptical and 10 uniaxial specimens for testing.

Table 4.1 *Table showing the full testing plan for all specimens.*

Decription	**Specimen name**	**DIC frame rate (FPS)**	**Inflation rate (ml/s)**	**Motor speed (RPM)**	**Strain rate (/s)**	**Crosshead speed (mm/min)**
round	R1 - R3	0.7	0.1	4		
round	R4 - R6	30	5.9	250		
round	R7 - R9	8	1.2	50		
round	R10 - R12	13	2.4	100		
round	R13 - R15	20	3.5	150		
round	R16 - R18	25	4.7	200		
40x50mm	E1 - E3	8	1.2	50		
30x50mm	E4 - E6	8	1.2	50		
uniaxial	T1 - T5	2			1.67	50
	T6 - T10	5			5	150

Chapter 5

Results

Experimental testing included bulge testing of 18 round and 6 elliptical specimens and uniaxial tension tests on 10 dog-bone specimens. The round, elliptical and tensile specimens are denoted 'R','E' and 'T' respectively. All specimens were manufactured from the same batch of Dragon Skin 10 silicone. The results shown in this chapter include stress-stretch graphs, quiver plots showing the directions of principal curvature and cross-sections from bulge tests.

5.1 Stretch-stress graphs

The stretch-stress figures are split into three sections: uniaxial tension, round bulge and elliptical bugle tests. This data is shown in Figures 5.1 to 5.8. In all of these figures, stress refers to true stress based either on instantaneous area for uniaxial tension or instantaneous thickness and curvature for bulge.

5.1.1 Uniaxial tension

Stretch-stress graphs for all dog-bone specimens are shown in Figure 5.1 where specimens T1 to T5 were tested at a strain rate of $1.67 \times 10^{-2}/s$ ($50mm/min$) and specimens T6 to T10 were tested at $5 \times 10^{-2}/s$ ($150mm/min$). An Instron Tensile Testing machine with a 100N load cell was used to conduct the uniaxial tests based on ASTM standard D412 and DIC was used to evaluate strain for each test. The overlap and scatter in the data in Figure 5.1 makes it difficult to discern any strain rate dependency in the strain rate range tested. There is a larger spread in the stress stretch response between all the tests at higher strains. Uniaxial and bulge stress-stretch data can be compared in Figure 6.7.

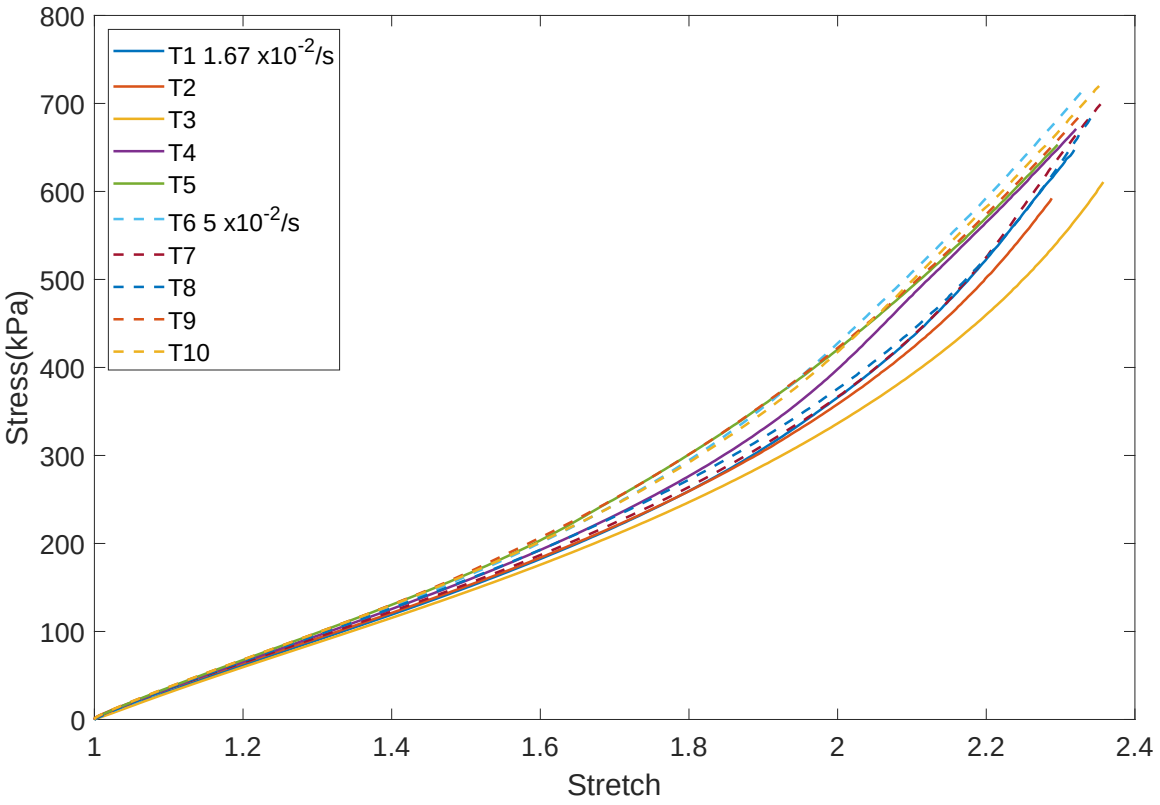

Figure 5.1 Stretch-stress graph for uniaxial tensile tests where specimens T1 to T5 and T6 to T10 were tested at strain rates 1.6×10^{-2} /s and 5×10^{-2} /s respectively.

5.1.2 Round bulge

All round bulge specimen curves (R1 to R18) are shown in Figure 5.2, where there is a small increase in the spread of data as strain increases. All round specimens display a similar response across all the bulge rates tested showing no clear strain rate effects. Specimens R1 to R3 shown in Figure 5.3 were tested at the lowest inflation rate of 0.1 ml/s and R4 to R6 shown in Figure 5.4 were tested at the highest inflation rate of 5.9 ml/s.

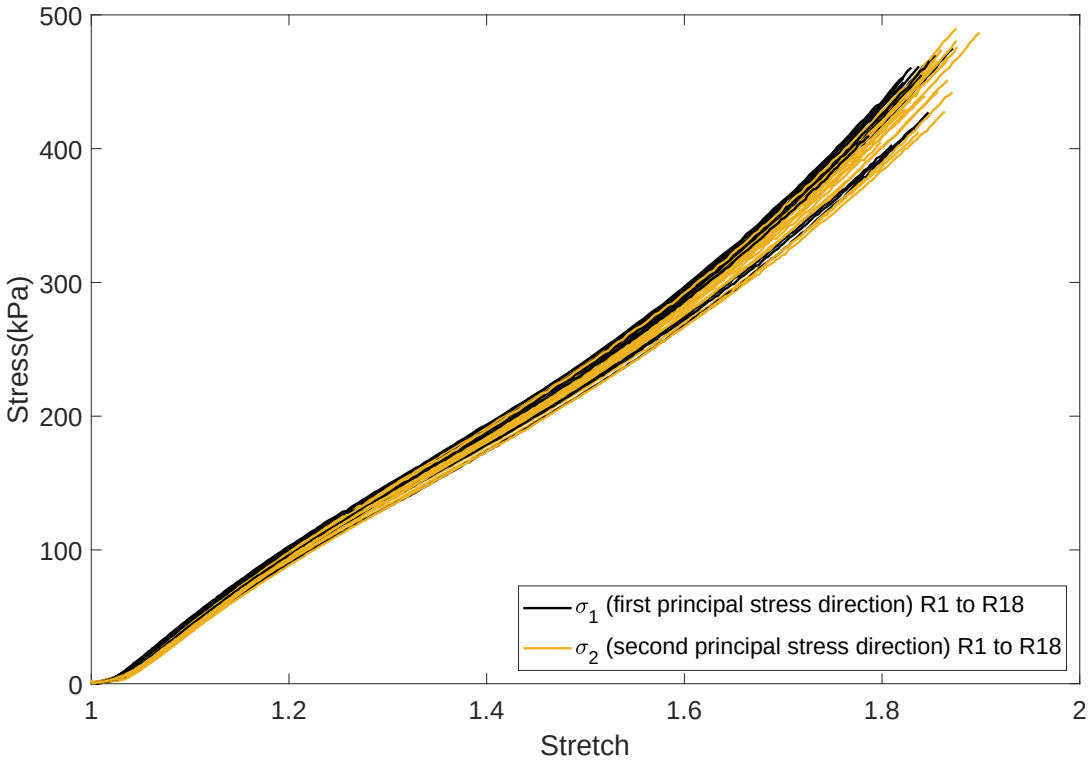

Figure 5.2 Stretch-stress curves in principal directions for all round specimens R1 to R18 inflated at rates between 0.1 ml/s and 5.9 ml/s.

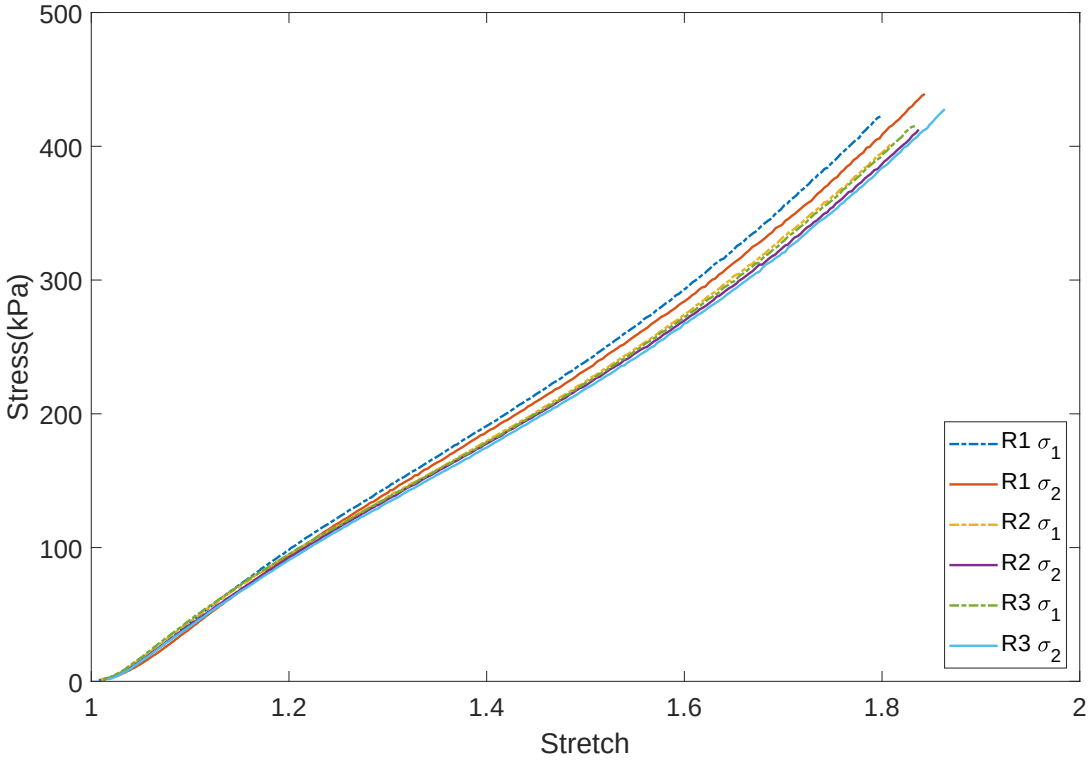

Figure 5.3 Stretch-stress curves in principal directions for specimens R1 to R3 inflated at 0.1 ml/s.

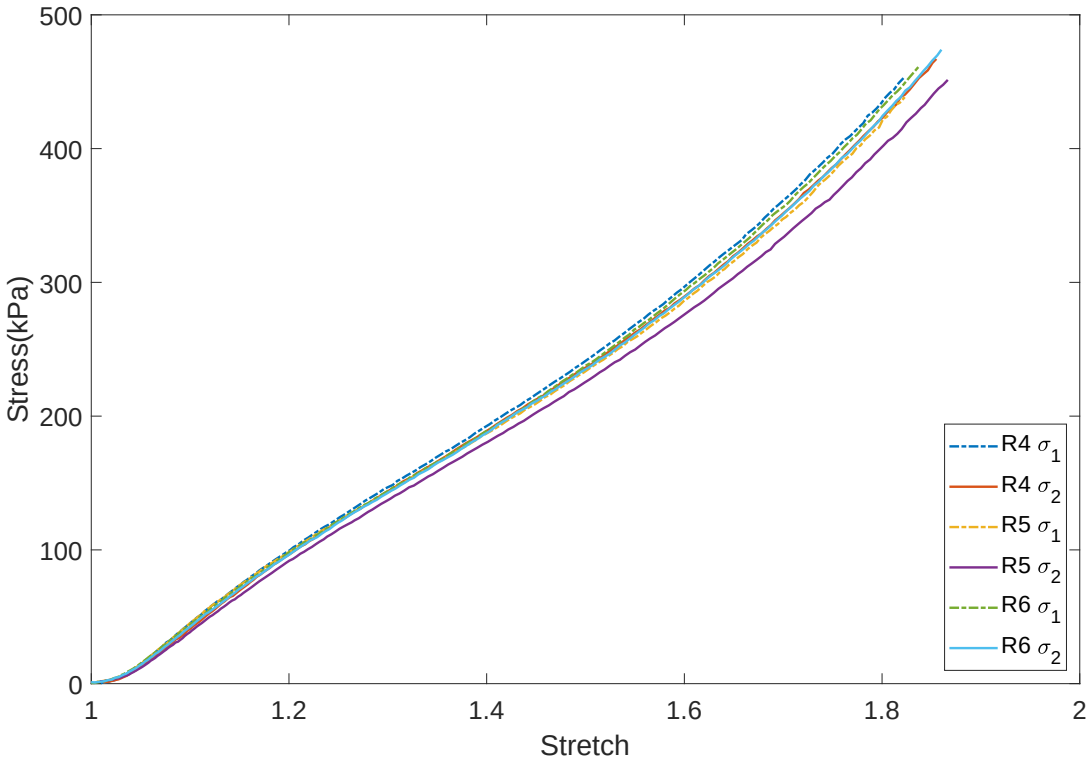

Figure 5.4 Stretch-stress curves in principal directions for specimens R4 to R6 inflated at 5. 9ml/s.

5.1.3 Elliptical bulge

All elliptical specimen curves (E1 to E6) are shown in Figure 5.5, where it is seen that there are large gaps in the data and a large spread in responses. Figure 5.6 shows the responses for the 40×50 mm specimens E1 to E3 and Figure 5.7 specimens E4 to E6. The responses from specimens E1 to E3 are similar with exception to E2 in the σ_1 direction which deviates slightly from the rest of the curves. The results for 30×50 mm specimens E4 to E6 contain larger gaps in the curves and larger spread in stress stretch response. Figure 5.8 shows the stress-stretch curves for round and elliptical specimens R1 and E1. The responses from these two specimens are comparable showing similar spread and shape.

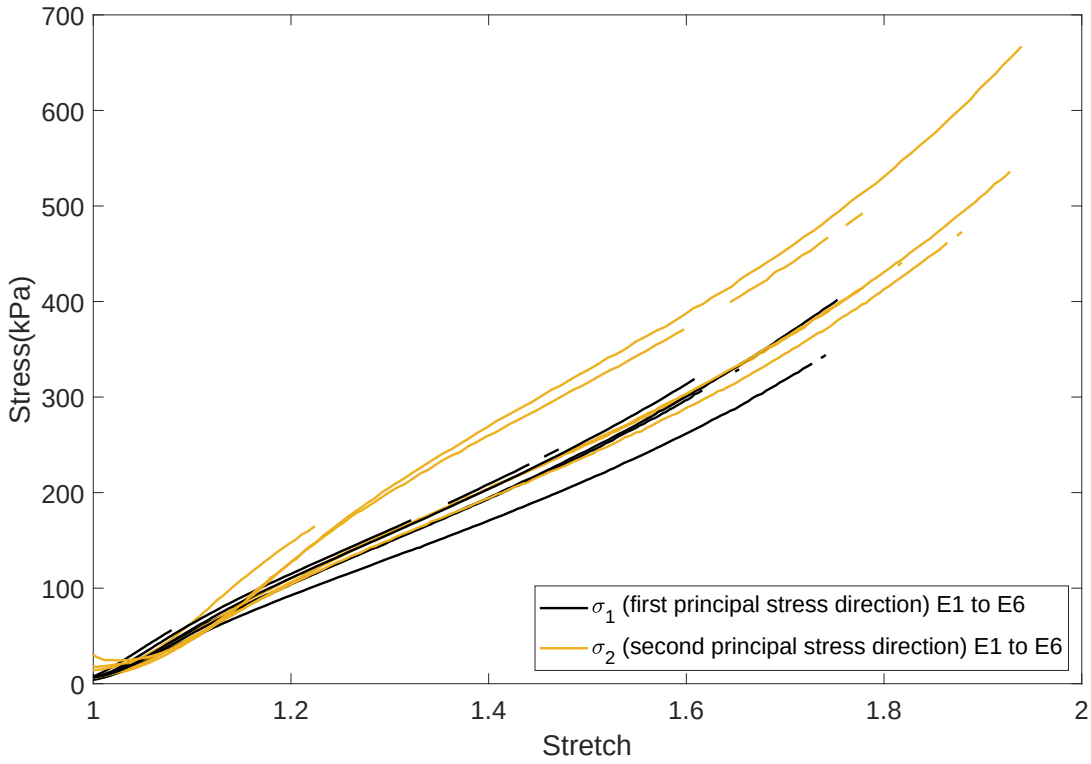

Figure 5.5 Stretch-stress curves in principal directions for all elliptical specimens E1 to E6 which were all tested at 1.18 ml/s.

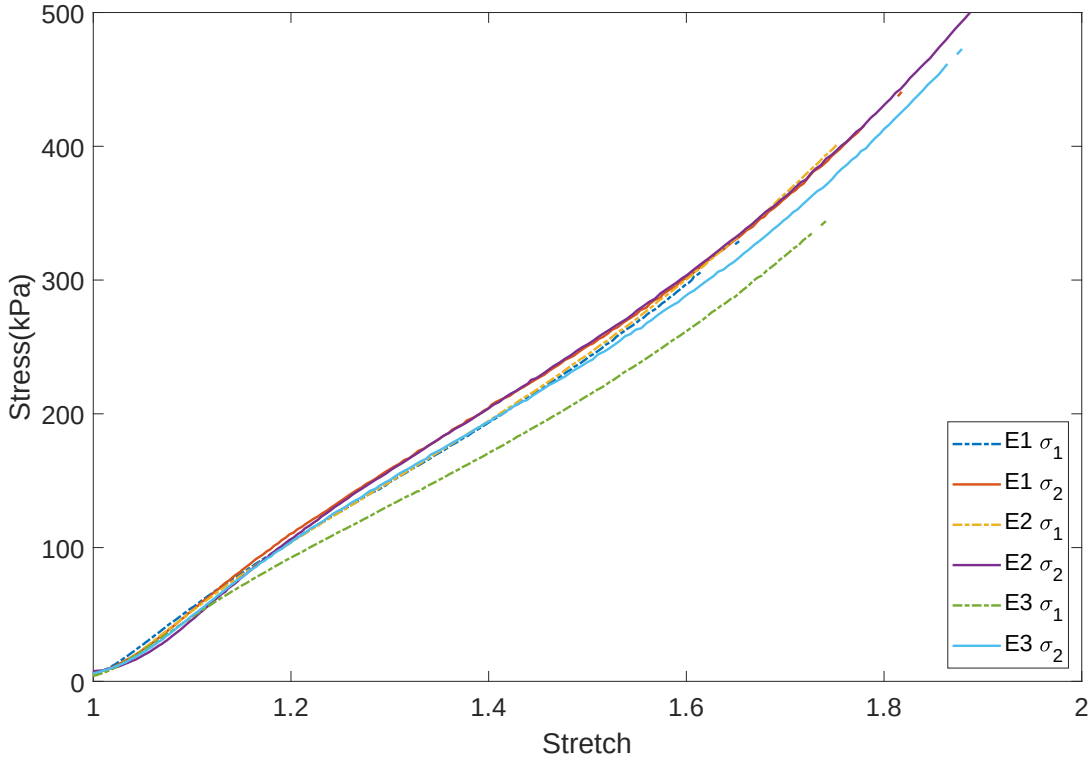

Figure 5.6 Stretch-stress curves in principal directions for 40x50 elliptical specimens E1 to E3.

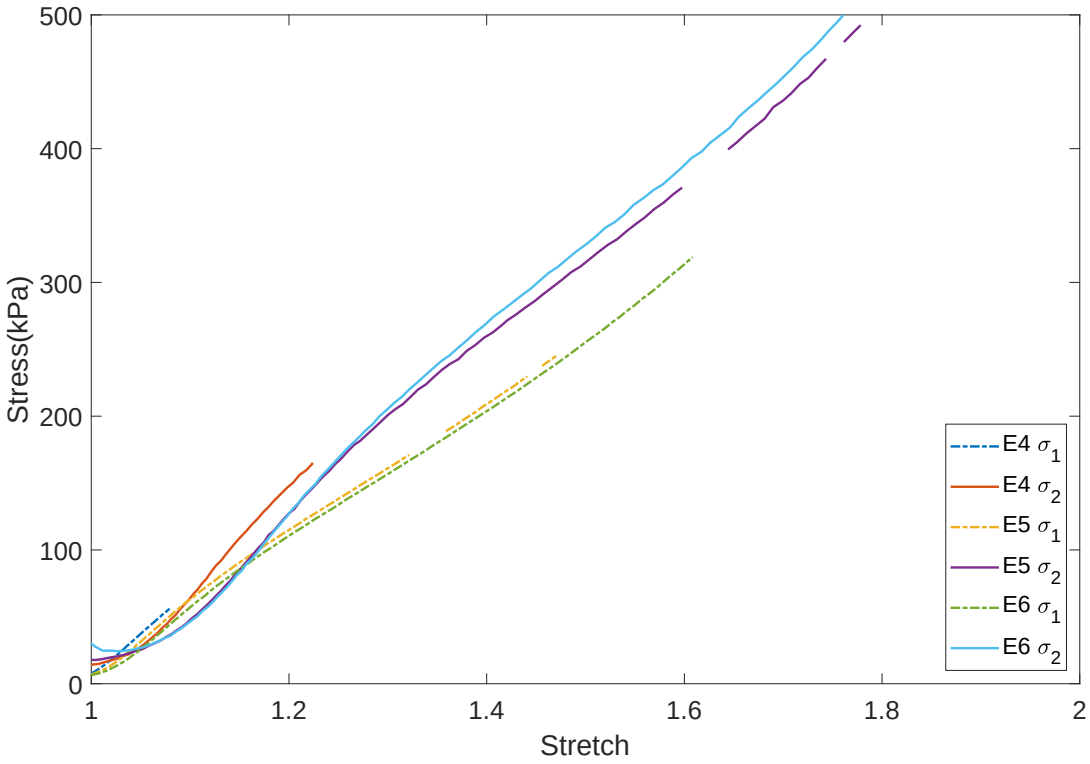

Figure 5.7 Stretch-stress curves in principal directions for 30x50 elliptical specimens E4 to E6.

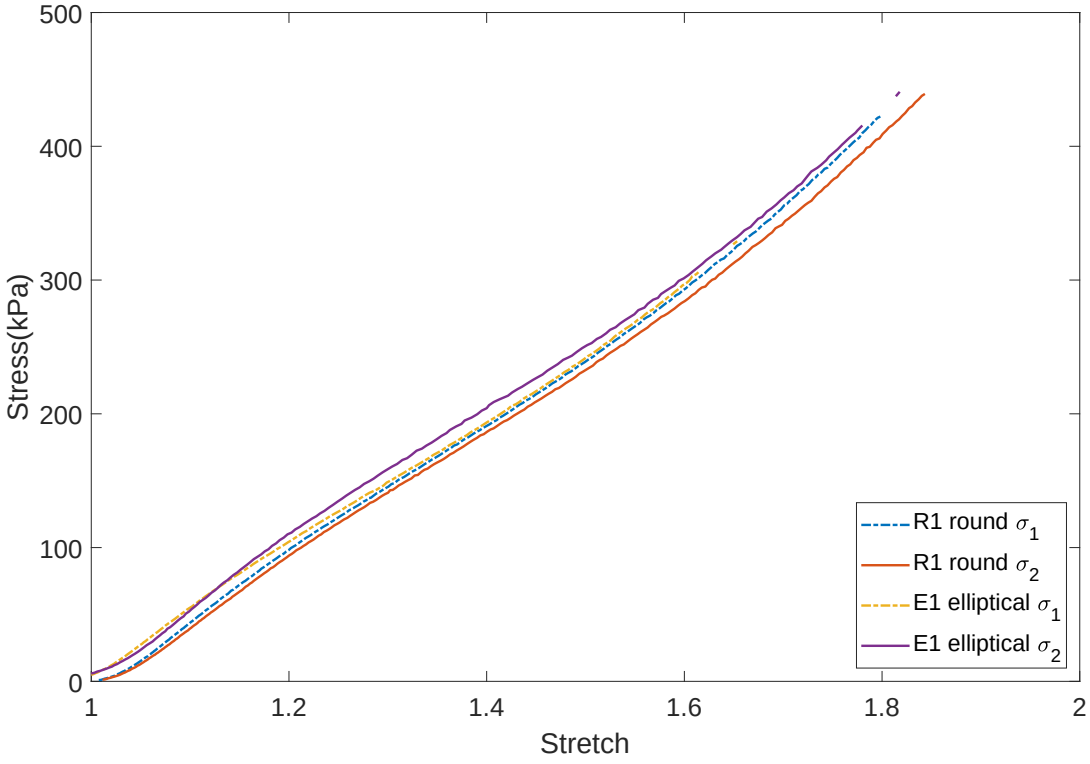

Figure 5.8 Stretch-stress curves in principal directions for round and elliptical specimens R1 and E1.

5.2 Directions of curvature

The directions of curvature are shown for each point at each step with two perpendicular arrows, one in the direction of maximum curvature and the other in direction of minimum curvature. The results for three specimens (R7, E2 and E5) are shown at three values of apex strain: 10%, 30% and 57%. Figure 5.9 (a, b, c), (d, e, f) and (g, h, i) show the curvature for specimens R7, E2 and E5 respectively. The curvature plots for the round specimen R7 show no clear trend for orientations for maximum and minimum curvature in the vicinity of the apex. This is expected due to spherical deformation. The curvature plots for both elliptical specimens show clear and consistent directions across all points for both maximum and minimum curvatures that correspond directly with the minor and major axis of the non-deformed ellipses.

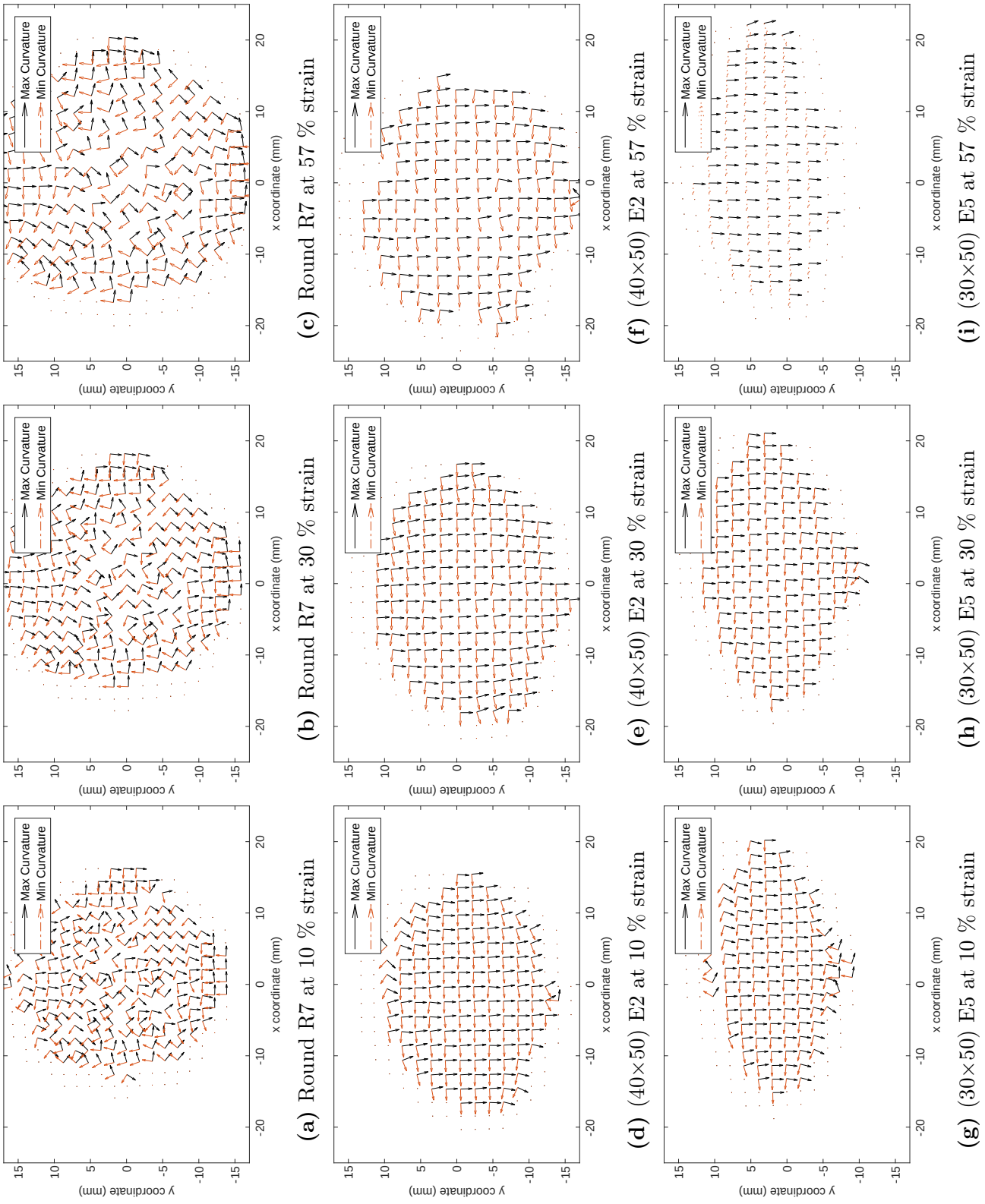

(a) Round R7 at 10 % strain **(b)** Round R7 at 30 % strain **(c)** Round R7 at 57 % strain

(d) (40×50) E2 at 10 % strain **(e)** (40×50) E2 at 30 % strain **(f)** (40×50) E2 at 57 % strain

(g) (30×50) E5 at 10 % strain **(h)** (30×50) E5 at 30 % strain **(i)** (30×50) E5 at 57 % strain

Figure 5.9 Quiver plots showing principal directions of curvature at each point of the round and elliptical specimens R7, E2 and E5 at apex strains of 10 %, 30 % and 57 %.

5.3 Bulge profiles

Bulge profiles with apex heights of 15 mm are shown for a round specimen (R5) and 40×50 mm and 30×50 mm elliptical specimens (E1 and E4) in Figures 5.10 to 5.12. Cross sections are taken in the X and Y directions for each of the three specimens to attain the bulge profiles. The X and Y directions for the round specimen show almost no difference in their profile which shows symmetrical bulge behaviour. The X and Y directions for the elliptical specimens correlate with the major and minor axis respectively for both specimens which also correlate with minimum and maximum directions of curvature.

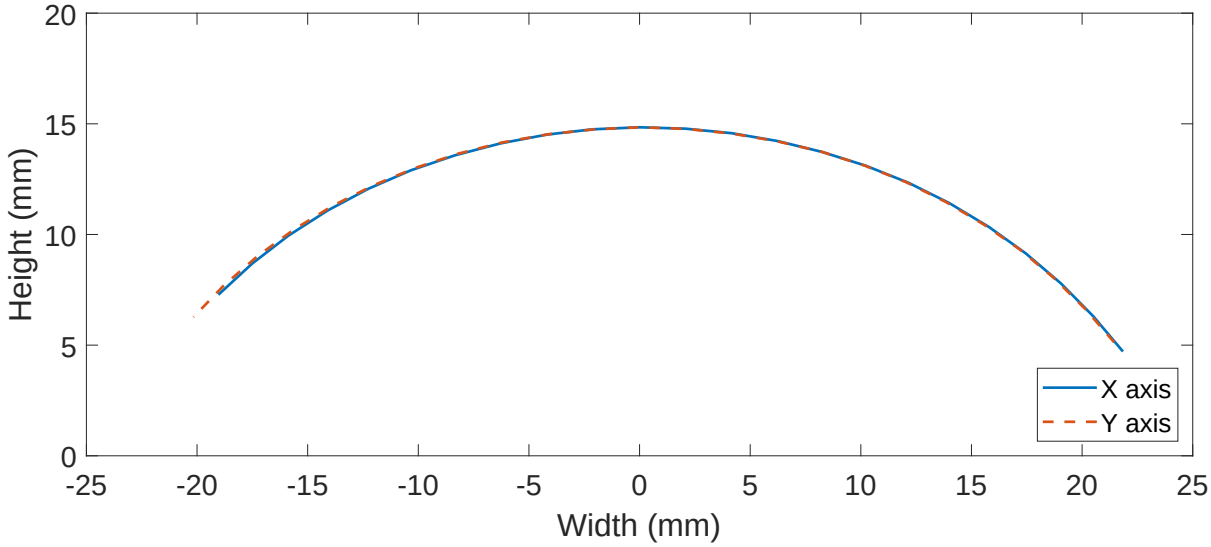

Figure 5.10 Bulge profile of specimen R5 (round specimen).

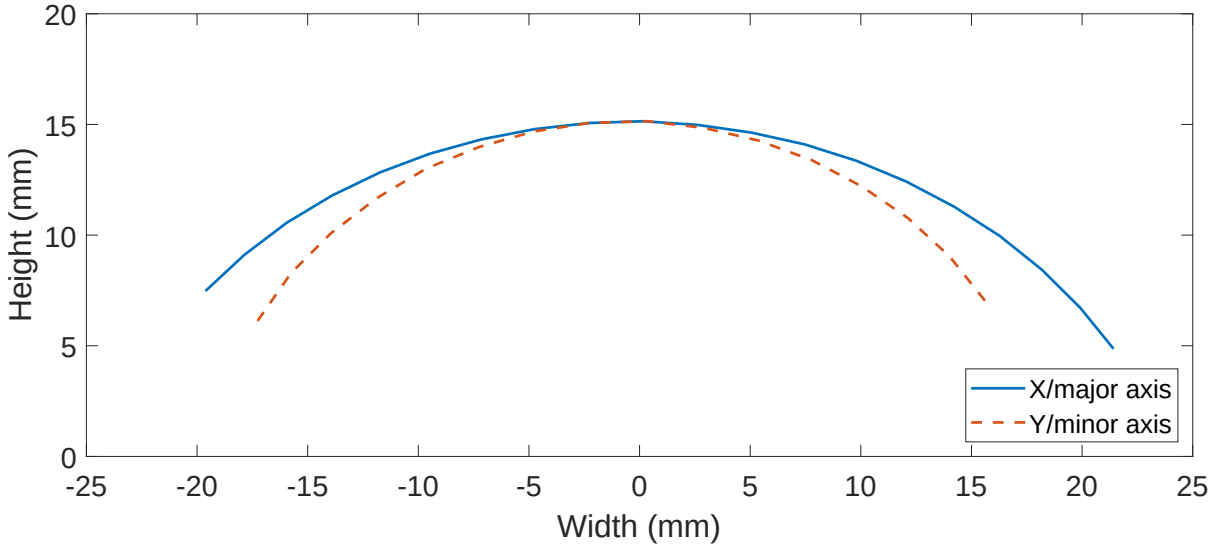

Figure 5.11 Bulge profile of specimen E1 (40x50 elliptical specimen).

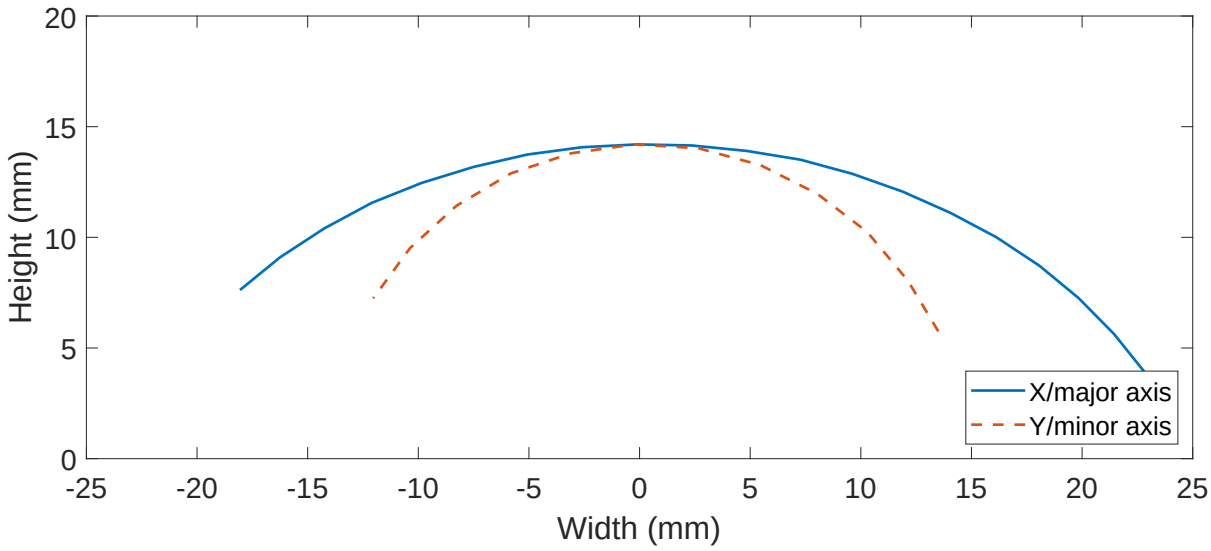

Figure 5.12 Bulge profile of specimen E4 (30x50 elliptical specimen).

5.4 Strain Rate

5.4.1 Round specimen strain rate response

The graphs showing the stretch vs strain rate responses that are seen in Figures 5.13 to 5.15 display the responses of the centres of each of the respective specimens. The strain rates in both the principal directions are shown for each specimen for comparison. Figure 5.13, which displays the data for round specimen R7, shows there is very little variation between the principal directions, as expected for a circular clamp. Both curves start with a negative gradient until a stretch of 1.08 where the strain rate increases linearly until a stretch of 1.3 after which the curve begins to level off at around 0.028 /s.

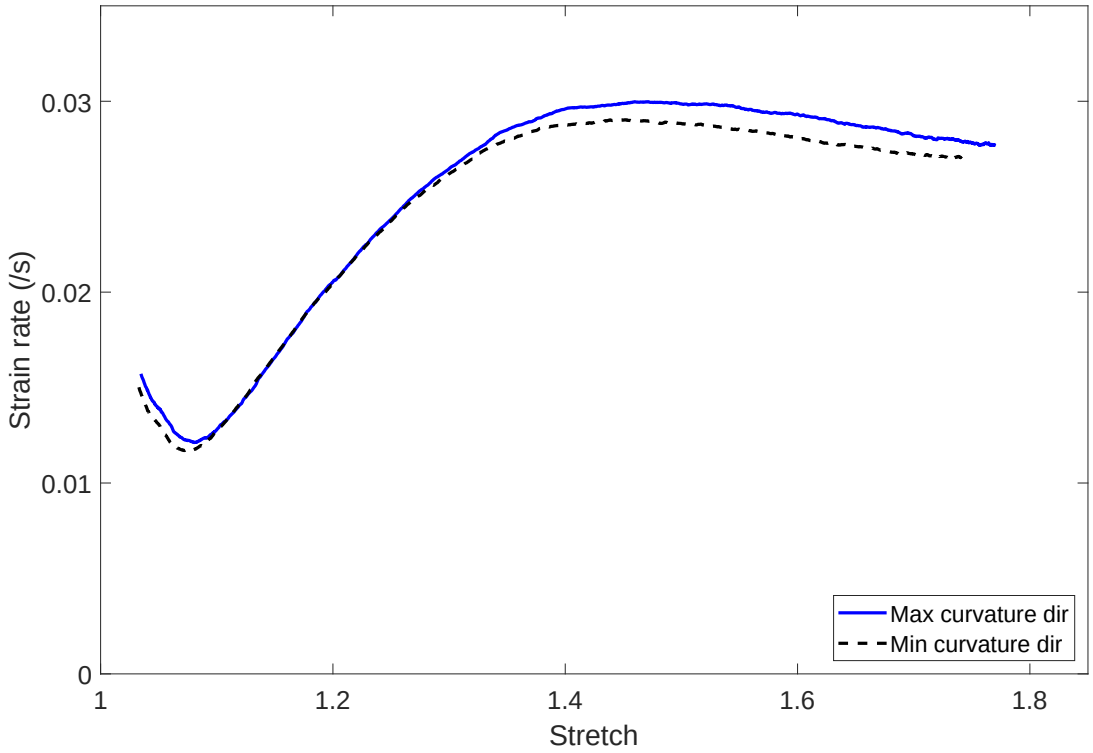

Figure 5.13 Graph showing the strain rate responses for a round specimen (R7) in both principal directions, inflated at 1.2 ml/s (50 RPM).

5.4.2 Elliptical specimen strain rate response

The elliptical specimens show different responses for the major and minor axes directions. In both elliptical specimens (E2 and E5) the minor axis direction strains at a higher rate and also undergoes more strain than the major axis direction. The elliptical and round specimens show a similar shaped response. However, the elliptical specimens show higher strain rates in the minor axis direction and the major axis direction strains less than the minor axis direction. There is a larger difference in response between the major and minor axes directions for the 30×50 (E5) specimen than the 40×50 (E2) specimen. The 30×50 (E5) specimen also strains at a higher rate in both directions than the 40×50 (E2) specimen.

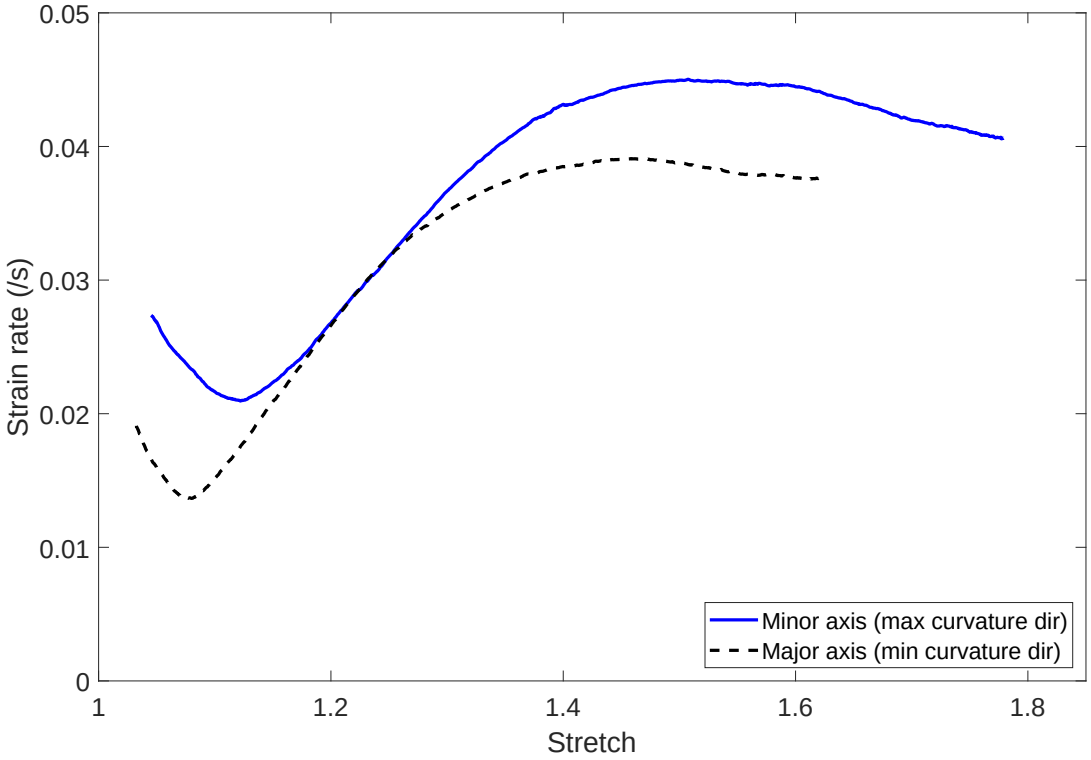

Figure 5.14 Graph showing the strain rate response for an elliptical specimen (E2) in both principal directions, inflated at 1.2 ml/s (50 RPM).

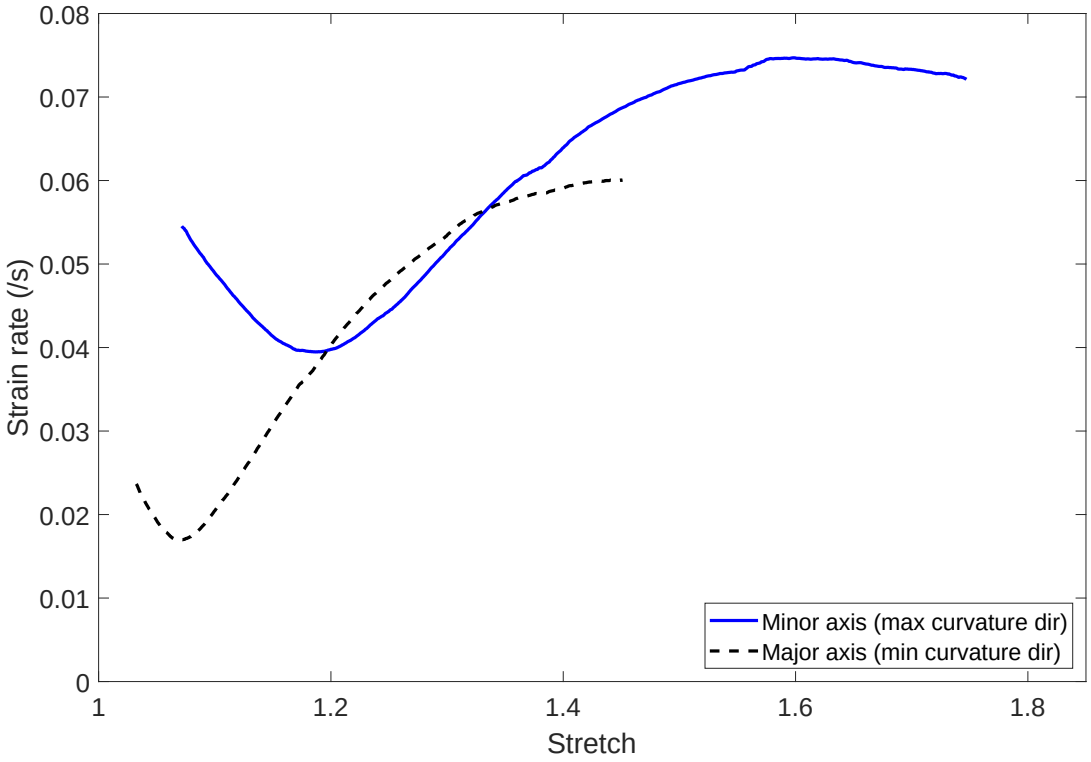

Figure 5.15 Graph showing the strain rate response for an elliptical specimen (E5) in both principal directions, inflated at 1.2 ml/s (50 RPM).

Chapter 6

Discussion

6.1 Material behaviour

Even within the same batch of silicone, the material properties for the uniaxial tests are seen to vary as seen in Figure 5.1, where the graphs for all ten uniaxial specimens are shown. The stretch-stress responses seems to vary the most at approximately a stretch of 2.1 to 2.2 after which the responses appear to converge. The same response is not evident in the bulge data since the stretch values only go up to a stretch of 1.8. Investigating this response further, Figure 6.1 shows the spread in stress values across the different specimen curves at four different stretch values. The mean stress of each curve is located on the 0 kPa line with the upper and lower bound stresses represented with error bars above and below the 0 kPa line. These mean, upper and lower stresses are plotted for both the uniaxial and bulge data for comparison. The spread in data between the uniaxial and bulge data at the various stretch values shows very similar responses. There is clearly more spread in the bulge data than the uniaxial data when comparing the magnitudes. Figure 6.2 shows the normalised spread, where error is expressed as a percentage relative to the mean stress at the corresponding stretch value, this allows easier comparisons of spread as the magnitude of the stress increases as in Equation 6.1. In Figure 6.2 it is seen that the bulge curves show their largest error at the lowest stretch of 1.2 with an error of 10 % and the error at the other stretch values remain fairly constant at around 8 %. The error for the uniaxial curves tends to increase with an increase in stretch from 7.5 % to 15 % error at the highest stretch of 2.2.

$$error(\%) = \frac{\sigma_{max/min}}{\sigma_{mean}} \tag{6.1}$$

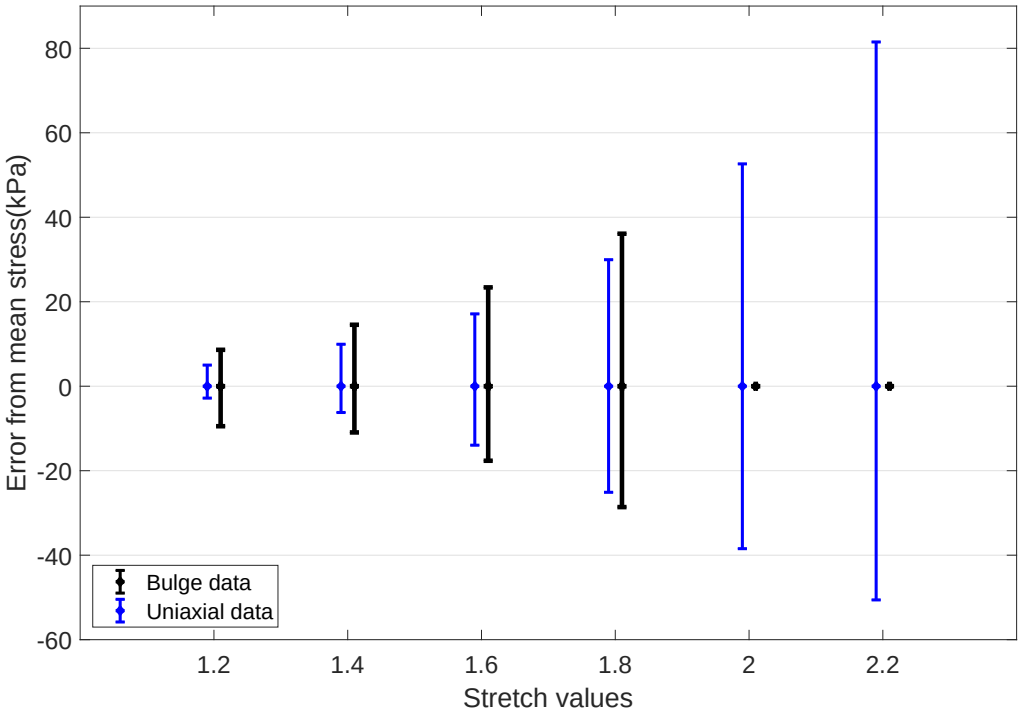

Figure 6.1 Plot showing the spread in stress curves at various stretch values comparing both uniaxial and bulge data.

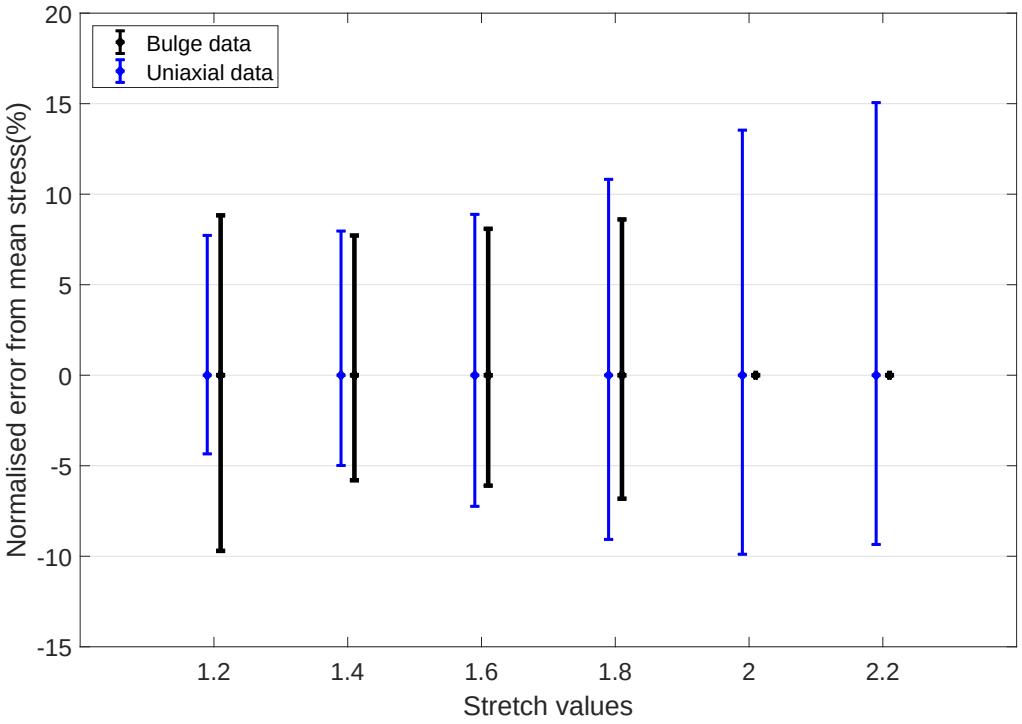

Figure 6.2 Plot showing the normalised spread of the stress curves relative to the mean stresses at various stretch values comparing both uniaxial and bulge data where the error bars indicate upper and lower bounds for variation.

6.2 Specimens and Speckle Patterns

Figure 6.3 shows the specimens in their undeformed state, with (a) to (r) being round specimens and (s) to (x) corresponding to elliptical specimens. It is evident that the speckle patterns for the elliptical specimens are qualitatively different from the round specimens, which has affected the DIC results. The speckle patterns for the elliptical specimens appear much darker with large connected black spots rather than the smaller black dots seen for the round specimens. It is strongly believed that this coarser speckle pattern had the largest impact on the lower quality of the elliptical stretch-stress data presented in this project. The large connected black spots on the elliptical specimens reduce the resolution of the DIC analysis because there are fewer unique markers on the surface to track the same amount of grid points as the round specimens. This necessitated using a larger grid spacing for DIC analysis of the elliptical specimens, as shown in Table 6.1, or the correlation would fail. The coarser speckle patterns that result in difficulty calculating and tracking strain in DIC, lead to gaps in the strain fields at larger strains. This is amplified for the elliptical specimens where the minor axes have reduced area to capture sufficient grid points across the surface.

Table 6.1 *Table showing the grid and facet DIC settings for the different specimen types.*

Specimen type	**Grid spacing (mm x mm)**	**Facet size (mm x mm)**
Round	1.7	2.5
Uniaxial	1.7	2.6
Elliptical	1.9	3.1

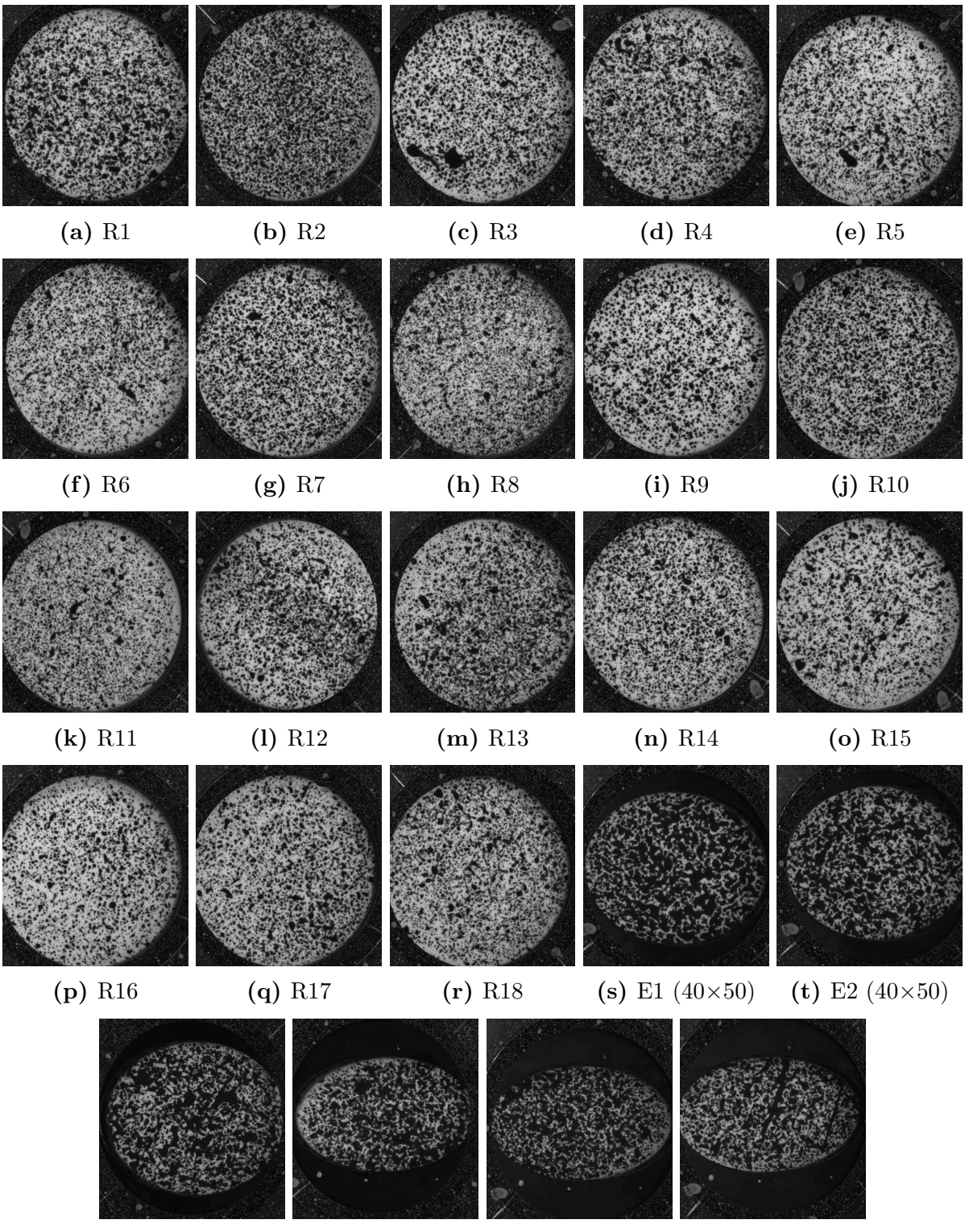

(a) R1 **(b)** R2 **(c)** R3 **(d)** R4 **(e)** R5

(f) R6 **(g)** R7 **(h)** R8 **(i)** R9 **(j)** R10

(k) R11 **(l)** R12 **(m)** R13 **(n)** R14 **(o)** R15

(p) R16 **(q)** R17 **(r)** R18 **(s)** E1 (40×50) **(t)** E2 (40×50)

(u) E3 (40×50) **(v)** E4 (30×50) **(w)** E5 (30×50) **(x)** E6 (30×50)

Figure 6.3 Images showing the speckle patterns of specimens R1 to R18 and E1 to E6.

6.3 Directions of curvature

6.3.1 Elliptical specimens

The directions of curvature results that were presented in Figure 5.9, show that the curvature code and calculations worked very well in showing the principal curvature directions that correlated with the major and minor axes of the elliptical specimens. The purpose of the elliptical specimens is to force more strain in one axis than the other when bulged. This type of response where there is more strain in one specific direction is representative of collagenous tissue such as skin which will have a fibre direction with a stiffer response. The response of skin tissue to bulge testing presented in Tonge *et al.* [4] shows that the stiffer fibre direction shows higher curvature than the direction perpendicular to the fibres as seen in Figure 6.4. This demonstrates how the minor axis of the elliptical specimens in this project can represent the fibre direction of a skin specimen. The methods used in this project evidently have a good ability to clearly show the directional trends of a bulging specimen that strains more in one axis than the other.

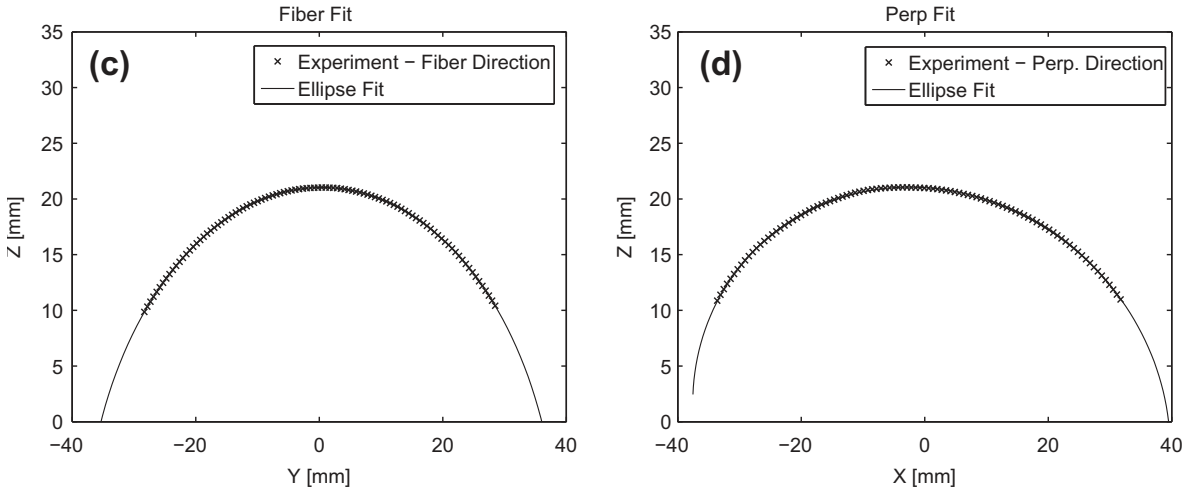

Figure 6.4 Results from Tonge *et al.* [4] where 2-D ellipses are fitted to bulge profiles of human skin specimens in the fibre and perpendicular directions.

6.3.2 Round specimens

Since every point of a sphere has equal curvature in every direction, it should be expected that with the small variations from DIC, the curvature directions for the round specimens will display a randomised type of response. This randomised response is expected to be the most prevalent at the apex of the specimens where clamping will have the smallest effect. This expected response is consistent with the results shown in Figure 5.9 (a) to

(c) where there is clearly no trend or pattern in the curvature arrows near the centre of the specimen. This suggests that any skin specimens that show a similar response might be bulging in a spherical manor with no clear fibre direction. If cameras with higher resolutions are used and a much finer speckle pattern is achieved then it would be expected that the method of curvature evaluation in this project would be capable of showing local fibre directions rather than just on a larger scale relative to the specimen size.

6.4 Testing Apparatus

6.4.1 Mechanical apparatus

The bulge testing device worked well at all inflation rates tested from 0.1 ml/s (4 RPM) to 5.9 ml/s (250 RPM). There is no visible difference in the data presented in Figures 5.3 and 5.4 which show the lowest and highest inflation rates tested respectively.

The only filtering/averaging that is applied to the stretch-stress data in this project is when the nine points around the apex of each specimen are averaged to form the two curves that represent each specimen in both principal directions. The data discussed in Section 6.1 shows that the spread in the bulge results is very similar to the Instron results, which suggests the data produced from the bulge tester in this project is of good quality.

6.4.2 Imaging and DIC

The DIC process in this project is believed to have the largest influence on the error and spread in data seen in the results of this project. This includes the lenses and lighting difficulties experienced when setting up the cameras for DIC and the difficulty in achieving a fine speckle pattern for the silicone specimens. It is expected that in future testing of biological tissues with this device, speckling of biological tissue and lighting will provide a different set of challenges to those seen in this project. D. Pillay executed a final year UG project, concurrent with the latter stages of this project, that investigated the different methods of speckling biological tissue (sheep intestine). Pillay's work revealed various challenges in speckling moist tissue, that can affect the quality of the DIC measurements.

6.5 Strain Rate

Specimens R7, E2 and E5 were all tested at the same inflation rate of 1.2 ml/s. However, the strain rate responses of all three specimens differ. The curves for all the directions and specimens follow the same type shape but all vary in magnitude and gradient. The two curvature directions of the round specimen strain at the same rate which is expected since

the round specimen should bulge symmetrically. The elliptical specimens, however show different strain rate responses for each principal direction. This is because of the geometric relationships between the major and minor axes of an ellipse that is bulging into an ellipsoid. As can be seen in Figure 6.5, the minor axis direction of the elliptical specimens strain at a greater rate and to a greater magnitude than the major axis direction. This is expected since the minor axis would need to strain more than the major axis to achieve the same apex height of the bulge. The increased strain rates for the elliptical specimens compared to the round specimen is seen because of the volumetric differences between the bulge shapes. An ellipsoid with an equal major axis dimension to a sphere, will have less volume than a sphere with a decrease in the minor axis dimension. With an inflation rate that is equal, the ellipsoid with the smaller minor axis dimensions will inflate faster than a sphere would resulting in an increased strain rate as seen by the 30×50 specimen straining at the highest rate and the round specimen at the lowest rate. From this it is seen that by restricting a specimen to bulge in an elliptical manner the strain rate in the minor axis is forced to be at a higher rate than the major axis. This also suggests from Section 6.3, that a skin specimen with a stiffer fibre direction will strain at a higher rate in that fibre direction than the perpendicular direction even for a round specimen.

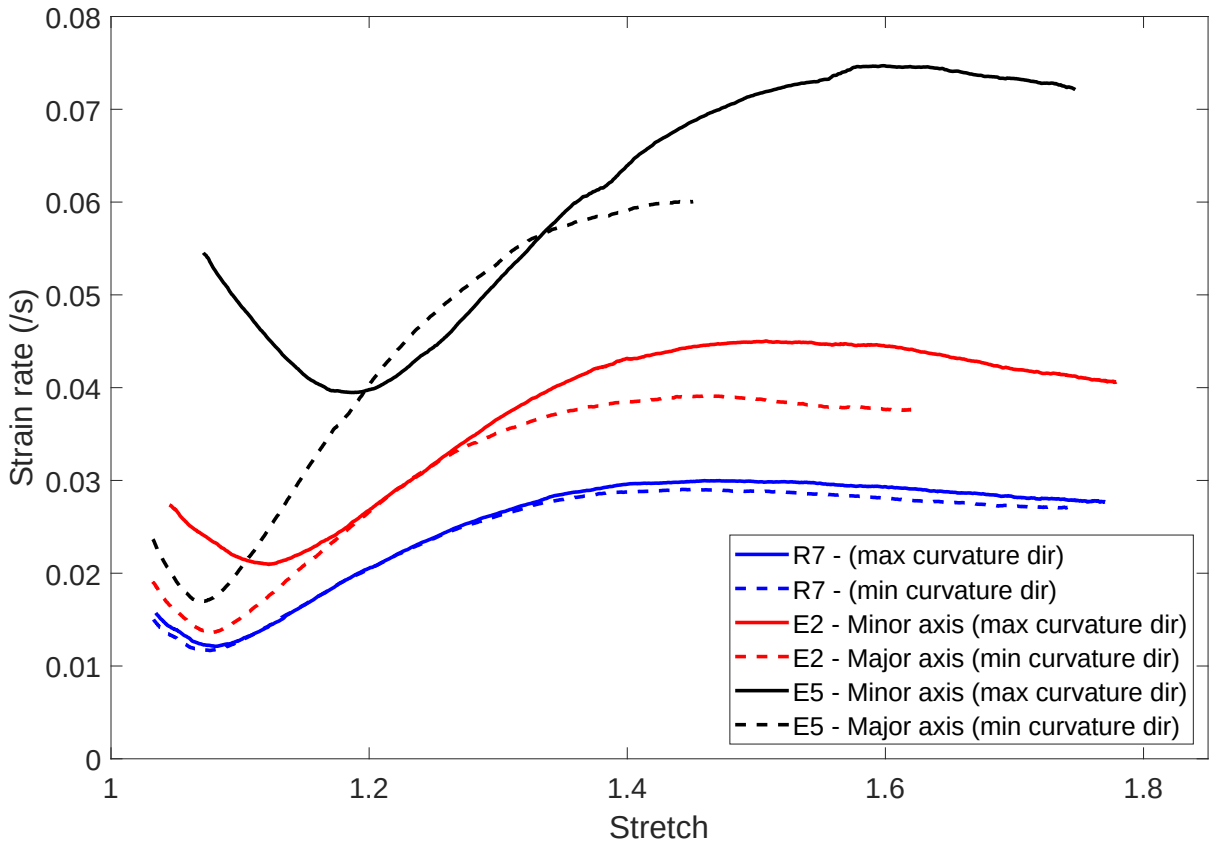

Figure 6.5 Comparing strain rates for specimens R7, E2 and E5 in both principal directions, all inflated at 1.2 ml/s (50 RPM).

The similar shapes seen in the strain rate responses suggests that a more constant strain rate can be achieved by adapting the inflation rate to following the inverse shape of the strain rate response. A rough inflation rate profile would begin by ramping up in speed followed by ramping down in speed and then levelling off to a constant inflation rate. This can be implemented in the software without any changes to hardware.

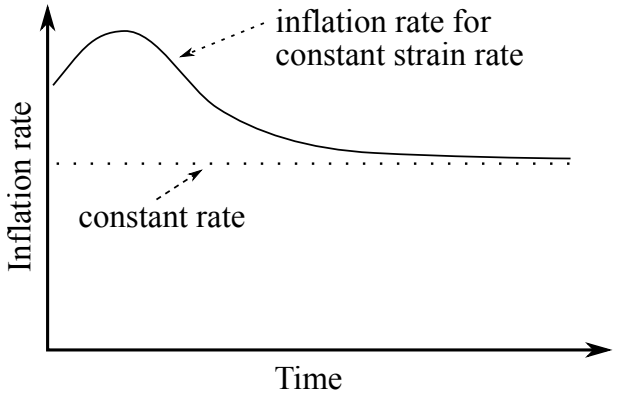

Figure 6.6 Estimate of inflation rate profile for near constant strain rate.

6.6 Ogden material models

Third order Ogden material models are fit to both the bulge and the uniaxial tension data sets. The material constants for both fits are presented in Table 6.2. The parameters were optimised by using the 'solver' add-in in Microsoft Excel following the method by Kemmer *et al.* [36] to minimise the sum of the error squared. The Ogden curve for the bulge curve fits well for the majority of the response but varies slightly for the first 10 % as seen in Figure 6.7. The variation between the Ogden model and the average uniaxial tensile test tensile data is substantial smaller than the variation in either the experimental upper or lower bounds in comparison to the average stress data. The data in Figure 6.8 illustrates how the the material parameters for the uniaxial and biaxial states are able to model each other. By using the parameters obtained from the biaxial fit to calculate the uniaxial response, it is seen that the response stiffness is underestimated compared to the experimental uniaxial data. The bulge response model using the parameters from the uniaxial fit shows a slightly stiffer response than the experimental bulge data. The solver found consistent parameters for the uniaxial fit but was much more sensitive when fitting to the bulge data. Parameters for the bulge data varied a large amount for different start point inputs into the solver. The errors for the different sets of parameters were very similar but the predictions for the uniaxial response using the different sets of parameters for the bulge data produced different curves. This suggests that the uniaxial data was able to reasonably predict the biaxial response but the bulge data was unreliable in predicting the uniaxial response, which contradicts the findings of Seibert *et al.* [23]. It is clear that fitting the material model parameters for non-linear models is a non-trivial exercise.

As the aim of this project was not to obtain the material parameters for the silicone elastomer to high precision, this was not pursued further. Follow-up projects which seek to characterise skin or membrane tissue will need to devote more attention to the parameter fitting methodology.

Table 6.2 *Material constants for the three term Ogden material models of bulge and tensile experiments.*

Bulge		**Uniaxial tension**	
$\alpha_1 : 0.136$	$\mu_1 : 124 \times 10^4 N/m^2$	$\alpha_1 : 0.344$	$\mu_1 : 626 \times 10^3 N/m^2$
$\alpha_2 : 5.61$	$\mu_2 : 200 \times 10^1 N/m^2$	$\alpha_2 : 6.92$	$\mu_2 : 969 N/m^2$
$\alpha_3 : -3.55$	$\mu_3 : -134 \times 10^1 N/m^2$	$\alpha_3 : 1.02$	$\mu_3 : 112 \times 10^1 N/m^2$

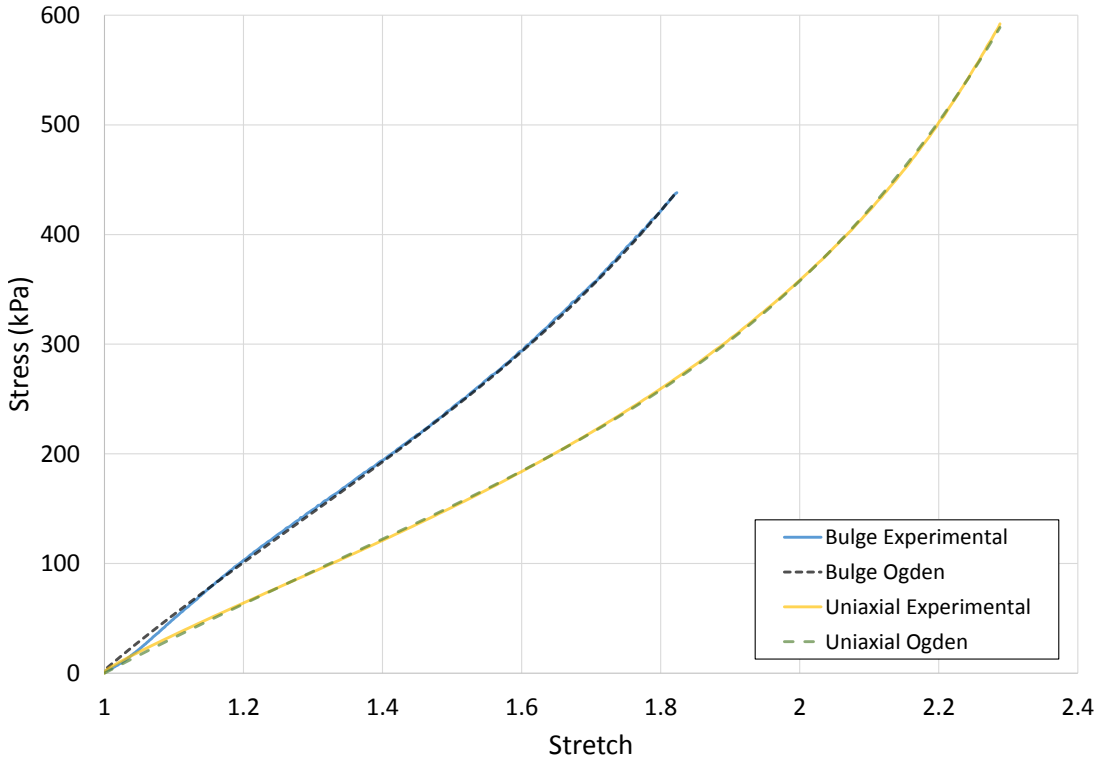

Figure 6.7 Third order Ogden material models for uniaxial and bulge experimental data.

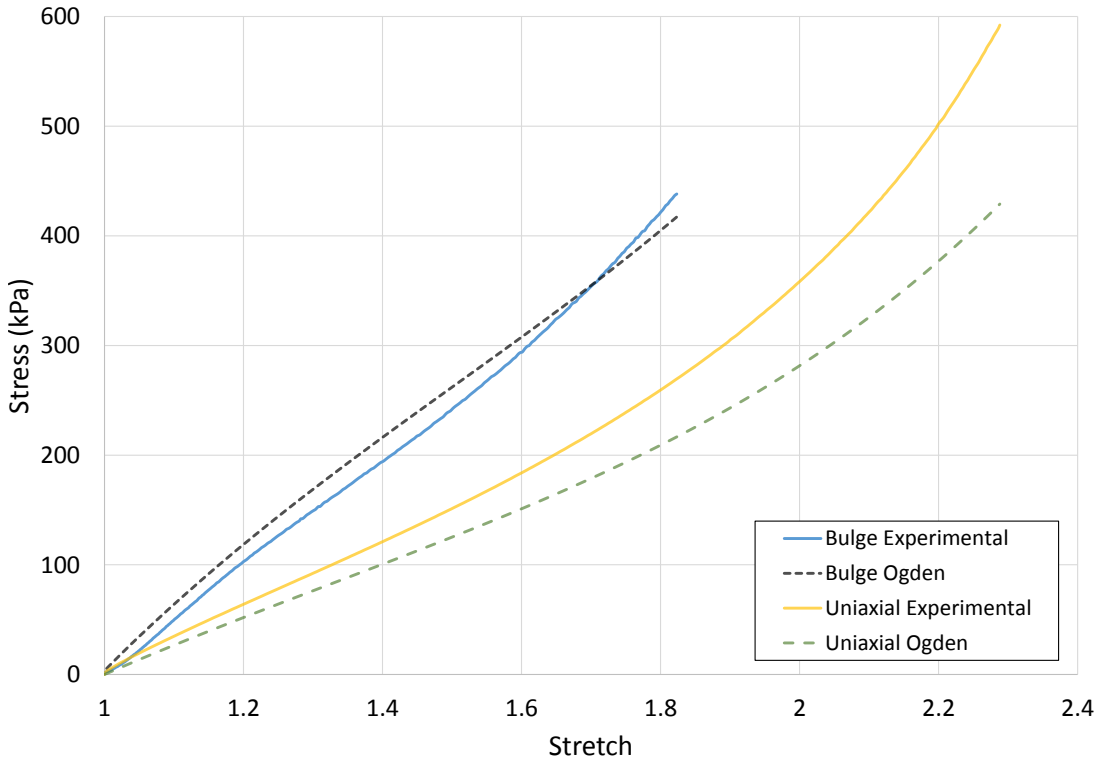

Figure 6.8 Using the uniaxial Ogden parameters to model the biaxial response and vice versa.

Chapter 7

Conclusions and Recommendations

The aim of this project was to build a bulge testing device for testing skin and membrane tissue within the parameters discussed in Chapter 3. An extensive literature review was completed on the properties of skin tissue and experimental methods of testing. Design requirements were compiled after which the bulge tester and syringe pump were designed and manufactured followed by the design and implementation of the electronics and control system. Silicone specimens were cast and speckled for testing and final testing was completed on 18 round, 6 elliptical and 10 uniaxial specimens. All bulge tests were performed at constant inflation rates between 0.01ml/s and 5.9 ml/s and uniaxial tests were completed at strain rates of 1.67×10^{-2} /s (50 mm/min) and 5×10^{-2} /s (150 mm/min). DIC was used to attain surface deformations fields of all tests and Matlab was used to analyse the DIC data and calculate curvature results and stretch-stress.

7.1 Experimental Apparatus

The experimental rig was designed for testing skin and other biological tissue. However, validation tests were done with silicone. All the design requirements discussed in Chapter 3 were adhered to in the final design of the bulge tester. The electronics and control system was designed and implemented onto the bulge tester, after which preliminary testing was completed. Experimental testing of Dragonskin10 silicone was conducted on both the bulge tester and an Instron uniaxial testing machine. The bulge tester performance was compared to the Instron by examining the stretch-stress data for each device. The data from the two devices were found to closely match in spread and error which gave confidence that the bulge tester system was reliable. The normalised error for the bulge tester was found to remain fairly constant at 8 % to 10 % and the error for the Instron was found to increase with stretch from 7.5 % to 15 %. The results for the lowest and highest inflation rates were shown to compare favourably, showing no clear strain rate effects. The range of speed for smooth running of the motor is 0.8 RPM to 250 RPM which results in an

inflation rate of 0.02 ml/s to 5.9 ml/s on the current device set-up. The bulge tester worked well for all the inflation rates tested and produced good data within its specified testing range.

7.2 Experimental Testing and Results

Dragonskin10 silicone was used for experimental testing in this project as a substitute for the intended biological materials such as skin. Dragonskin10 is commercially used as a human skin substitute in orthotics and prosthetics. The casting and speckling of the silicone was found to be difficult and inconsistent which resulted in different speckle patterns for the two different batches that were used in testing. The first batch was intended to contain all the final specimens. However, the elliptical specimens from this batch contained defects, hence they could not be tested. A second batch of elliptical specimens were cast and the speckle patterns applied to this batch resulted in coarser DIC analyses than the round specimens with the better speckle patterns. This lead to inferior data for the elliptical specimens.

The results from experimental testing comprised of stretch-stress curves, curvature plots, bulge profiles and strain rate curves. The stretch-stress curves of the round specimens showed low spread and good consistency across all inflation rates tested. However, the elliptical specimens showed larger spread in data with large gaps due to inferior speckle patterns. Third order Ogden models were fitted to both uniaxial and bulge data and found to correlate well. Using the uniaxial Ogden parameters to predict the bulge response was found to be a closer prediction than using the bulge parameters to predict the uniaxial response. More detailed work is required to investigate this finding fully but further investigation falls outside the scope of this project. The strain rate curves showed clear differences between the major and minor axes of the elliptical specimens. This provided insight into how geometric relationships of round and elliptical specimens affect strain and strain rates as well as how to induce different strain rate behaviour. The curvature results clearly demonstrated the ability to determine principal curvature directions for the elliptical bulge profiles that are representative of skin and other collagenous tissue behaviour. The method used in this project is therefore capable of clearly extracting a stiffer axis or fibre direction from bulged specimens which is one of the main goals of this project.

7.3 Imaging and DIC

All experimental tests were recorded using DIC for tracking surface displacement and strain. The two lenses used were found to have slightly different aperture sizes which caused challenges with calibration and set-up. The fact that specimens needed a larger

depth of field meant that the apertures were reduced resulting in additional light sources being required. The lighting and camera positions were adjusted until acceptable calibration residuums were achieved. The author encountered the most challenges with achieving the correct lighting and camera set-up, which took far longer than any other sub-set of the experimental set-up. Different DIC settings were investigated for each specimen type, with a facet overlap of one third resulting in better correlations. The uniaxial and round bulge specimens used similar settings since the speckle patterns were similar and the cameras used of each type of testing have similar resolutions. The elliptical specimens required a coarser grid spacing due to the larger speckle patterns.

7.4 Recommendations

- Higher quality lenses with equal aperture sizes at each aperture setting would result in easier camera set-up.
- Using cameras that can be controlled directly via the Dantec Istra-4D software would result in a much faster and easier calibration process and a faster turnover time for testing.
- Achieving a finer speckle pattern would result in higher quality data and results from testing. The speckle patterns had the largest negative effect on data quality in this project.
- Using the strain rate profile of a bulge test at a constant motor speed and inflation rate, it should be possible to create a varying motor speed profile that will result in less variation in strain rate at the apex during the test, an example is seen in Figure 6.6.
- Design a clamp or device to achieve a flatter start position for specimens when setting up the bulge tester. A possible solution is to use a 3D-printed tamp with a shoulder to provide a surface for the specimen to rest on in the exact flat zero position when the inflation chamber is inverted upside-down for purging of air. Currently the specimens sag a small amount when inverted upside down due to the head of water. If the specimen lay flat against a surface in the correct start position rather than sagging, it should remain in the correct position when turned back the right way up.

References

[1] G. Machado, D. Favier, and G. Chagnon, "Membrane Curvatures and Stress-strain Full Fields of Axisymmetric Bulge Tests from 3D-DIC Measurements. Theory and Validation on Virtual and Experimental results," *Experimental Mechanics*, vol. 52, no. 7, pp. 865–880, 2012.

[2] A. Graham, "No Title," Masters Dissertation, University of Cape Town, 2019.

[3] M. Geerligs, *Skin layer mechanics*, 2010. [Online]. Available: http://131.155.54.17/mate/pdfs/11390.pdf

[4] T. K. Tonge, L. S. Atlan, L. M. Voo, and T. D. Nguyen, "Full-field bulge test for planar anisotropic tissues: Part I-Experimental methods applied to human skin tissue," *Acta Biomaterialia*, vol. 9, no. 4, pp. 5913–5925, 2013. [Online]. Available: http://dx.doi.org/10.1016/j.actbio.2012.11.035

[5] R. Reihsner, B. Balogh, and E. J. Menzel, "Two-dimensional elastic properties of human skin in terms of an incremental model at the in vivo configuration," *Medical Engineering and Physics*, vol. 17, no. 4, pp. 304–313, 1995.

[6] W. Sun, M. S. Sacks, and M. J. Scott, "Effects of Boundary Conditions on the Estimation of the Planar Biaxial Mechanical Properties of Soft Tissues," *Journal of Biomechanical Engineering*, vol. 127, no. 4, p. 709, 2006.

[7] A. J. Gallagher, A. Ní Anniadh, K. Bruyere, M. Otténio, H. Xie, and M. D. Gilchrist, "Dynamic tensile properties of human skin," in *2012 IRCOBI Conference Proceedings - International Research Council on the Biomechanics of Injury*, 2012.

[8] A. Delalleau, G. Josse, J. M. Lagarde, H. Zahouani, and J. M. Bergheau, "A nonlinear elastic behavior to identify the mechanical parameters of human skin in vivo," *Skin Research and Technology*, vol. 14, no. 2, pp. 152–164, 2008.

[9] K. Langer, "On the anatomy and physiology of the skin. I. The cleavability of the cutis," *British Journal of Plastic Surgery*, vol. 31, no. 1, pp. 3–8, 1978.

[10] A. N. Annaidh, Karine Bruyère, M. Destrade, M. D. Gilchrist, C. Maurini, M. Otténio, and G. Saccomandi, "Automated estimation of collagen fibre dispersion in the dermis and its contribution to the anisotropic behaviour of skin," *Annals of Biomedical Engineering*, vol. 40, no. 8, pp. 1666–1678, 2012.

[11] T. Sugihara, T. Ohura, K. Homma, and H. H. Igawa, "The extensibility in human skin: variation according to age and site," *British Journal of Plastic Surgery*, vol. 44, no. 6, pp. 418–422, 1991.

[12] A. Ní Annaidh, K. Bruyère, M. Destrade, M. D. Gilchrist, and M. Otténio, "Characterization of the anisotropic mechanical properties of excised human skin," *Journal of the Mechanical Behavior of Biomedical Materials*, vol. 5, no. 1, pp. 139–148, 2012. [Online]. Available: http://dx.doi.org/10.1016/j.jmbbm.2011.08.016

[13] L. H. Jansen and P. B. Rottier, "Comparison of the mechanical properties of strips of human abdominal skin excised from below and from above the umbilic," *Dermatology*, 1958.

[14] M. G. Dunn and F. H. Silver, "Viscoelastic behavior of human connective tissues: Relative contribution of viscous and elastic components," *Connective Tissue Research*, 1983.

[15] H. G. VOGEL, "Age dependence of mechanical and biochemical properties of human skin. I: Stress-strain experiments, skin thickness and biochemical analysis," *Bioengineering and the skin*, 1987.

[16] C. Jacquemoud, K. Bruyere-Garnier, and M. Coret, "Methodology to determine failure characteristics of planar soft tissues using a dynamic tensile test," *Journal of Biomechanics*, 2007.

[17] P. G. Agache, C. Monneur, J. L. Leveque, and J. De Rigal, "Mechanical properties and Young's modulus of human skin in vivo," *Archives of Dermatological Research*, 1980.

[18] S. Diridollou, M. Berson, V. Vabre, D. Black, B. Karlsson, F. Auriol, J. M. Gregoire, C. Yvon, L. Vaillant, Y. Gall, and F. Patat, "An in vivo method for measuring the mechanical properties of the skin using ultrasound," *Ultrasound in Medicine and Biology*, 1998.

[19] F. Khatyr, C. Imberdis, P. Vescovo, D. Varchon, and J. M. Lagarde, "Model of the viscoelastic behaviour of skin in vivo and study of anisotropy," *Skin Research and Technology*, 2004.

[20] C. Pailler-Mattei, S. Bec, and H. Zahouani, "In vivo measurements of the elastic mechanical properties of human skin by indentation tests," *Medical Engineering and Physics*, 2008.

[21] H. Zahouani, C. Pailler-Mattei, B. Sohm, R. Vargiolu, V. Cenizo, and R. Debret, "Characterization of the mechanical properties of a dermal equivalent compared with human skin in vivo by indentation and static friction tests," *Skin Research and Technology*, 2009.

[22] Z. Liu and K. Yeung, "The Preconditioning and Stress Relaxation of Skin Tissue," *Journal of Biomedical & Pharmaceutical Engineering*, vol. 1, no. 1, pp. 22–28, 2008.

[23] H. Seibert, T. Scheffer, and S. Diebels, "Biaxial testing of elastomers - Experimental setup, measurement and experimental optimisation of specimen's shape," *Technische Mechanik*, vol. 34, no. 2, pp. 72–89, 2014.

[24] L. R. G. Treloar, *The physics of rubber elasticity.* Oxford University Press, USA, 1975.

[25] B. Cruz Perez, J. Tang, H. J. Morris, J. R. Palko, X. Pan, R. T. Hart, and J. Liu, "Biaxial mechanical testing of posterior sclera using high-resolution ultrasound speckle tracking for strain measurements," *Journal of Biomechanics*, vol. 47, no. 5, pp. 1151–1156, 2014. [Online]. Available: http://dx.doi.org/10.1016/j.jbiomech.2013.12.009

[26] A. Avanzini and D. Battini, "Integrated experimental and numerical comparison of different approaches for planar biaxial testing of a hyperelastic material," *Advances in Materials Science and Engineering*, vol. 2016, 2016.

[27] N. Kumaraswamy, "Characterization of Biaxial Mechanical Properties of Rubber and Skin," Ph.D. dissertation, The University of Texas at Austin, 2014.

[28] L. C. Gerhardt, J. Schmidt, J. A. Sanz-Herrera, F. P. Baaijens, T. Ansari, G. W. Peters, and C. W. Oomens, "A novel method for visualising and quantifying through-plane skin layer deformations," *Journal of the Mechanical Behavior of Biomedical Materials*, vol. 14, pp. 199–207, 2012. [Online]. Available: http://dx.doi.org/10.1016/j.jmbbm.2012.05.014

[29] F. M. Hendriks, D. Brokken, C. W. J. Oomens, D. L. Bader, and F. P. T. Baaijens, "The relative contributions of different skin layers to the mechanical behavior of human skin in vivo using suction experiments," *Medical Engineering and Physics*, vol. 28, no. 3, pp. 259–266, 2006.

[30] L. Yu and B. Pan, "Full-frame, high-speed 3D shape and deformation measurements using stereo-digital image correlation and a single color high-speed camera," *Optics and Lasers in Engineering*, vol. 95, no. March, pp. 17–25, 2017. [Online]. Available: http://dx.doi.org/10.1016/j.optlaseng.2017.03.009

[31] M. A. Sutton, "Digital Image Correlation for Shape and Deformation Measurements," in *Springer Handbook of Experimental Solid Mechanics*, 2008.

[32] H. Joodaki and M. B. Panzer, "Skin mechanical properties and modeling: A review," 2018.

[33] G. A. Holzapfel, *Nonlinear solid mechanics : a continuum approach for engineering*. Wiley, 2000.

[34] UK Health and Safety Executive, "Manual Handling at Work: A Brief Guide," 2020.

[35] R. Curry, "Response of plates subjected to air-blast and buried explosions," Ph.D. dissertation, University of Cape Town, 2017.

[36] G. Kemmer and S. Keller, "Nonlinear least-squares data fitting in Excel spreadsheets," *Nature Protocols*, vol. 5, no. 2, pp. 267–281, 2010. [Online]. Available: http://dx.doi.org/10.1038/nprot.2009.182

Appendices

Appendix A

Engineering Drawings and Device Images

ITEM NO.	PART NUMBER	QTY.
1	Base_Plate	1
2	Linear_Rail	2
3	Bearing_Block_Fixed	1
4	Bearing_Block_Float	1
5	Screw	1
6	Linear_Guide_Block	3
7	Ball_Nut	1
8	Nut_Housing	1
9	Connect_Plate	1
10	Syringe_Block	1
11	Plunger_Clamp	1
12	Rubber_Foot	4
14	Syringe_Wedge	1
16	Limit_switch_trigger_left	1
17	Limit_switch_trigger_right	1
18	Limit_switch	2
19	Limit_switch_bracket	1
20	nema 23 mount	1
21	Nema 23	1
22	GT2_40teeth_8bore	1
23	GT2_20Teeth_5bore_6wide	1
24	GT2_belt_158mm_75teeth	1
25	Belt tensioner_nema23	1

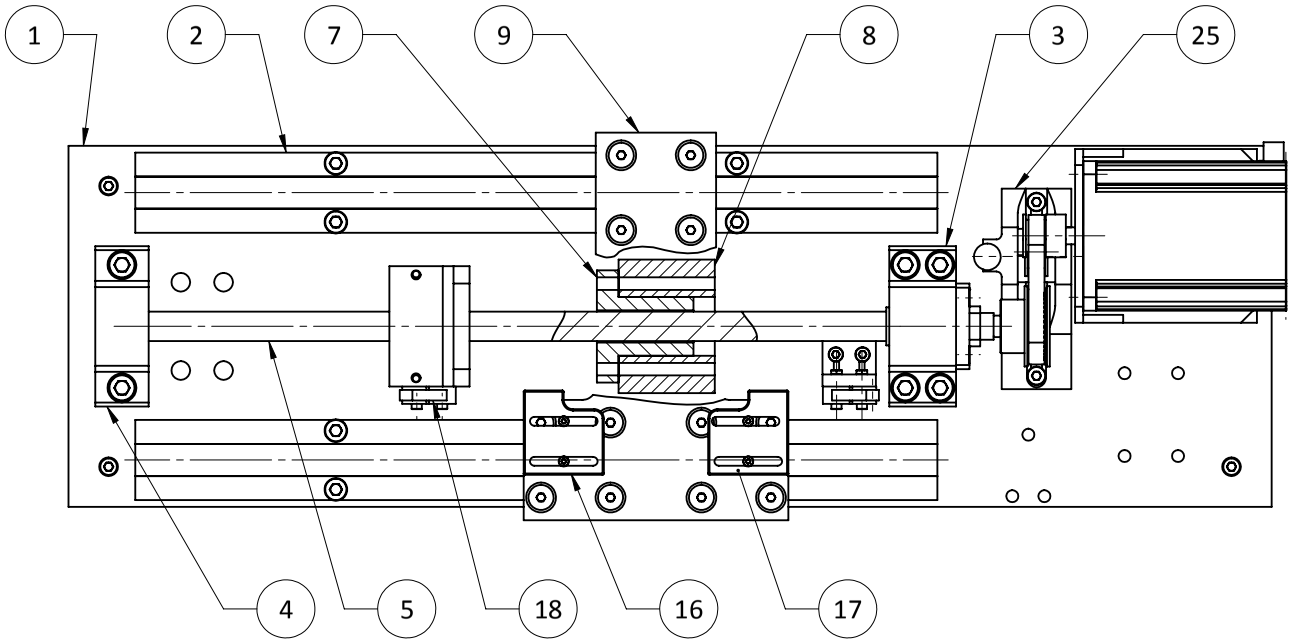

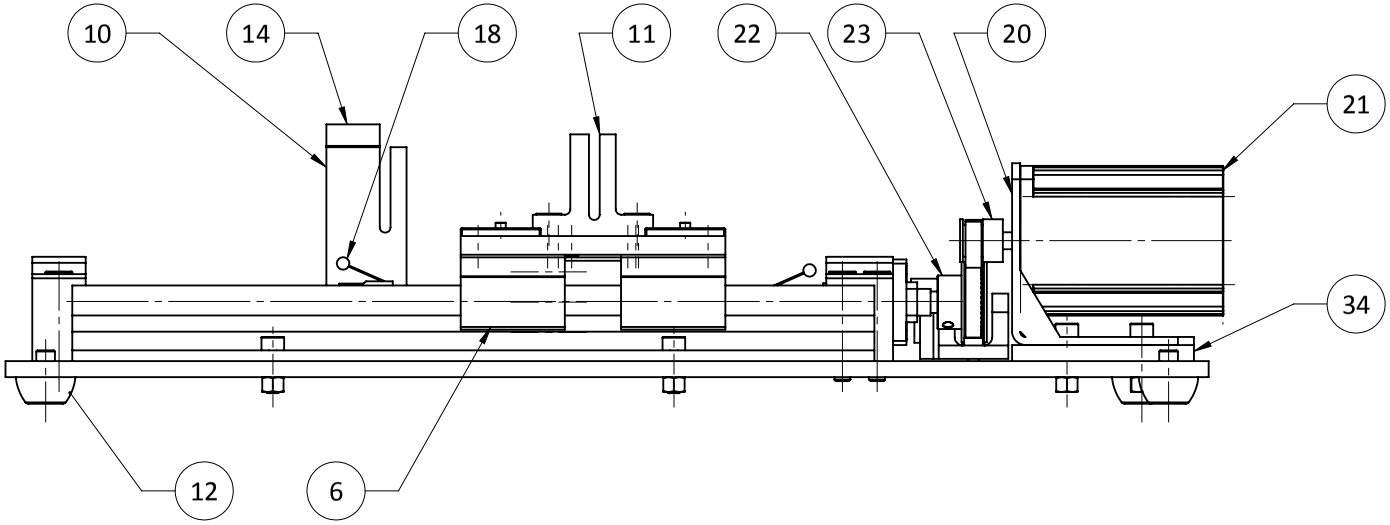

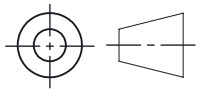

SOLIDWORKS Educational Product. For Instructional Use Only

DEPARTMENT OF MECHANICAL ENGINEERING | M.Sc.

GENERAL NOTES:
All measurements are in millimeters.
Do not measure off the drawing.
Deburr and break all sharp edges.

SCALE 1:2

DRAWN BY	Andrew Curry
STUDENT No:	CRRAND009
SUPERVISOR:	Dr. R. Govender
SUPERVISOR SIGNATURE:	

TITLE: SYRINGE PUMP ASSEMBLY

DRAWING No: 2019-SYR-PUMP-ASSEMBLY | REVISION: 1 | SHEET: 1

ITEM NO.	PART NUMBER	QTY.
1	Main_chamber	1
2	Clamp_50A_2T_bottom	1
3	Clamp_50A_top	1
4	RA_45_t_piece	1
5	Ball valve	1
6	Inlet_connector_6mm	1
7	M5_hex bolt	6
8	M5_hex_nut	6

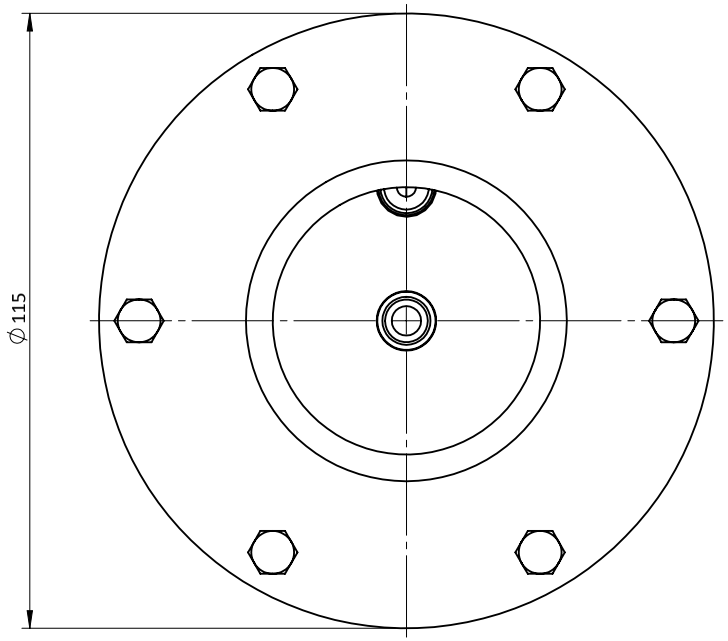

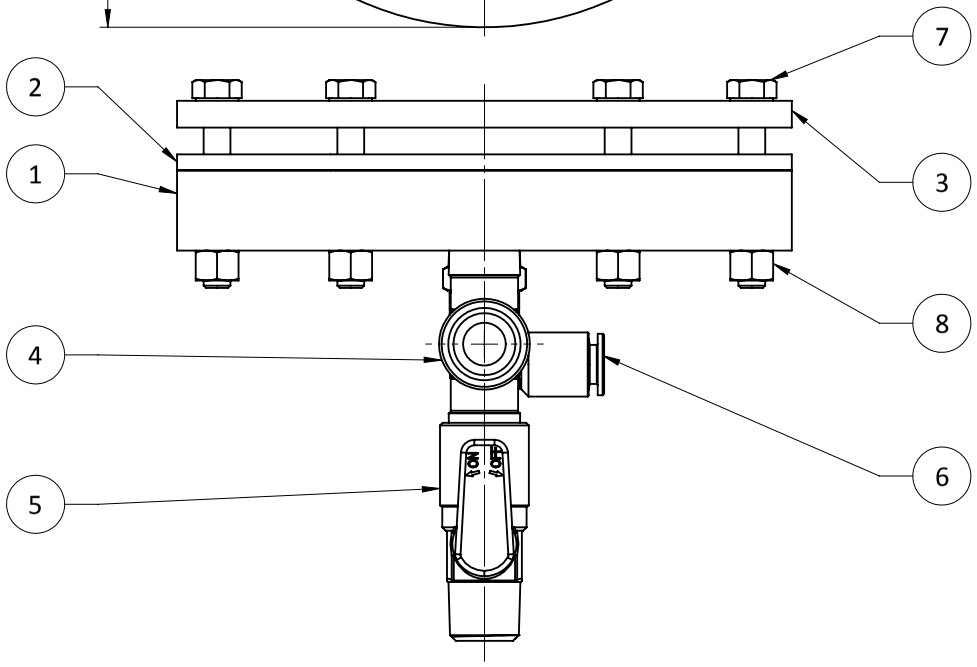

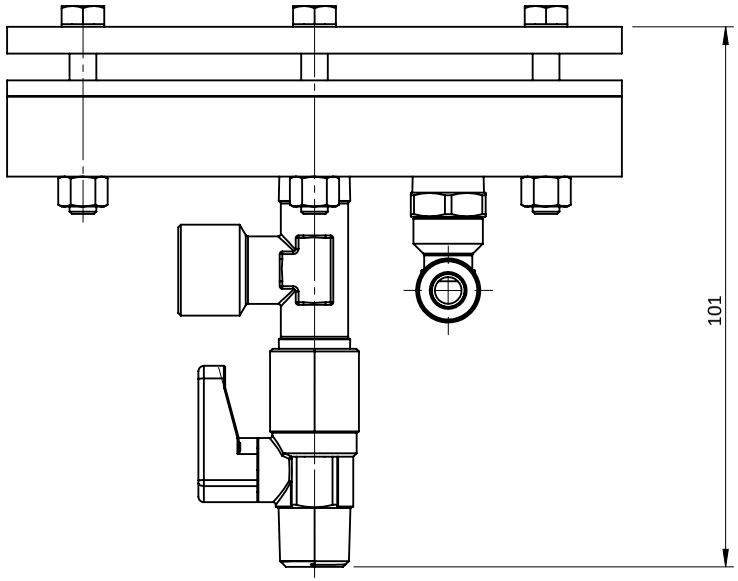

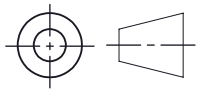

SOLIDWORKS Educational Product. For Instructional Use Only

DEPARTMENT OF MECHANICAL ENGINEERING | M.Sc.

GENERAL NOTES:
All measurements are in millimeters.
Do not measure off the drawing.
Deburr and break all sharp edges.

SCALE 1:1

DRAWN BY	Andrew Curry
STUDENT No:	CRRAND009
SUPERVISOR:	Dr. R. Govender
SUPERVISOR SIGNATURE:	

TITLE: INFLATION CHAMBER ASSEMBLY

DRAWING No: 2019-INF-ASSEMBLY | REVISION: 1 | SHEET: 1

ITEM NO.	PART NUMBER	QTY.
1	Belt tensioner_nema23	1
2	tensioner_key_triangle	1
3	idler	1
4	tensioner_shaft	1

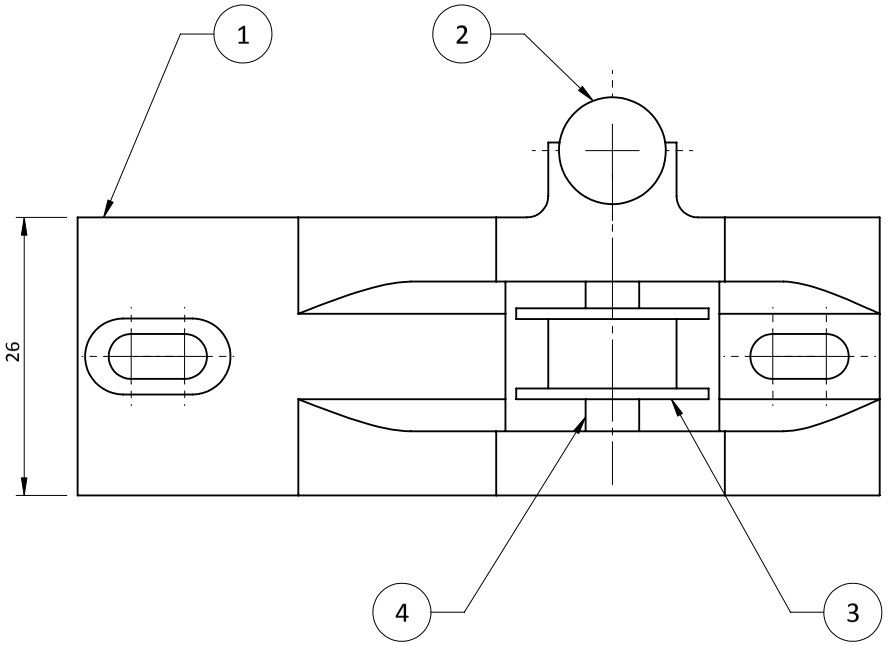

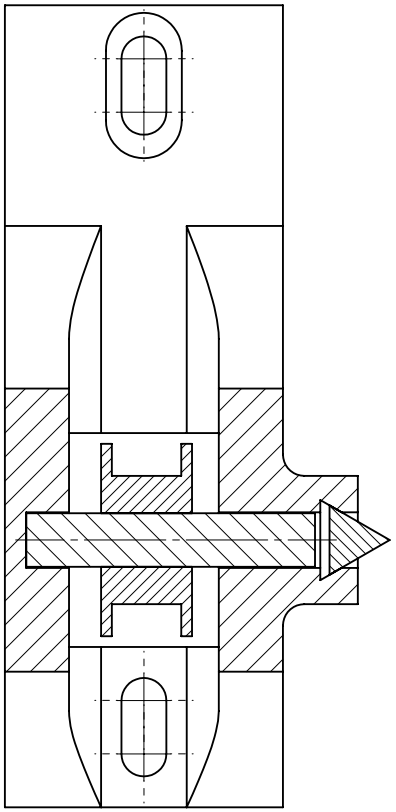

SECTION A-A
SCALE 2:1

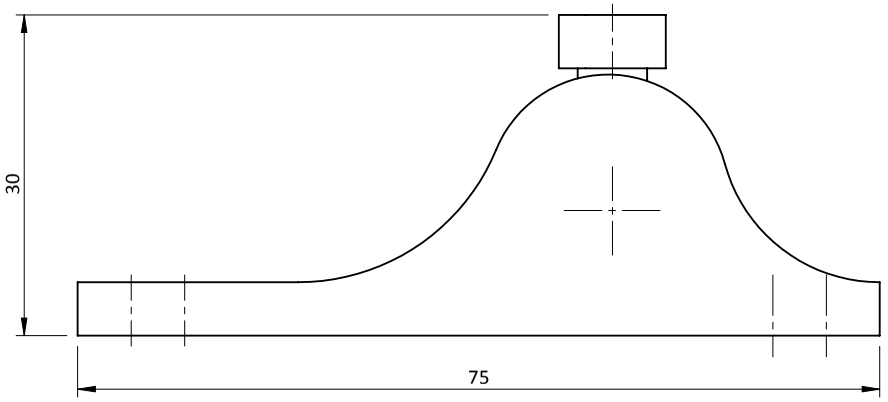

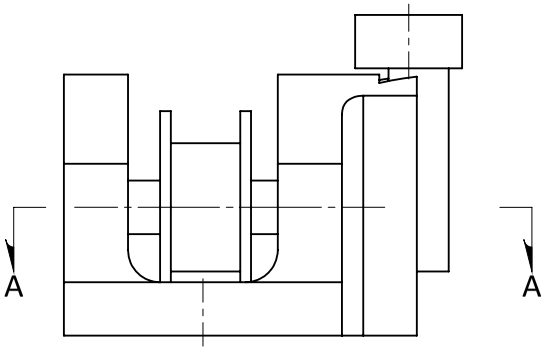

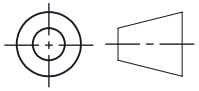

SOLIDWORKS Educational Product. For Instructional Use Only

DEPARTMENT OF MECHANICAL ENGINEERING | M.Sc.

GENERAL NOTES:
All measurements are in millimeters.
Do not measure off the drawing.
Deburr and break all sharp edges.

SCALE 2:1

DRAWN BY	Andrew Curry
STUDENT No:	CRRAND009
SUPERVISOR:	Dr. R. Govender
SUPERVISOR SIGNATURE:	

TITLE: BELT TENSIONER ASSEMBLY

DRAWING No: 2019-TENSION-ASSEMBLY | REVISION: 1 | SHEET: 1

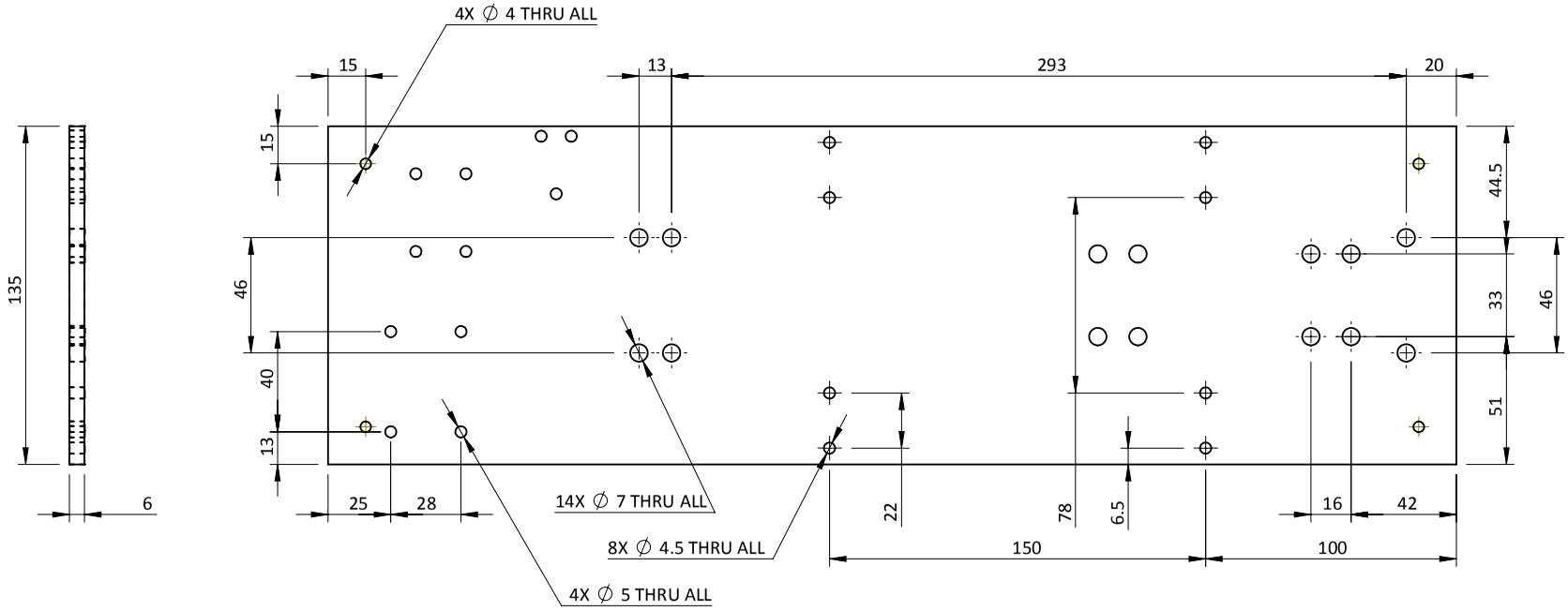

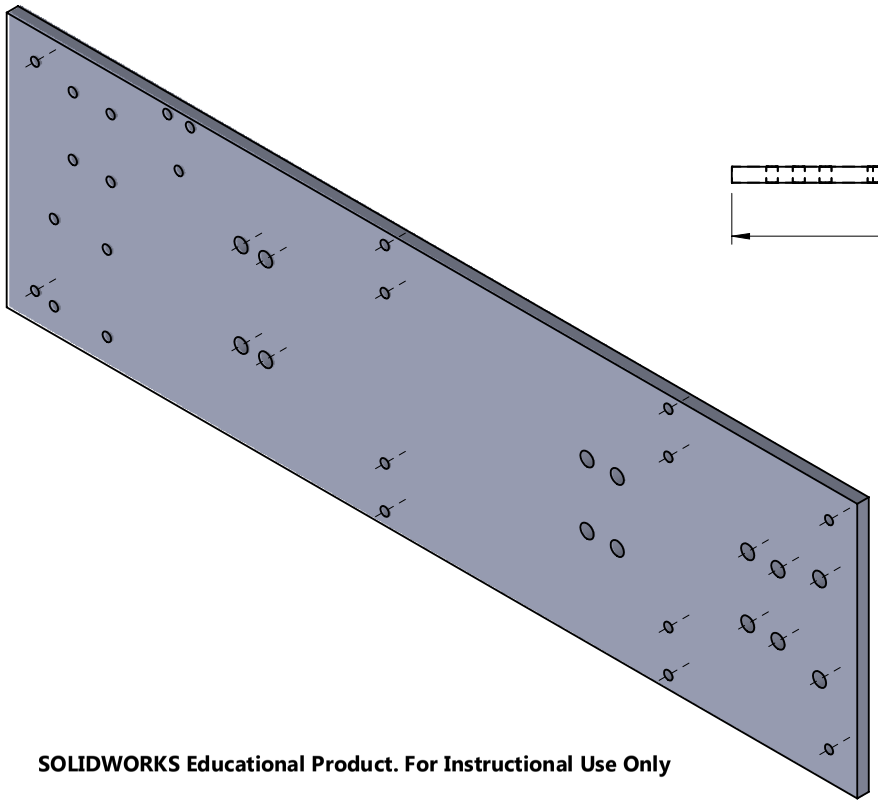

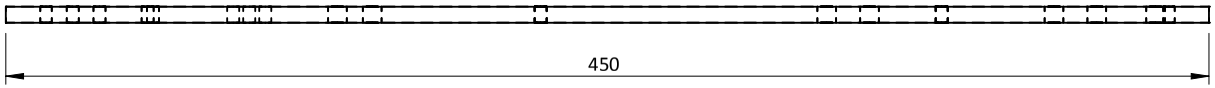

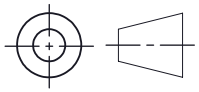

MAT'L: MILD STEEL

SOLIDWORKS Educational Product. For Instructional Use Only

DEPARTMENT OF MECHANICAL ENGINEERING				M.Sc.	
GENERAL NOTES: All measurements are in millimeters. Do not measure off the drawing. Deburr and break all sharp edges.		DRAWN BY	Andrew Curry	TITLE: BASE PLATE	
		STUDENT No:	CRRAND009		
		SUPERVISOR:	Dr. R. Govender		
SCALE	1:2	SUPERVISOR SIGNATURE:		DRAWING No: 2019-BASE-PLATE	REVISION: 1 / SHEET: 1

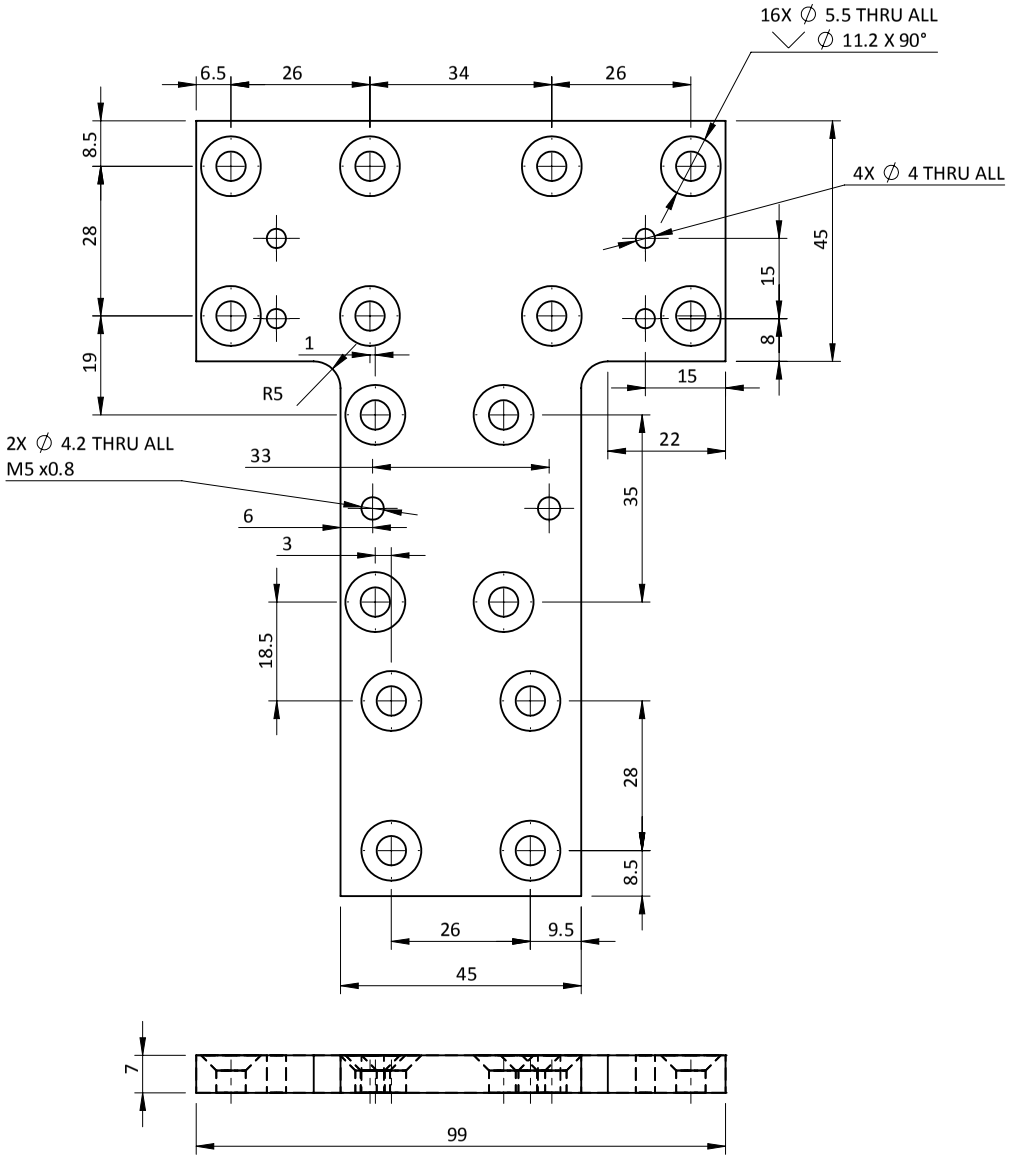

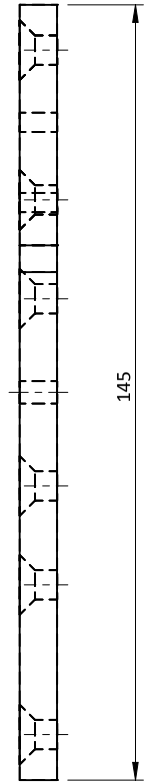

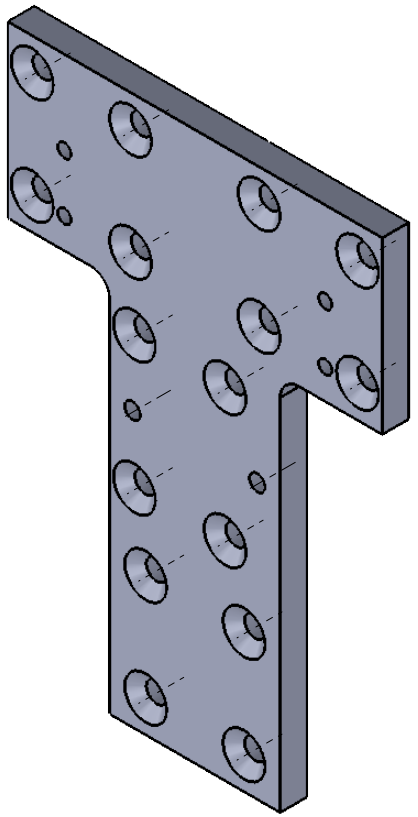

MAT'L: STAINLESS STEEL 316

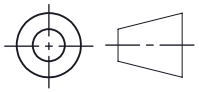

SOLIDWORKS Educational Product. For Instructional Use Only

DEPARTMENT OF MECHANICAL ENGINEERING				M.Sc.	
GENERAL NOTES: All measurements are in millimeters. Do not measure off the drawing. Deburr and break all sharp edges.		DRAWN BY	Andrew Curry	TITLE: T-PLATE	
		STUDENT No:	CRRAND009		
		SUPERVISOR:	Dr. R. Govender		
SCALE	1:1	SUPERVISOR SIGNATURE:		DRAWING No: 2019-T-PLATE	REVISION: 2 / SHEET: 1

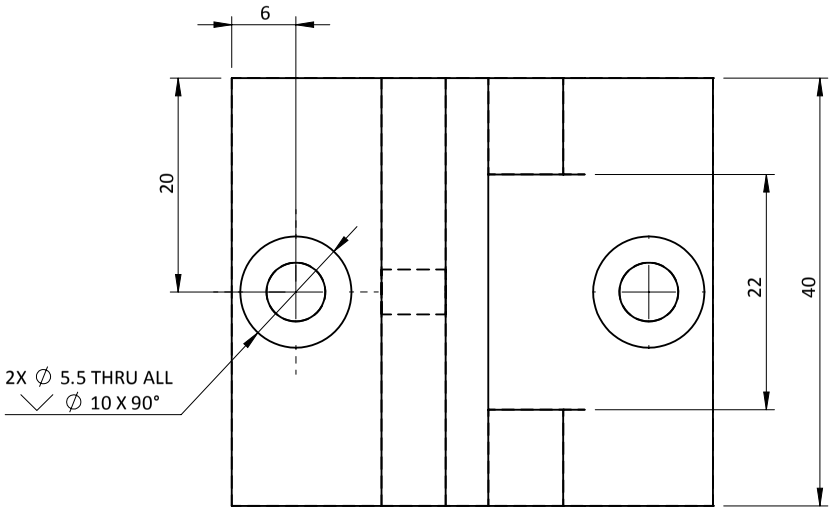

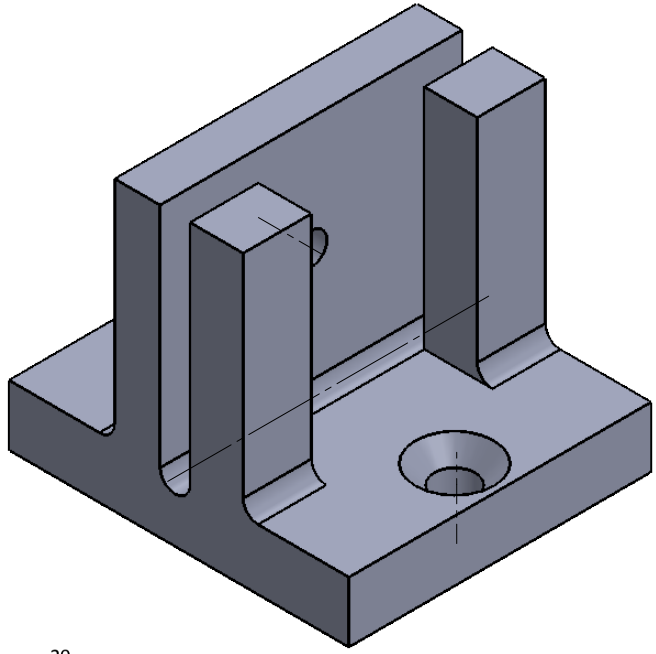

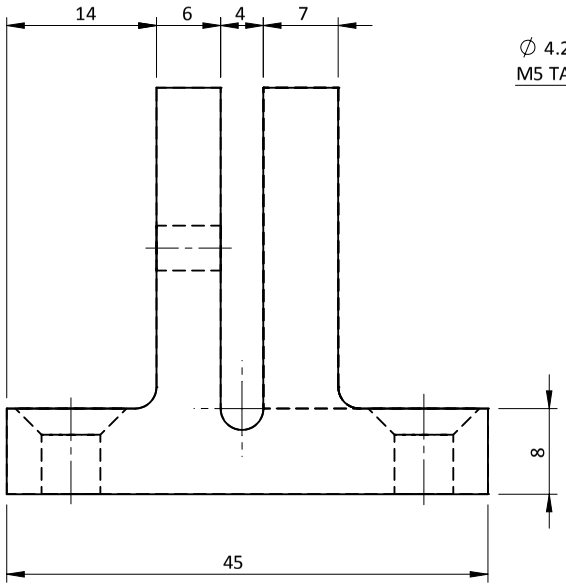

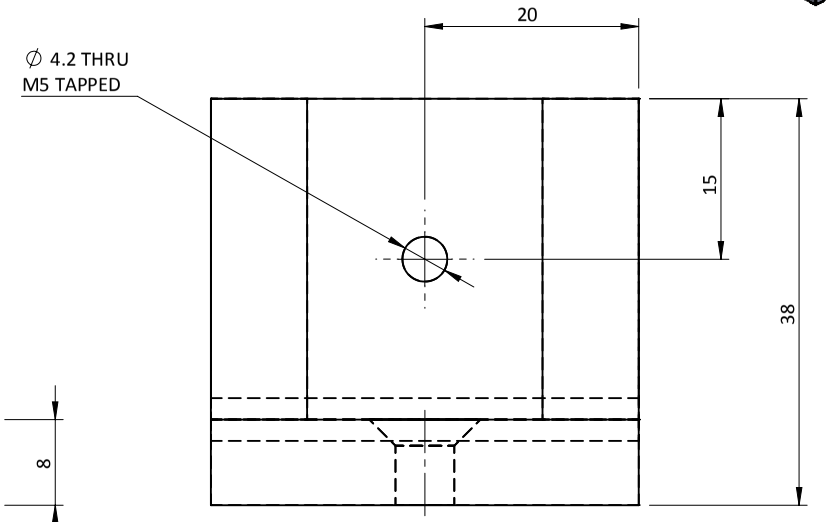

MAT'L: STAINLESS STEEL 316

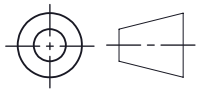

SOLIDWORKS Educational Product. For Instructional Use Only

DEPARTMENT OF MECHANICAL ENGINEERING			M.Sc.
GENERAL NOTES: All measurements are in millimeters. Do not measure off the drawing. Deburr and break all sharp edges.	DRAWN BY	Andrew Curry	TITLE: SYRING _PLUNGER BLOCK
	STUDENT No:	CRRAND009	
	SUPERVISOR:	Dr. R. Govender	
SCALE 1:1	SUPERVISOR SIGNATURE:		DRAWING No: 2019-PLUNGER-BLOCK REVISION: 1 SHEET: 1

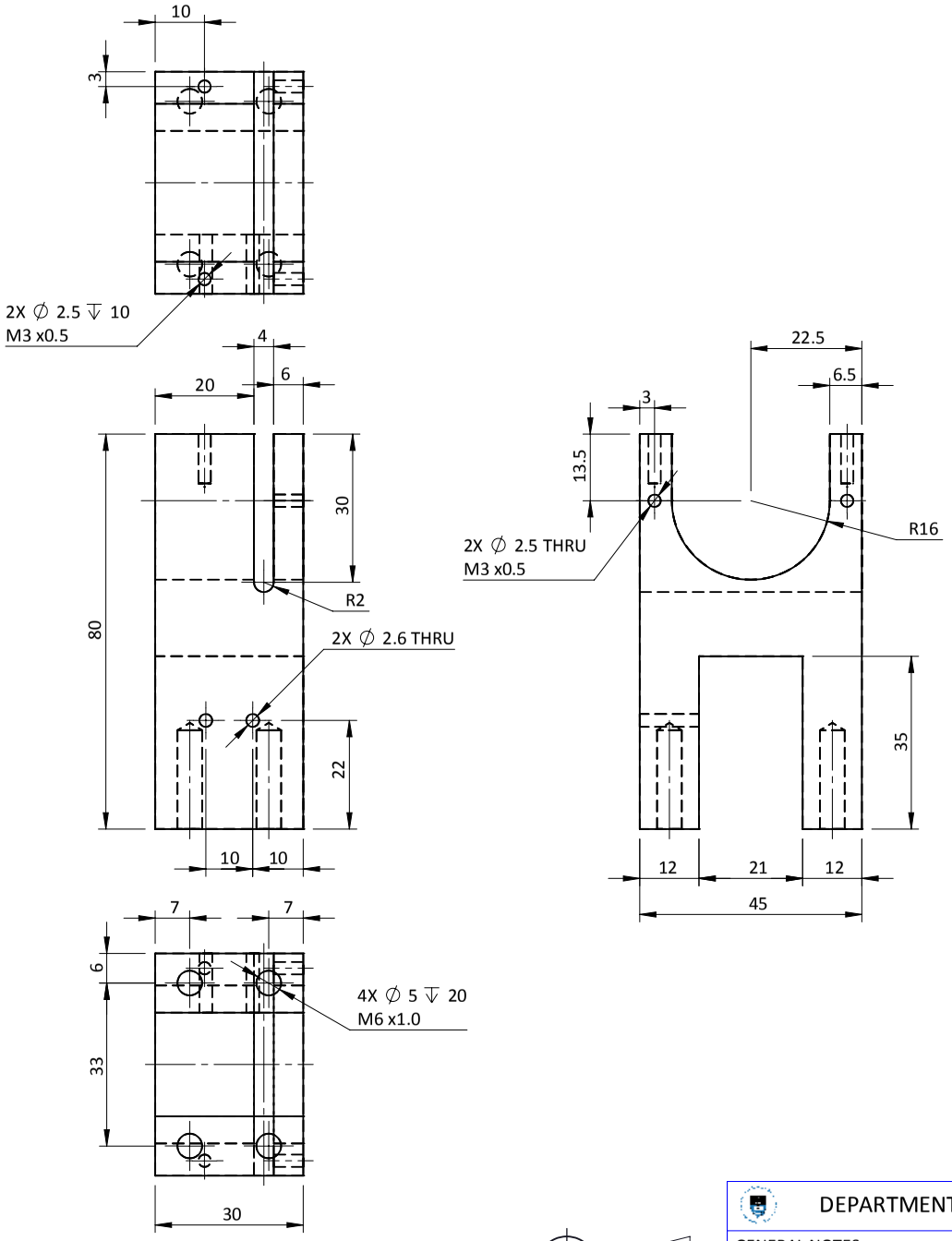

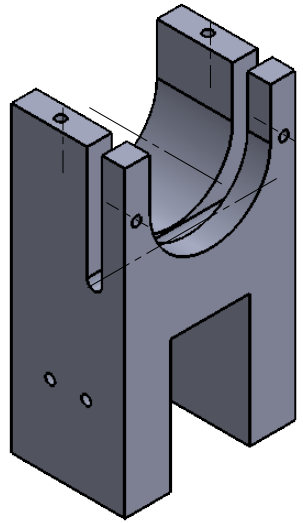

MAT'L: STAINLESS STEEL 316

SOLIDWORKS Educational Product. For Instructional Use Only

DEPARTMENT OF MECHANICAL ENGINEERING				M.Sc.	
GENERAL NOTES: All measurements are in millimeters. Do not measure off the drawing. Deburr and break all sharp edges.		DRAWN BY	Andrew Curry	TITLE: SYRINGE BLOCK	
		STUDENT No:	CRRAND009		
		SUPERVISOR:	Dr. R. Govender		
SCALE	1:1	SUPERVISOR SIGNATURE:		DRAWING No: 2019-SYRINGE-BLOCK	REVISION: 2 / SHEET: 1

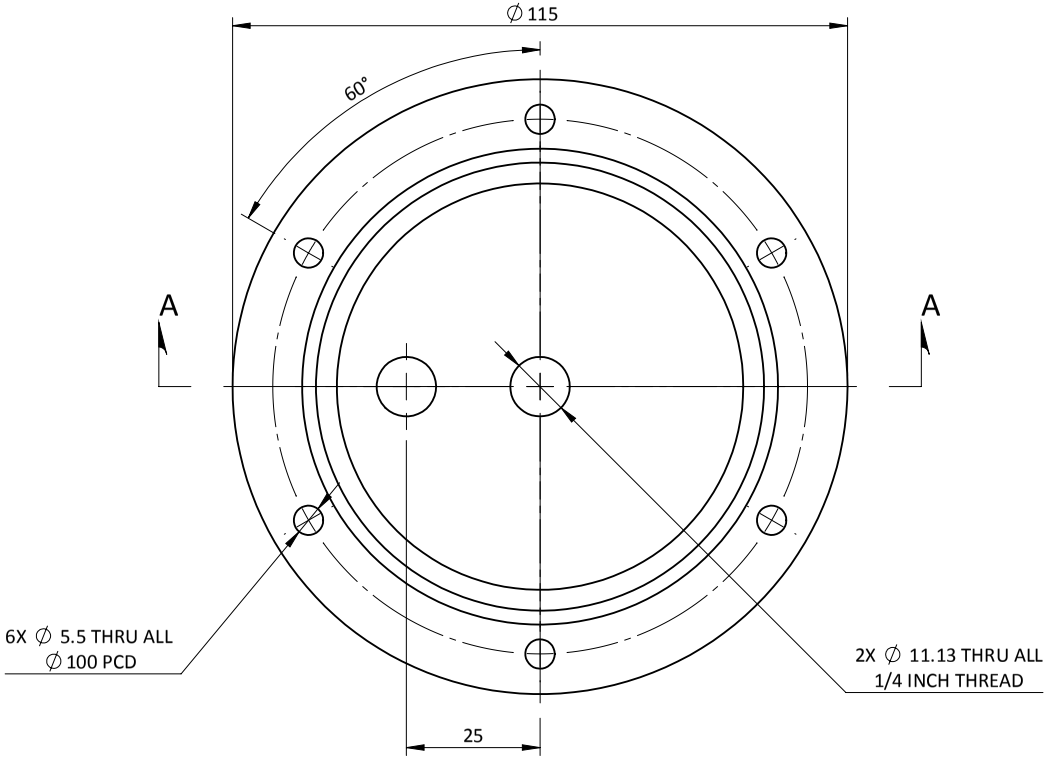

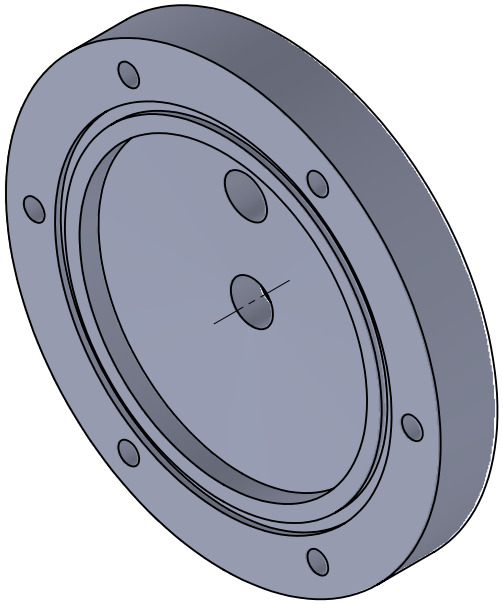

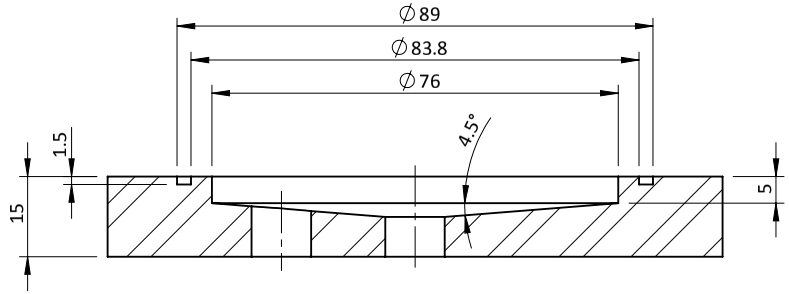

SECTION A-A

MAT'L: STAINLESS STEEL

SOLIDWORKS Educational Product. For Instructional Use Only

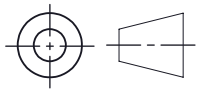

DEPARTMENT OF MECHNICAL ENGINEERING				M.Sc.	
GENERAL NOTES: All measurements are in millimeters. Do not measure off the drawing. Deburr and break all sharp edges.		DRAWN BY	Andrew Curry	TITLE: MAIN CHAMBER	
		STUDENT No:	CRRAND009		
		SUPERVISOR:	Dr. R. Govender		
SCALE	1:1	SUPERVISOR SIGNATURE:		DRAWING No: 2019-MAIN-CHAMBER	REVISION: 1 / SHEET: 1

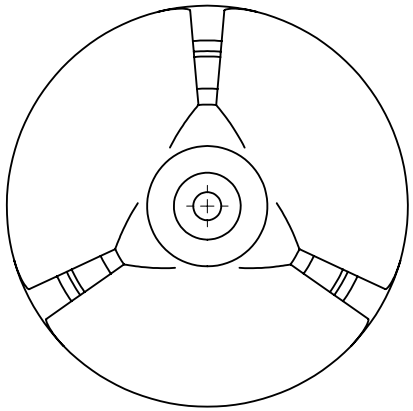

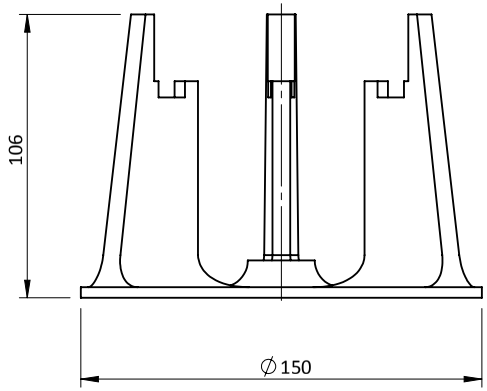

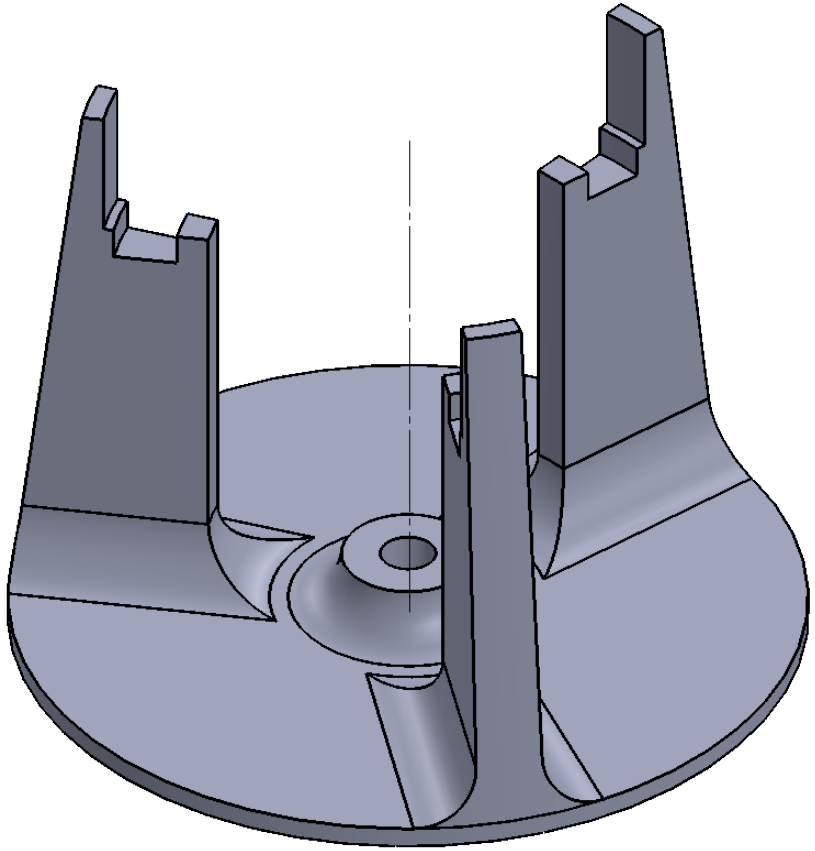

NOTE: 3D PRINT PART

MAT'L: PLA

DEPARTMENT OF MECHANICAL ENGINEERING			M.Sc.		
GENERAL NOTES: All measurements are in millimeters. Do not measure off the drawing. Deburr and break all sharp edges.	DRAWN BY	Andrew Curry	TITLE: INFLATION CHAMBER STAND		
	STUDENT No:	CRRAND009			
	SUPERVISOR:	Dr. R. Govender			
SCALE 1:1	SUPERVISOR SIGNATURE:		DRAWING No: 2019-STAND	REVISION: 1	SHEET: 1

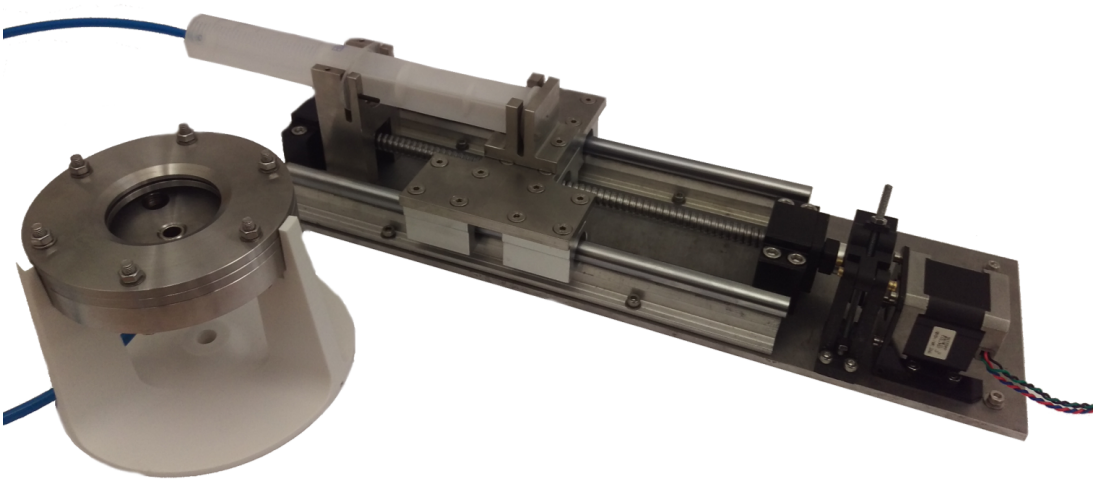

Figure A.1 Image of the syringe pump and inflation chamber.

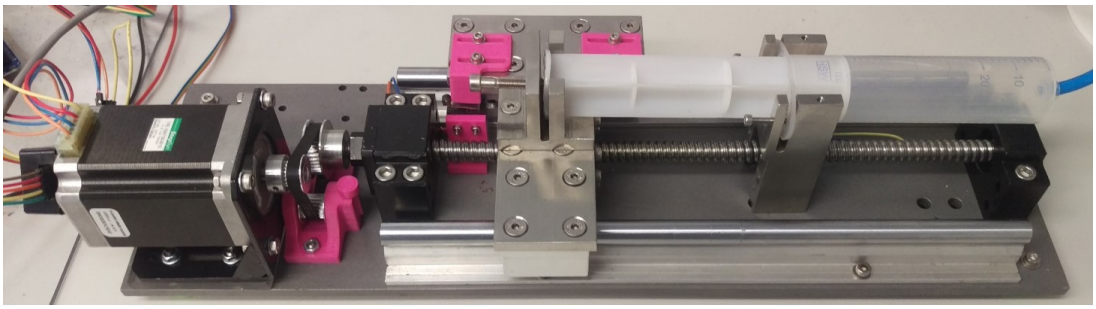

Figure A.2 Image of syringe pump with a 60 ml syringe installed.

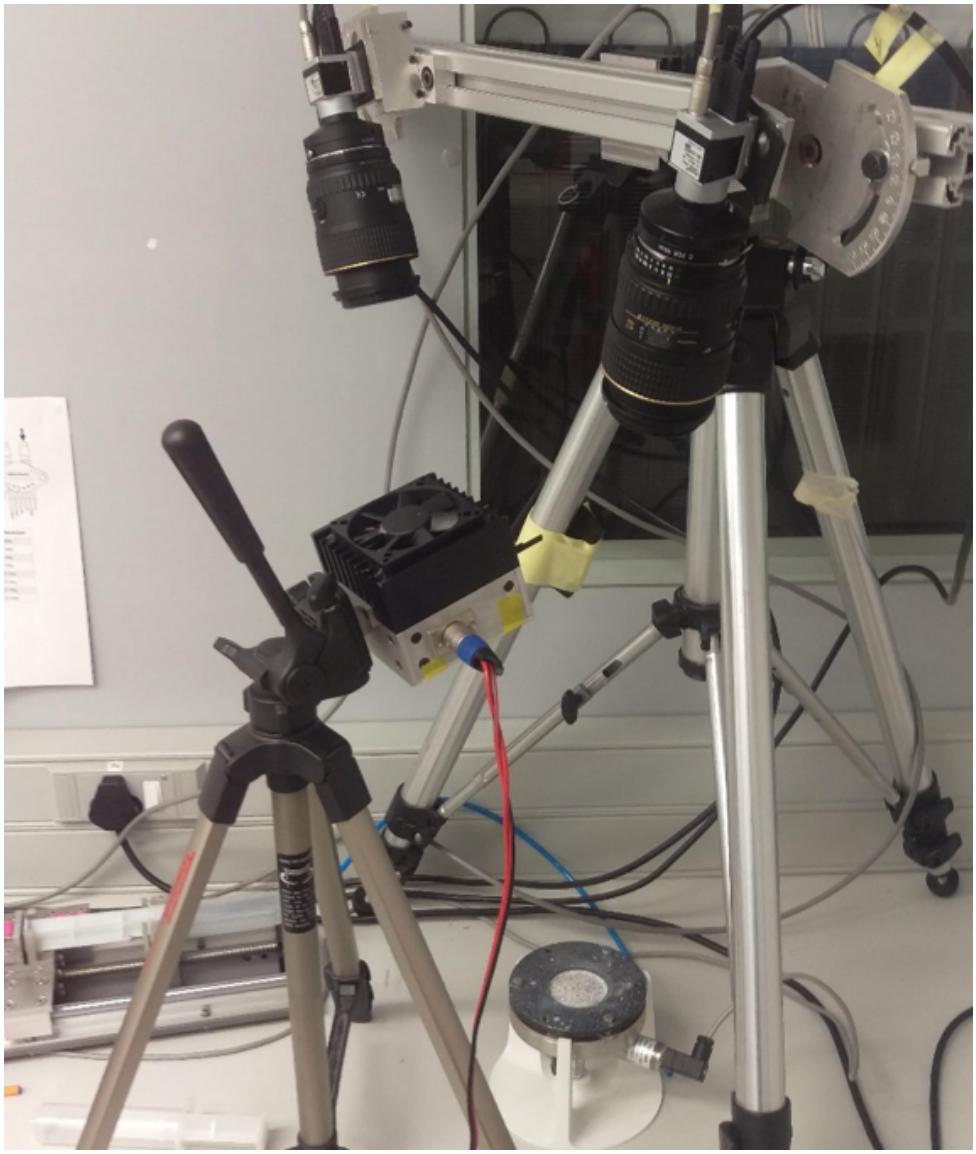

Figure A.3 Image of camera and lighting set up.

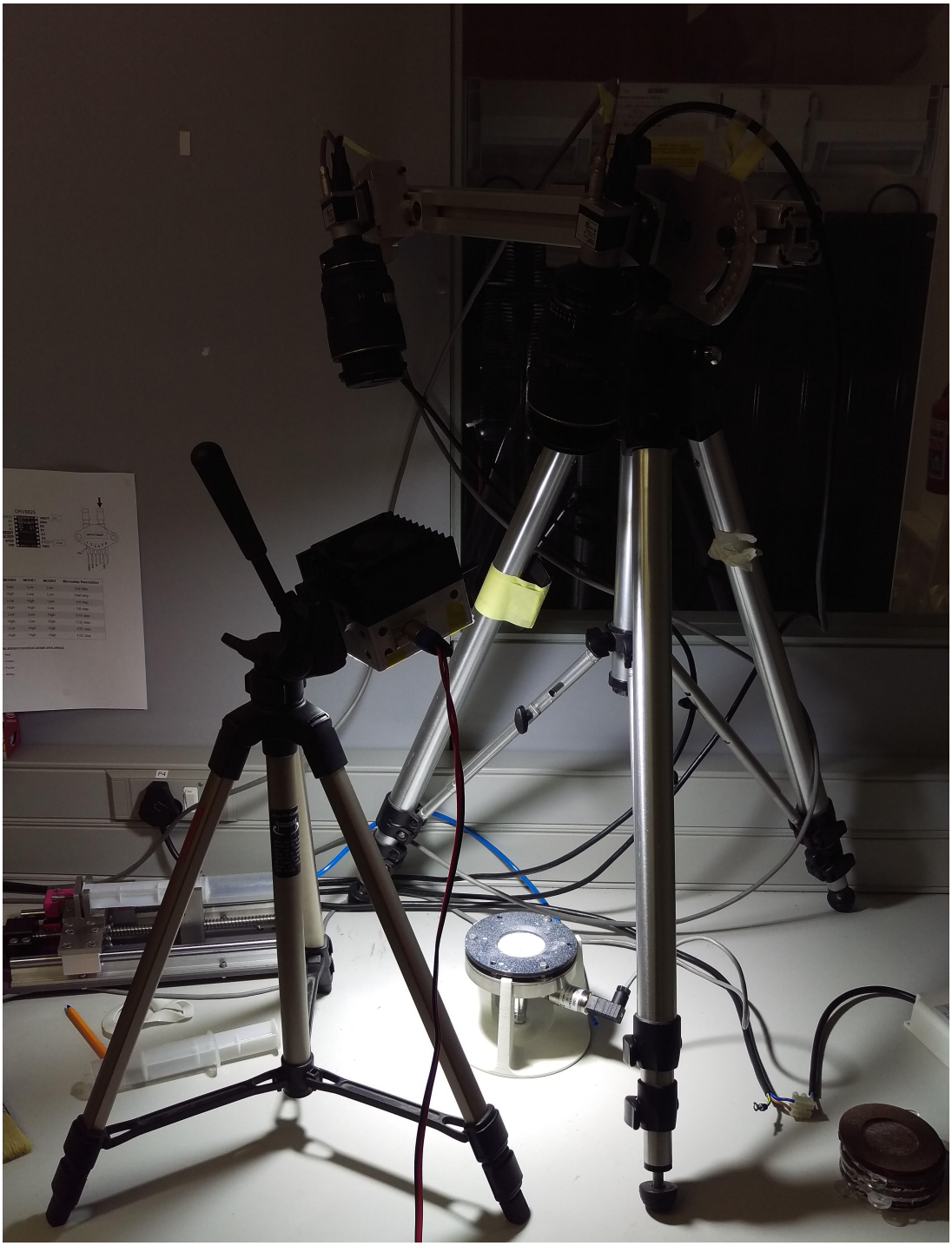

Figure A.4 Image of camera and lighting set up running during a test.

Appendix B

Electronics wiring diagram

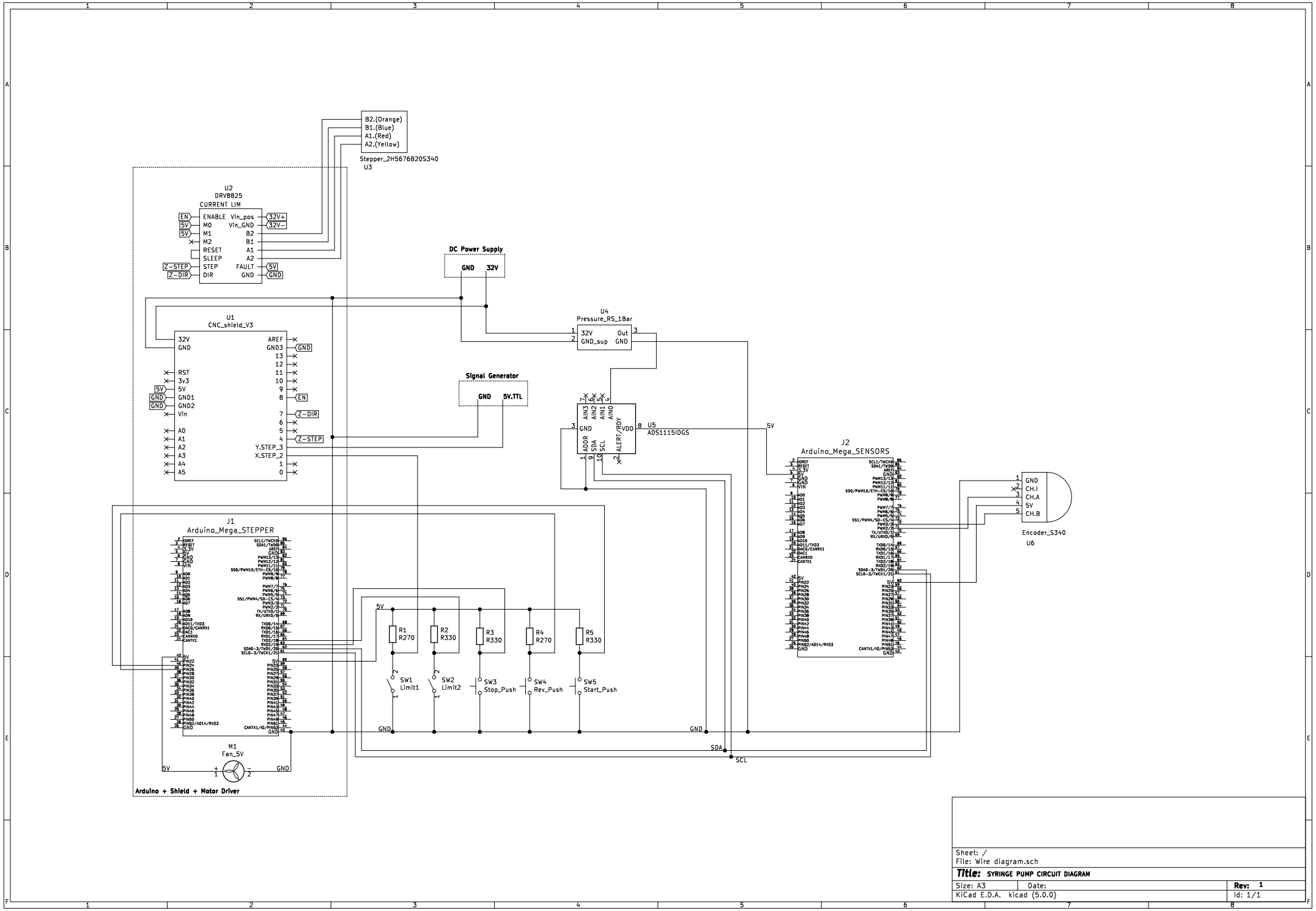

Sheet: /
File: Wire diagram.sch

Title: SYRINGE PUMP CIRCUIT DIAGRAM

Size: A3	Date:	Rev: 1
KiCad E.D.A. kicad (5.0.0)		Id: 1/1

Appendix C

Arduino code

C.1 Motor Arduino Code

This code is uploaded to the Motor-Arduino that controls the stepper motor with push-button and limit switch inputs. The major functions of this code are to control the stepper motor and signal the Sensor Arduino to start of stop data capture.

```
#include <Arduino.h>
#include <Wire.h>
#define MOTOR_STEPS 200
#define RPM 0
//Stepper driver board pins
#define DIR 7
#define STEP 4
#define ENABLE 8
//Stepper driver board
#include "DRV8825.h"
#define MODE0 3
#define MODE1 7
#define MODE2 6
DRV8825 stepper(MOTOR_STEPS, DIR, STEP, ENABLE, MODE0, MODE1,
    MODE2);
/////            MOTOR SPEED INPUT  (This is the speed on the
    motor calibrated)
float MotorSpeedINPUT = 10;
/////
//Button flags setup
```

```
//Sets to stop mode so that the stepper doesnt move when system
   starts up
bool limit_1 = false; // limit switch at the end of stoke
bool limit_2 = false; // limit switch at begining of stroke
bool start_button = false;
bool reverse_button = false;
bool stop_button = true;
bool StartTestFlag = false;
bool StartTrigger = false;
float TestingSpeed = 0.0013 * MotorSpeedINPUT * MotorSpeedINPUT
   + 0.9275 * MotorSpeedINPUT + 1.5245; // Calibration curve for
    the motor speed
//Button Pin reading setup
int rlimit_1;
int rlimit_2;
int rstart_button;
int rreverse_button;
int rstop_button;
unsigned int i = 0;
//assign pin numbers for buttons
int limitswitch1Pin = 2;   //interupt pin INT.0 priority
int limitswitch2Pin = 18;   //interupt pin INT.1 priority
int startswitchPin = 24;
int stopswitchPin = 19;    //interupt pin INT.2 priority
int reverseswitchPin = 26;
int StartTriggerPin = 3;   // interupt for serial read event
   used to start or stop stepper
////////////////////////////////////////////////////////////
void setup() {
Wire.begin(8);                // join i2c bus with address #8
Wire.onReceive(receiveEvent); // register event
// Setting up Pins
pinMode(limitswitch1Pin , INPUT);
pinMode(limitswitch2Pin , INPUT);
pinMode(startswitchPin , INPUT);
pinMode(stopswitchPin , INPUT);
pinMode(reverseswitchPin , INPUT);
pinMode(StartTriggerPin , INPUT_PULLUP);
//Setting initial sates
digitalWrite(limitswitch1Pin, LOW);
```

```
digitalWrite(limitswitch2Pin, LOW);
digitalWrite(startswitchPin, LOW);
digitalWrite(stopswitchPin, LOW);
digitalWrite(reverseswitchPin, LOW);
//  digitalWrite(StartTriggerPin, HIGH);
//Initiating Interrupts
attachInterrupt(digitalPinToInterrupt(limitswitch1Pin), limitONE
    , HIGH);
attachInterrupt(digitalPinToInterrupt(StartTriggerPin), START,
   RISING);
attachInterrupt(digitalPinToInterrupt(limitswitch2Pin), limitTWO
    , HIGH);
attachInterrupt(digitalPinToInterrupt(stopswitchPin), STOP, HIGH
   );
Serial.begin(115200); //Set the same serial speed in the serial
   terminal
}
////////////////////////////////////////////////////////////////
// Interupt function for recieving data between Arduinos
void receiveEvent(int howMany) {
int x = Wire.read();
if (x == 3) {    // '3' is the signal code for max pressure
   reached, proceduce is to stop the stepper, it can only move
   backwards
stepper.stop();
// Setting button flags to prevent further forward movement
limit_1 = true; //also activated as backup
stop_button = true; //also activated as backup
start_button = false;
reverse_button = false;
}
}
////////////////////////////////////////////////////////////////
//Interrupt function limitONE when limit switch one is triggered
    at the end of the syringe pump stoke
void limitONE() {
stepper.stop();
limit_1 = true; //indicates the limit switch is triggers
stop_button = true; //also activated as backup
start_button = false;
```

```
reverse_button = false;
StartTrigger = false;
Serial.println("**************PIN LIMIT 1 PUSHED
   ************************");
}
////////////////////////////////////////////////////////////
//Interrupt function limitTWO when limit switch two is triggered
    at the beginning of the syringe pump stoke
void limitTWO() {
stepper.stop();
//  delay(100); // without delay, code was breaking, stepper
   would stop and no buttons would work
stepper.begin(100, 16);// initiate motor to move at 100 RPM
stepper.move(-800); // move forward small amount to move off of
   the limit switch
stepper.stop(); //Stop movement
limit_1 = false;
limit_2 = false;
stop_button = true;
start_button = false;
reverse_button = false;
StartTrigger = false;
}
////////////////////////////////////////////////////////////
// Interrupt function when the red stop button is pressed
void STOP() {
stepper.stop();
stop_button = true;
start_button = false;
reverse_button = false;
limit_1 = false;
StartTrigger = false;
Serial.println("********STOP PUSHED********");
}
////////////////////////////////////////////////////////////
// Function for when the start button is pressed
void START() {
StartTrigger = true;
Serial.println("***Start triggered***");
}
```

```
////////////////////////////////////////////////////////////////
void loop() {
//Reading button pins
rlimit_1 = digitalRead(limitswitch1Pin);
rlimit_2 = digitalRead(limitswitch2Pin);
rstart_button = digitalRead(startswitchPin);
rreverse_button = digitalRead(reverseswitchPin);
rstop_button = digitalRead(stopswitchPin);
// Debugging code to monitor button trigger states
//      Serial.print("PIN LIMIT 1 = ");
//      Serial.println(rlimit_1);
//      Serial.print("PIN LIMIT 2 = ");
//      Serial.println(rlimit_2);
//      Serial.print("PIN START   = ");
//      Serial.println(rstart_button);
//      Serial.print("PIN REVERSE = ");
//      Serial.println(rreverse_button);
//      Serial.print("PIN STOP    = ");
//      Serial.println(rstop_button);
//      Serial.println("////////////");
////////////////////////////////////////////////////////////////
//Changing button flags depending on which button is pushed
if (rstart_button == HIGH) {
start_button = true;
stop_button = false;
reverse_button = false;
limit_2 = false;
}
else if (rreverse_button == HIGH) {
reverse_button = true;
stop_button = false;
start_button = false;
limit_1 = false;
}
// Debugging code to monitor button trigger states
//    Serial.print("LIMIT 1 = ");
//    Serial.println(limit_1);
//    Serial.print("LIMIT 2 = ");
//    Serial.println(limit_2);
//    Serial.print("START   = ");
```

```
//     Serial.println(start_button);
//     Serial.print("REVERSE = ");
//     Serial.println(reverse_button);
//     Serial.print("STOP    = ");
//     Serial.println(stop_button);
//     Serial.println("////////////////////////////////////");
////////////////////////////////////////////////////////////
//// If the Syringe pump in in the middle of its stroke
if (limit_1 == false && limit_2 == false) {
// Stop movement on stepper
if ((start_button == false) && (reverse_button == false) && (
   stop_button == true)) {
stepper.stop(); // maintain stop
if (StartTestFlag == true) {
Wire.beginTransmission(9); // transmit signal to sensor ardunio
Wire.write(1);              // sends one byte signal code '1'
   for stop command
Wire.endTransmission();     // stop transmitting
Serial.println("Test Stopped");
Serial.println("");
StartTestFlag = false;
}
}
//Start moving the syringe pump forward when Start button is
   pressed
else if ((start_button == true) && (reverse_button == false) &&
   (stop_button == false)) {
StartTestFlag = true;
Wire.beginTransmission(9); // transmit signal to sensor ardunio
Wire.write(0);              // sends one byte signal code '0'
   for Start command
Wire.endTransmission();
Serial.print("Starting Test at "); Serial.print(TestingSpeed);
   Serial.println(" RPM");
delay(2000); // 2s Delay for Sensor Arduino to capture zero
   reference data
while ((start_button == true) && (reverse_button == false) && (
   stop_button == false)) {
stepper.begin(TestingSpeed, 8); // initiate motor to move at the
    testing speed
```

```
stepper.move(-10000); ///move many steps, aiming for continuous
   movement until interupt pin stops movement
}
}
//Start moving the syringe pump backwards when Reverse button is
    pressed
else if ((start_button == false) && (reverse_button == true) &&
   (stop_button == false)) {
while ((start_button == false) && (reverse_button == true) && (
   stop_button == false)) {
//  stepper.setMicrostep(32);
stepper.begin(400, 8);
stepper.move(10000); // move back until Limit 2 is reached
}
}
else {
return;
}
}
////////////////////////////////////////////////////////////
//// If the Syringe pump is at the end limit of its stroke when
   limit switch 1 is triggered
else if ((limit_1 == true)) {
stepper.stop();
if (StartTestFlag == true) {
Wire.beginTransmission(9); // transmit to Sensor Arduino
Wire.write(2);              // sends one byte code '2' which is
   a stop command
Wire.endTransmission();     // stop transmitting
Serial.println("Test Stopped (End Limit)");
Serial.println("");
StartTestFlag = false;
}
}
////////////////////////////////////////////////////////////
//// backup safety stop, there shouldnt be any other conditions
   than the ones above
else {
stepper.stop();
stop_button = true;
```

```
start_button = false;
reverse_button = false;
}
}
```

C.2 Sensor Arduino Code

This code is uploaded to the Sensor-Arduino that processes the signals from the pressure transducer, rotary encoder and outputs the TTL signal for triggering the two cameras. The data is outputted to the serial terminal on the laptop via USB connection where it is saved after each test.

```
//MASTER arduino
// Sensors:
//    1 BAR Pressure transducer
//    Rotary encoder
#include <Wire.h>
#include <Adafruit_ADS1015.h>
Adafruit_ADS1115 ads;
/////
/////          CAMERA FREQUENCY INPUT
/////
float TTLfreq = 8; // (Hz)          Not 100% accurate, arduino
   clock is underclocked, timer is slower
/////                               The pressure time stamps and
    cameras are triggered off the same clock so the underclock
   isnt an issue
/////
float Voltage = 0.0;
float Pressure = 0.0;
int TTLpin = 12;
bool TTLflag = true;
int MaxPressure = 90; // This is the Pressure (kPa) that the
   will stop a test.
#include <TimerOne.h>
#define encoder0PinA  2
#define encoder0PinB  3
bool SerialPrintFlag = LOW;
float TTLperiod = 500000 / TTLfreq; // (seconds)
volatile float StartTime = 0;
volatile float oldPulse = 0;
volatile float deltaPulse = 0;
volatile float ElapsedTime = 0;
volatile float CurrentTime = 0;
volatile float TIME = 0.0;
volatile float encoder0Pos = 0;
```

```
volatile float speedReading = 0;
volatile float timeread = 0;
float TestStartTime;
float TestEndTime ;
float TestTime;
float TestingRPM;
volatile float SpeedArray[20];
int i = 0;
float RPMsum = 0;
float AveRPM = 0;
//
   ////////////////////////////////////////////////////////////////////

void setup(void)
{
Wire.begin(9); // join i2c bus (address optional for master)
Wire.onReceive(receiveEvent); // register event
ads.begin();
pinMode(TTLpin, OUTPUT);
pinMode(encoder0PinA, INPUT);
pinMode(encoder0PinB, INPUT);
// encoder pin on interrupt 0 (pin 2) Pins from the rotary
   encoder
attachInterrupt(0, doEncoderA, CHANGE);
// encoder pin on interrupt 1 (pin 3)  Pins from the rotary
   encoder
attachInterrupt(1, doEncoderB, CHANGE);
Timer1.initialize();  //initialise interupt timer, period in (
   microseconds)
Timer1.attachInterrupt(TTL, TTLperiod);
analogWrite(TTLpin, 100);
Serial.begin (115200); // Set serial terminal to same speed
StartTime = micros(); //
}
//
   ////////////////////////////////////////////////////////////////////

// Function for
void TTL() {
if (SerialPrintFlag == HIGH) {
```

```
if (TTLflag == true) {
digitalWrite(TTLpin, HIGH);
TTLflag = false;
}
else if (TTLflag == false) {
digitalWrite(TTLpin, LOW);
TTLflag = true;
}
}
else {
digitalWrite(TTLpin, LOW);
}
}
//
   ////////////////////////////////////////////////////////////////////

// Recieving data commands from the motor Arduino
void receiveEvent(int howMany) {
if (howMany == 1) {
int x = Wire.read();
if (x == 0) {
for (int k = 0; k < 20; k++) {    ////setting RPM array to zeros
SpeedArray[k] = 0;
}
//Start test, start serial printing
Serial.println(""); Serial.println("Test started."); Serial.
   println("");
Serial.print("time(s)"); Serial.print(" "); Serial.print("
   Pressure(kPa)");
Serial.print(" "); Serial.println("RPM");
TestStartTime = millis();
TIME = 0;
SerialPrintFlag = HIGH;
}
if (x == 1) {
//Stop test.Stop serial printing
SerialPrintFlag = LOW;
Serial.println(""); Serial.println("Test Stopped."); Serial.
   println("**********************");
```

```
TestEndTime = millis();
TestTime = (TestEndTime - TestStartTime) / 1000;
Serial.println("Total test time (seconds)");
Serial.println(TestTime); Serial.println(" ");
}
else if (x == 2) {
//Stop test.Stop serial printing
SerialPrintFlag = LOW;
Serial.println(""); Serial.println("Test Stopped (End Limit)");
   Serial.println("**********************");
TestEndTime = millis();
TestTime = (TestEndTime - TestStartTime) / 1000;
Serial.println("Total test time (seconds)");
Serial.println(TestTime); Serial.println(" ");
}
}
}
//
   ////////////////////////////////////////////////////////////////////////

void loop(void)
{
TIME = millis() - TestStartTime; TIME = TIME / 1000;
int16_t adc0;
adc0 = ads.readADC_SingleEnded(0);
Voltage = (adc0 * 0.1875) / 1000 + 0.021;
Pressure = Voltage * 100 / 5;
///////Stop stepper if max pressure is reached
if (Pressure > MaxPressure & SerialPrintFlag == HIGH) {
//send command to slave (stepper arduino) to stop test)
//    analogWrite(MaxPressurePin, HIGH); //attached to interupt
   function on stepper arduino
SerialPrintFlag = LOW;
Serial.println("");
Serial.print("Maximum Pressure Exceeded (Pressure >");
Serial.print(MaxPressure); Serial.println("kPa) Test Stopped");
Serial.println(" ");
Wire.beginTransmission(8); // transmit to device #8
Wire.write(3);              // 3 indicates max pressure reached
Wire.endTransmission();     // stop transmitting
```

```
}
else if (Pressure > MaxPressure & SerialPrintFlag == LOW) {
//    analogWrite(MaxPressurePin, HIGH);
Serial.print("WARNING!(Current ");
Serial.print(Pressure); Serial.print("kPa > Max ");
Serial.print(MaxPressure); Serial.println("kPa)");
delay(1000);
}
else if (Pressure < MaxPressure) {
}
deltaPulse = abs(encoder0Pos - oldPulse);
if (i == 20) {
i = 0; // reset to start
}
if (deltaPulse >= 15) { // find time taken to move 15 pulses
CurrentTime = micros();
ElapsedTime = (CurrentTime - StartTime) / 60000000; //time in
   min
speedReading = (deltaPulse / 1600) / ElapsedTime;
SpeedArray[i] = speedReading; // inputs a speed reading into the
    array of 20
i++;
oldPulse = encoder0Pos;
StartTime = micros();
}
RPMsum = 0;
for (int j = 0 ; j <= 19 ; j++) {
RPMsum = RPMsum + SpeedArray[j];
}
AveRPM = RPMsum / 20;
if (SerialPrintFlag == HIGH) { // print out data to serial
   terminal
Serial.print(TIME, 3); Serial.print(" ");
Serial.print(Pressure); Serial.print(" ");
Serial.println(AveRPM);
}
}
//
   ////////////////////////////////////////////////////////////////////
```

```
// Calculates and displays average motor speed from 20 past
   readings
void AVEspeed() {
RPMsum = 0;
for (int j = 0 ; j <= 19 ; j++) {
RPMsum = RPMsum + SpeedArray[j];
}
AveRPM = RPMsum / 20;
}
//
   ////////////////////////////////////////////////////////////////

// Interrupt for reading signal A from rotary encoder
void doEncoderA() {
// look for a low-to-high on channel A
if (digitalRead(encoder0PinA) == HIGH) {
// check channel B to see which way encoder is turning
if (digitalRead(encoder0PinB) == LOW) {
encoder0Pos = encoder0Pos + 1;          // CW
}
else {
encoder0Pos = encoder0Pos - 1;          // CCW
}
}
else   // must be a high-to-low edge on channel A
{
// check channel B to see which way encoder is turning
if (digitalRead(encoder0PinB) == HIGH) {
encoder0Pos = encoder0Pos + 1;           // CW
}
else {
encoder0Pos = encoder0Pos - 1;           // CCW
}
}
}
//
   ////////////////////////////////////////////////////////////////

// Interrupt for reading signal B from rotary encoder
void doEncoderB() {
```

```
// look for a low-to-high on channel B
if (digitalRead(encoder0PinB) == HIGH) {
// check channel A to see which way encoder is turning
if (digitalRead(encoder0PinA) == HIGH) {
encoder0Pos = encoder0Pos + 1;          // CW
}
else {
encoder0Pos = encoder0Pos - 1;          // CCW
}
}
// Look for a high-to-low on channel B
else {
// check channel B to see which way encoder is turning
if (digitalRead(encoder0PinA) == LOW) {
encoder0Pos = encoder0Pos + 1;           // CW
}
else {
encoder0Pos = encoder0Pos - 1;           // CCW
}
}
}
```

Appendix D

Matlab code

D.1 Curvature Code

This code has been adapted from the code published by Machado *et al.* [1]. The adaptations include solving the eigenvalue problem as explained in Section 2.4 which yield principal curvatures and their respective directions.

```
function [b11,g3,g11,g12,g22,x,y,u1,u2,v1,v2,EigVect,EigVal, K,
    H, Ki, Kii] = scurvature (X, Y, Z, gs)
%function [b11,b12,b22,g3,g11,g12,g22, K, H, Ki, Kii] =
    scurvature (X, Y, Z, gs)
% scurvature compute gaussian, mean and principal curvatures of
    a surface
% [K, H, Ki, Kii] = scurvature (X, Y, Z, gs), where:
% X, Y, Z are matrix of points on the surface.
% gs specifies the spacing between points in every direction. (
    Default gs = 1)
% K is the gaussian curvature.
% H is the mean curvature.
% Ki and Kii are minimum and maximum curvatures at each point.%

% First Derivatives
[Xu, Xv] = gradient(X, gs);
[Yu, Yv] = gradient(Y, gs);
[Zu, Zv] = gradient(Z, gs);
% Second Derivatives
[Xuu, Xuv] = gradient(Xu, gs);
[Yuu, Yuv] = gradient(Yu, gs);
```

```
[Zuu, Zuv] = gradient(Zu, gs);
[Xuv, Xvv] = gradient(Xv, gs);
[Yuv, Yvv] = gradient(Yv, gs);
[Zuv, Zvv] = gradient(Zv, gs);
% Reshape 2D Arrays into vectors
Xu = Xu(:); Yu = Yu(:); Zu = Zu(:);
Xv = Xv(:); Yv = Yv(:); Zv = Zv(:);
Xuu = Xuu(:); Yuu = Yuu(:); Zuu = Zuu(:);
Xuv = Xuv(:); Yuv = Yuv(:); Zuv = Zuv(:);
Xvv = Xvv(:); Yvv = Yvv(:); Zvv = Zvv(:);
Xu = [Xu Yu Zu];
Xv = [Xv Yv Zv];
Xuu = [Xuu Yuu Zuu];
Xuv = [Xuv Yuv Zuv];
Xvv = [Xvv Yvv Zvv];
% First fundamental form coef f icients (g11, g12, g22)
g11 = dot(Xu, Xu, 2);
g12 = dot(Xu, Xv, 2);
g22 = dot(Xv, Xv, 2);
% Normal vector (g3)
m = cross(Xu, Xv, 2);
p = sqrt(dot(m, m, 2));
g3 = m./[p p p];
% Second fundamental Coef f icients of the surface (b11, b12,
   b22)
b11 = dot(Xuu, g3, 2);
b12 = dot(Xuv, g3, 2);
b22 = dot(Xvv, g3, 2);
[s, t] = size (Z);
% Gaussian Curvature (K)
K = (b11 .* b22 - b12.^2)./(g11 .* g22 - g12.^2);
K = reshape (K, s, t);
% Mean Curvature (H)
H = (g11 .* b22 + g22 .* b11 - 2. * g12.* b12)./(2 *(g11.* g22 -
    g12.^2));
H = reshape (H, s, t);
% Principal Curvatures.
Ki = H + sqrt(H.^2 - K);
Kii = H - sqrt(H.^2 - K);
%% Solving the Eigen value problem
```

```
for i = 1:length(b11)
B=[b11(i) b12(i);b12(i) b22(i)];
G=[g11(i) g12(i);g12(i) g22(i)];
SumNaN = sum(isnan(B(:)));
if SumNaN == 0
D=B/G;

[EigVect,EigVal]=eig(D);

EigVal=EigVal(:);
[maxVal,MaxIndx]=max(EigVal);
if MaxIndx == 4 %second eigen vector is max
u1(i)=EigVect(1,2);
v1(i)=EigVect(2,2);
u2(i)=EigVect(1,1);
v2(i)=EigVect(2,1);
elseif MaxIndx == 1
u1(i)=EigVect(1,1);
v1(i)=EigVect(2,1);
u2(i)=EigVect(1,2);
v2(i)=EigVect(2,2);
end
end
end
% Orienting directions to be similar
for i=1:length(u1(:,1))
if u1(i)<0
u1(i)=u1(i)*-1;
v1(i)=v1(i)*-1;
end
if v2(i)<0
u2(i)=u2(i)*-1;
v2(i)=v2(i)*-1;
end
end
x=X(:); y=Y(:); u1=u1(:); v1=v1(:); u2=u2(:); v2=v2(:);
end
```

D.2 Variable Processing

This code imports data from the Curvature code and testing data from the Sensor-Arduino. The Stress Calculation function is called in order to calculate the stress at each point. The output of this code is principal stresses and strains at every point and every step.

```
clear all
% Specimens to process
SpecimenNumbers =[1:18 28:33];
%SpecimenNumbers = [1:3];
%SpecimenNumbers =9;
SpecimenInfo = xlsread('specimen_info.xlsx');
data.SpecimenInfo=SpecimenInfo;

for i=SpecimenNumbers %run though each specimen
clearvars -except data SpecimenNumbers i
i
SpecimenName= strcat('Specimen',int2str(i));
%Adds path for Folder of step files
StepFilePathName = strcat('C:\Users\CRRAND009\OneDrive\M.Sc\
   Scurvature/S',int2str(i));
addpath(StepFilePathName)

%Calls varibles from specimen info
T=data.SpecimenInfo(i,1);
FPS=data.SpecimenInfo(i,2);
gs=data.SpecimenInfo(i,3);
MaxStep=data.SpecimenInfo(i,5);

%Reads Pressure file for current specimen
PressureFileName=strcat('S',int2str(i),'.txt');
B = importdata(PressureFileName);
B.data(:,4) = B.data(:,1).*FPS; %finding when frames were taken
B.data(:,2)=B.data(:,2)-B.data(2,2);  %zeroing pressure

for ijk=1:1:MaxStep %run through each step file for one specimen

%Set file name
filename = strcat('Step_',int2str(ijk),'.txt');
A = importdata(filename);
```

```
%Find Pressure in Kpa for current step
[c,frameIndex] = min(abs(B.data(:,4)-ijk));
P(1,ijk)=B.data(frameIndex,2);
[d(ijk),zMaxRow] = max(A.data(:,18));
P(2,ijk)=P(1,ijk)-d(ijk)*9.78057/1000;%minus pressure due to
    height of bulge
if ijk>50
zMaxXIndexChar(ijk,:)=A.data(zMaxRow,1);
zMaxYIndexChar(ijk,:)=A.data(zMaxRow,2);
end
%% Variable Initialisation

Mx=max(A.data(:,1));
My=max(A.data(:,2));

X=zeros(Mx,My); Y=X; Z=X; EngStrain1=X; EngStrain2=X;

for k=1:length(A.data(:,1))
X(A.data(k,1),A.data(k,2)) = A.data(k,3);
Y(A.data(k,1),A.data(k,2)) = A.data(k,4);
Z(A.data(k,1),A.data(k,2)) = A.data(k,5);
EngStrain1(A.data(k,1),A.data(k,2)) = A.data(k,38)/1000;
EngStrain2(A.data(k,1),A.data(k,2)) = A.data(k,39)/1000;
end

for j=1:length(X(1,:))
for k=1:length(X(:,1))
if X(k,j)== 0
X(k,j)=NaN;
end
end
end

%% Function calls
[b11,g3,g11,g12,g22,x,y,u1,u2,v1,v2,EigVect,EigVal, K, H, Ki,
    Kii] = scurvature (X, Y, Z, gs);

[ModulusKi, ModulusKii,stressKi, stressKii] = stresscalc (
    EngStrain1, EngStrain2, Ki, Kii,T,P(2,ijk));
```

```
field=strcat('Step',int2str(ijk));
StressKi.(field)=stressKi;
StressKii.(field)=stressKii;
EngStrainKi.(field)=EngStrain1+1;
EngStrainKii.(field)=EngStrain2+1;
XYZ.(field)=A.data(:,1:5);
Pressure.(field)=P(2,:);
CurveDir.(field)=x(1:length(u1));
CurveDir.(field)(:,2)=y(1:length(u1));
CurveDir.(field)(:,3)=u1;
CurveDir.(field)(:,4)=v1;
CurveDir.(field)(:,5)=u2;
CurveDir.(field)(:,6)=v2;
end %end through each step file for one specimen

%this refers to the the row from DIC data matrix corresponding
   to mid point of max z displacement.
zMaxIndex=strcat(int2str(zMaxXIndexChar),int2str(zMaxYIndexChar)
   );
zIndex=mode(zMaxIndex);
data.SpecimenInfo(i,6)=str2double(zIndex(1:2));
data.SpecimenInfo(i,7)=str2double(zIndex(3:4));

data.(SpecimenName).StressKi=StressKi;
data.(SpecimenName).StressKii=StressKii;
data.(SpecimenName).EngStrainKi=EngStrainKi;
data.(SpecimenName).EngStrainKii=EngStrainKii;
data.(SpecimenName).Pressure=Pressure;
data.(SpecimenName).CurveDir=CurveDir;
data.(SpecimenName).XYZ=XYZ;

rmpath(StepFilePathName)
end %end run though each specimen
save('Variable_Processing_19Oct','data')
```

D.3 Stress Calculation

This function is called to calculate stress at each point. It uses curvature, pressure and strain to calculate membrane stress.

```
function [ModulusKi, ModulusKii, StressKi, StressKii] =
    stresscalc (EngStrain1, EngStrain2, Ki, Kii,T,P);
StressKi=Ki*0; StressKii=Ki*0;
ModulusKi=Ki*0; ModulusKii=Ki*0;
%% Calculate Stress at each point with regards to Ki and Kii
for i=1:length(EngStrain1(:,1))
for j=1:length(EngStrain1(1,:))
t=T/((1+EngStrain1(i,j))*(1+EngStrain2(i,j)));

StressKi(i,j)  =P/(2*t*Kii(i,j));
StressKii(i,j) =P/(2*t*Ki(i,j));

if StressKi(i,j)>1e3 || StressKi(i,j)<-1e2
StressKi(i,j)=0;
end
end
end
ModulusKi=StressKi./EngStrain1;
ModulusKii=StressKii./EngStrain2;
% StressKi=StressKi(:);
end
```

Appendix E

Additional Resources

E.1 Motor Calibration

The stepper motor control consists of the following components and tools:

- Arduino Mega 2560
- 2H5676B20S340 Sanyo Denki Bipolar Bipolar Stepper Motor 1.8°, 1.27Nm, 36V DC, 2A, 4 Wires
- DRV8825 Stepper motor driver board
- Arduino CNC shield V3
- Arduino BasicStepperDriver Library: https://github.com/laurb9/StepperDriver

The driver library was found to not accurately run the stepper motor at given input speeds. The different motor speeds were recorded for different micro-stepping settings as seen in Table E.1. The most accurate setting was full step but the full step setting could not turn the motor faster than 318RPM and using full steps did not provide smooth operation of the stepper and low speeds. The 1/8 setting was chosen as the most desirable because it allowed for the greatest speed and still maintained smooth motion at all speeds above 0.8RPM. The calibration curve for input vs output speeds at 1/8 micro stepping in seen in Figure E.1.

Table E.1 *Table showing the motor speeds for different micro-stepping settings.*

Input speed	**Micro-step setting**				
(RPM)	**full step**	**1/2**	**1/8**	**1/16**	**1/32**
0.8					0.81
1	0.99	1	1.01	1.01	1
200	195	196	170	150	
210	205				
220	215				129
230	225				
240	233				
250	244				
260	253				
270	262				
290	280	281			
320	305	302			154
330	318	310	275		
335	FAIL	314	279		
370		340	295	227	
450		FAIL	330	255	192
500			355	270	192
600			FAIL	301	204
800				352	205
1000				FAIL	205

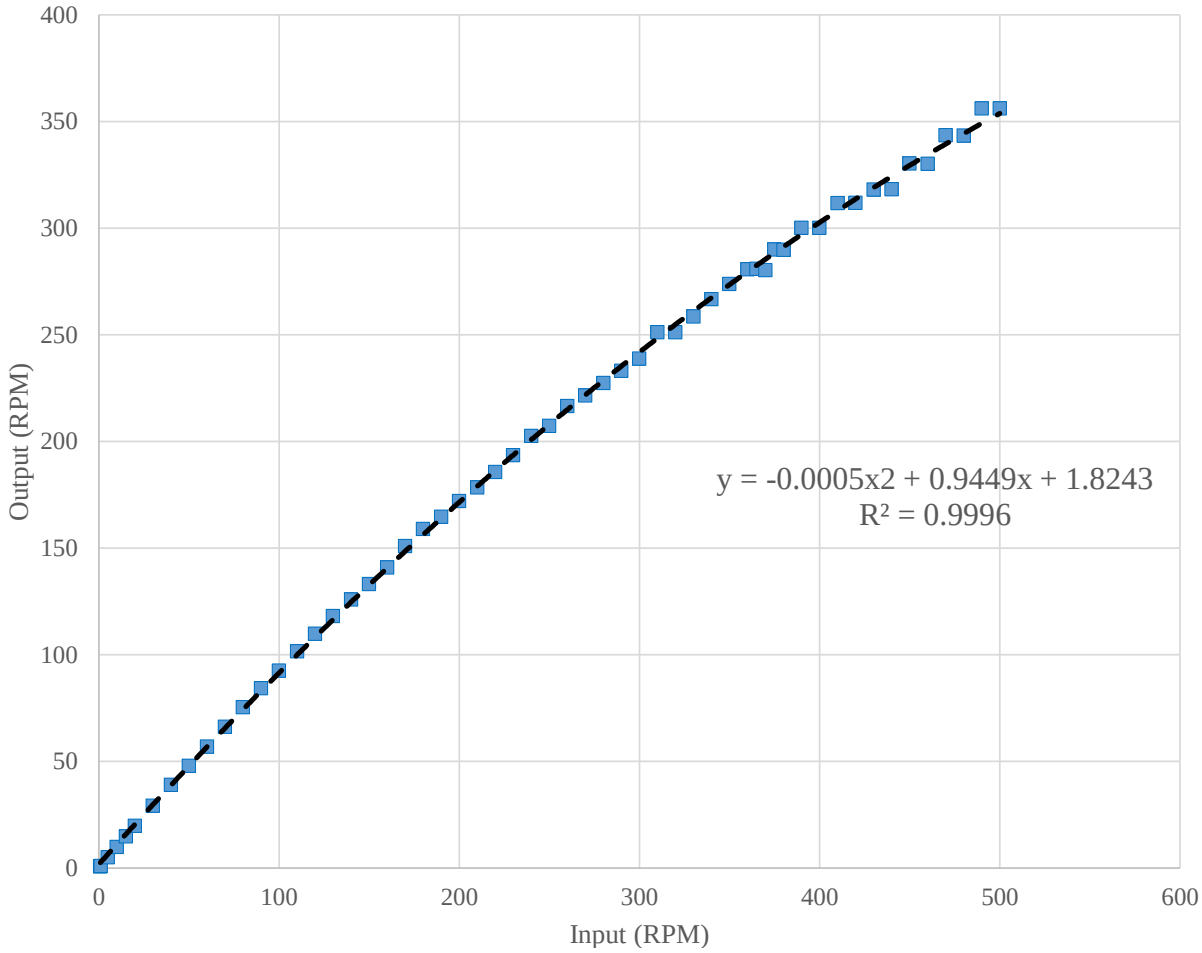

Figure E.1 Calibration curve for the stepper motor output speed using 1/8 micro-stepping.

E.2 Pressure Transducer Calibration

The pressure transducer was calibrated using a finely calibrated pressure gauge as a reference for measuring the input pressure. Voltages were recorded at pressure intervals of 10kPa from 10kPa to 100kPa. The calibration curve for the 100kPa pressure transducer is seen in Figure E.2.

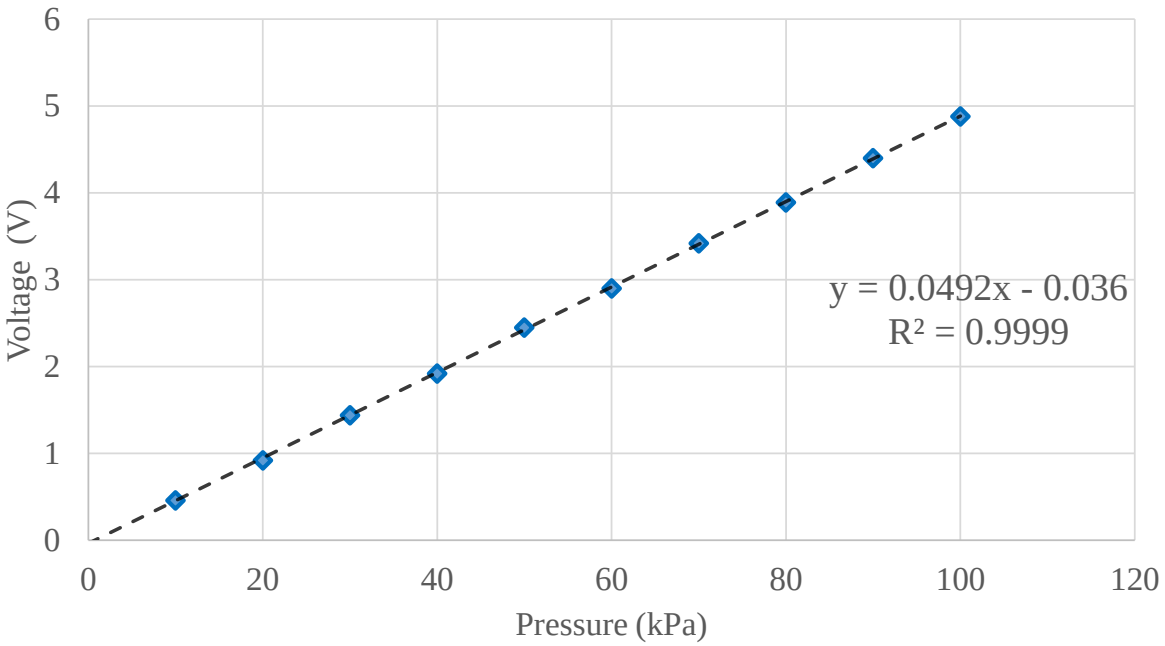

Figure E.2 Calibration curve for the 100kPa pressure transducer.